UNIVERSITÀ DEGLI STUDI DI CATANIA
FACOLTÀ DI SCIENZE MATEMATICHE, FISICHE E NATURALI
DOTTORATO DI RICERCA IN FISICA

MARIANGELA BONDÍ

HEAVY-ION DOUBLE CHARGE EXCHANGE REACTIONS AS TOOLS FOR $0\nu\beta\beta$ DECAYS. THE ^{40}Ca(^{18}O,^{18}Ne)^{40}Ar REACTION AT 270 MEV BY USING MAGNEX

PH.D THESIS

PH.D COORDINATOR: PROF. F. RIGGI

TUTOR: PROF. F. CAPPUZZELLO
CO-TUTOR: DR. M. CAVALLARO

XXVII CICLO 2011-2014

É strano che tanto tempo sia passato
dall'annunzio del grande crac: seppure
quel tempo e quella notizia siano esistiti.
L'abbiamo letto nei libri: il fuoco non li risparmiava
e anche di noi rimarrá un'eco poco attendibile.
Attendo qualche nuova di me che mi rassicuri.
Attendo che mi si dica ció che nasconde il mio nome
Attendo con la fiducia di non sapere
perché chi sa dimentica persino
di essere stato in vita.
E. Montale, *Satura*

Ai miei due pilastri: Rosanna e Lucio

Acknowledgements

I am grateful to many people, professionally and personally, for their help, support, and encouragement during the completion of this work. My first thanks goes to my tutor, Prof. Francesco Cappuzzello, for the constant cure he had on my research activity, for his great competence and precious teachings. Special thanks to Dr. Manuela Cavallaro, her advices and suggestions are always insightful and helpful.

An enormous thanks goes to Dr. Diana Carbone, colleague but above all dear friend. In these years, we have shared all, sunny and rainy days, constantly helping each other. I am really grateful to her for all the effort she spent in constantly supporting me, both in personal life and in work.

I would like to thank also the other members of my research group: Dr. Clementina Agodi, Prof. Antonino Foti, Prof. Angelo Cunsolo, Dr. Marzio De Napoli.

I am particularly grateful to Prof. H. Lenske, for his kindness to welcome me during my visit in Giessen. Working with him has been a very fruitful experience.

A special thanks goes to my colleagues and friends Luca Guardo and Iolanda Indelicato, who shared with me these crazy days, supporting and helping each other.

An enormous thanks goes to my friends Dario Nicolosi, Cristina Schillaci and Roberta Spartá, for their constant encouragement and support. Without them, I am sure I would have missed one of the best things I found in this place, their sincere friendship.

A special thanks goes to all the guys of the LNS, especially to Armandino, Antonellina, Peppedagata, Lurenzen, Mini, La Scudy, Lucia and Giovanna.

Particular and reserved thanks goes to my dear friends Cristina e Laura, who shared with me these years.

A personal thanks goes to my best friends Danila and Giulia, for being always close to me. They are my guardian angels. A great thanks goes to my new dear friend Davidino, who is a special and nice person.
There are no appropriate words to thank my big and crazy family at all, for giving me all the love, the support and for constantly encouraging me through these years. Finally, a special thought goes to my nephew Michelino, who I love deeply

Abstract

This study is inserted in a research line that aims to access the Nuclear Matrix Element (NME) involved in the half-life of the $0\nu\beta\beta$ decay, by measuring the cross sections of heavy-ion induced Double Charge Exchange (DCE) reactions with high accuracy. The basic point is that the initial and final state of both $0\nu\beta\beta$ decay and DCE processes are the same. In addition, both processes pass through the same intermediate state and the transition operators have a similar mathematical structure.

This work shows for the first time experimental data on heavy-ion DCE reaction in a wide range of transferred momenta, with an acceptable statistical significance and good angular and energy resolution. In particular (^{18}O,^{18}Ne) reaction at 270 MeV incident energy on ^{40}Ca target was investigated. In order to estimate the contribution of the concurrent channels the ^{40}Ca(^{18}O,^{18}F)^{40}K single charge exchange intermediate channel and the competing processes ^{40}Ca(^{18}O,^{20}Ne)^{38}Ar two-proton transfer and ^{40}Ca(^{18}O,^{16}O)^{42}Ca two-neutron transfer were also studied.

The experiment was performed at Laboratori Nazionali del Sud (LNS-INFN) in Catania using a 270 MeV energy ^{18}O Cyclotron beam impinging on a 279 μg/cm^2 thick ^{40}Ca target. The ejectiles were momentum analysed by the MAGNEX large acceptance magnetic spectrometer and detected by its focal plane detector.

The energy spectra and angular distributions have been extracted. The data analysis of experimental results have established that the transition to ^{40}Ar$_{g.s.}$ is dominated by the direct processes.

Finally, an innovative technique to infer on the nuclear matrix elements by measuring the cross section of a double charge exchange nuclear reaction was proposed. The main assumption are that the DCE reaction is a two-step charge exchange and a surface localized process. The model adopted to

describe the cross section of the DCE reaction consists in a generalization of the well-established factorization of the single charge-exchange cross section, valid under certain hypothesis, discussed in the thesis. Therefore, the cross section could be factorized in a nuclear structure term, containing the matrix elements, and a nuclear reaction one (unit cross section). Despite the used approximations, the extracted strength and nuclear matrix elements are reasonable within $\pm$ 50%, signalling that the main physics content has been kept.

Contents

Introduction

After 80 years since the first guess on its existence, neutrino still escapes our insight: the mass and the true nature (Majorana or Dirac) of this particle is still unknown. In the past years, neutrino oscillation experiments have finally provided the incontrovertible evidence that neutrinos species mix each other and have finite masses [1–3] . These results represent the strongest demonstration that the Standard Model of electroweak interaction is incomplete and that new physics beyond it exists. None of these experiments could however shade light on some of the basic features of neutrinos. In this scenario, a unique role is played by the Neutrinoless Double Beta ($0\nu\beta\beta$) decay searches. This decay is a process in which two neutrons change into two protons and emit two electrons as the sole decay products. These experiments can explore lepton number conservation, the Dirac/Majorana nature of neutrinos and their absolute mass scale (hierarchy problem) and might have an impact on the baryon asymmetry in the Universe via leptogenesis [4–7]. To achieve these goals certain hurdles have to be overcome.

From the experimental point of view, today, $0\nu\beta\beta$ decay studies faces a new era where large scale experiments with a sensitivity approaching the so-called degenerate-hierarchy region are nearly ready to start. The challenge for the next future is the construction of detectors characterized by a tonne-scale size and an incredibly low background, to fully probe the inverted-hierarchy region. A number of new proposed projects took up this challenge [8–11].

In addition, since the experimental decay rate is proportional to the square of the Nuclear Matrix Elements (NME), it is essential evaluating such matrix elements with high accuracy to be able to extract the neutrino effective mass.

The evaluation of the NMEs is presently limited to state of the art model calculations

based on different methods [12–17]. High precision experimental information from single charge exchange, transfer reactions and electron capture are used to constraint the calculations [18–22]. However, the ambiguities in the models are still too large and the constraints too loose to reach accurate values of the NMEs. In addition, some common assumptions, in the different competing calculations, could cause overall systematic uncertainties [8]. A precision of about 20-30% on the NMEs is considered mandatory to guarantee a reasonable conversion from half-lives to neutrino masses keeping the precision high enough to discriminate among the different models and determine the neutrino mass. For this reason, the enormous experimental efforts for searching $0\nu\beta\beta$-decay should be also oriented towards the experimental determination of the NMEs. Determining experimentally the NMEs for $0\nu\beta\beta$-decay is an important task and an old dream of many scientist involved in this research field. To reach this goal, the experimental study of other nuclear transitions where the nuclear charge is changed by two units leaving the mass number unvaried, in analogy to the $\beta\beta$-decay, could give important information. The most similar nuclear processes are the Double Charge Exchange (DCE) reactions which can be induced by pions or heavy-ions.

Past attempts to use pion DCE reactions [23–26] to probe $\beta\beta$-decay NMEs were abandoned due to the large differences in the momentum transfers and in the nature of the operators [8]. Early studies on heavy-ion induced DCE were also not conclusive. The reason was the lack of zero-degree data and the poor yields in the measured energy spectra and angular distributions, due to the very low cross sections involved, ranging from about 5-40 nb/sr [27, 28] to 10 μb/sr [29].

The present thesis work is connected to this ambitious task. Indeed, its main purpose is to demonstrate that it is possible to access the NMEs by measuring the cross sections of heavy-ion induced DCE reactions with high accuracy. The basic point is that the initial and final state of both $0\nu\beta\beta$-decay and DCE processes are the same and that transition operators are similar.

In particular, as a first pioneering attempt, the (^{18}O, ^{18}Ne) reaction at 270 MeV incident energy on ^{40}Ca target is investigated. In order to estimate the contribution of the concurrent channels, the two-proton transfer reaction ^{40}Ca(^{18}O,^{20}Ne)^{38}Ar, the two-neutron transfer reaction ^{40}Ca(^{18}O,^{16}O)^{42}Ca and the single-charge exchange ^{40}Ca(^{18}O,^{18}F)^{40}K reaction are also studied.

The experiments have been pursued in Catania at the INFN-LNS laboratories, using

the MAGNEX large acceptance magnetic spectrometer. The use of a modern high resolution and large acceptance spectrometer, as MAGNEX, allows to face the experimental challenges that limited in the past the experimental study of heavy ion DCE reactions. The measurement of DCE high-resolution energy spectra with reasonable statistics is crucial to identify the transitions of interest. The concurrent measurement of the cross section for other relevant reaction channels allows isolating the direct DCE mechanism from the competing transfer processes.

These thesis is organized as follows. A general overview of what is currently known about the neutrino and the properties that have still to be measured is discussed in Chapter 1. The double beta decay and the nuclear matrix element involved in the estimation of the half life are also described.

The status of the art regarding the past attempts about heavy-ion DCE and the renewed interest of the scientific community on it is summarized in Chapter 2. Furthermore, the similarities among the heavy-ion DCE reaction and $0\nu\beta\beta$ decay are investigated. Finally the optimal experimental conditions to study such processes are examined.

Chapter 3 is focused on the description of the experimental set-up used to explore the above mentioned nuclear reactions. The reaction ejectiles were momentum analysed by MAGNEX and detected by its focal plane detector. This experiment represents the first measurement at 0° performed by MAGNEX. Thus a detailed description about the technique used to set the spectrometer is presented.

Chapter 4 is devoted to the description of the adopted data reduction technique. This is a quite involved procedure made up of several steps. The first one consists in the identification of the ejectiles. The identification procedure is based on the standard ΔE-E technique for the atomic number (Z), while the mass number (A) is determined by the correlation between the measured ion positions at the focus and its kinetic energy. Once the ion tracks are measured at the focal plane detector, it is possible to optimize the spectrometer transport map up to the 10^{th} order. The whole procedure completely characterizes the investigated event, providing the ion kinetic energy and scattering angle in the laboratory reference frame. Starting from these quantities, the excitation energy spectra and angular distributions are constructed.

Chapter 5 describes the theoretical analysis of the ^{40}Ca(^{18}O,^{18}F)^{40}K single charge exchange reaction, which feeds the intermediate channel, in the framework of the Charge-Exchange Quasiparticle Random Phase Approximation (CEX-QRPA) [30–32]. The re-

sults of this calculation are used in the simple model adopted to extract the nuclear matrix element, as discussed in Chapter 6. In particular, the double charge exchange cross sections can be factorized in a nuclear structure term containing the matrix elements and a reaction factor. It is demonstrated that the model reproduces the experimental data and it is possible to extract the strengths and matrix elements within a tolerable accuracy under the hypothesis of a two-step charge exchange process.

Chapter 1

Neutrino physics and double beta decay

Neutrinos play a fundamental role in various areas of modern physics from nuclear and particle physics to cosmology. Two of the fundamental issues of neutrino physics:

- the nature of the neutrino: whether it is a Dirac or Majorana particle;
- its absolute mass scale.

Neutrinoless double beta decay ($0\nu\beta\beta$) experiments are the only practical test of the neutrino nature. If $0\nu\beta\beta$ experiments are successful and the neutrino is proved to be a Majorana particle, this discovery will have a profound effect in different area of physics. For example the Majorana neutrino would have implications for Grand Unified Theory of fundamental interactions and could explain the observed matter-antimatter asymmetry in the universe through the leptogenesis scenario [4–7].
An overview of what is currently known about the neutrino and the properties that have still to be measured, is presented in the first part of this Chapter. Then, the double beta decay is described, using particular attention on the nuclear matrix element involved in the estimation of the half life of the decay.

1.1 The neutrino history

The existence of electrically neutral half-spin particle was postulated by Wolfgang Pauli in 1930, as a *"desperate remedy"* to save the principle of energy conservation in beta

decay. It was Enrico Fermi in 1934 who named this particle *neutrino*, within the formulation of his theory of beta decay. Maria Goeppert-Mayer was the first to consider the double decay in her paper in 1935 [33], acknowledging Eugene Wigner for suggesting the problem. In 1937 the young Ettore Majorana published his theory of neutrinos, stating that neutrinos and antineutrinos are the same particle and suggesting an experiment to test his theory [34]. This work was followed by a succession of papers from Racah, Furry and Primakoff formulating neutrinoless β decay theory [35–37].

After their first attempt in 1952 [38], Frederick Reines and Clyde Cowan made the first detection of a neutrino at the Savannah River Nuclear Plant in 1956 [39]. In 1957 Bruno Pontecorvo proposed neutrino-antineutrino oscillations [40, 41], and then in 1962 Ziro Maki, Masami Nakagawa and Shoichi Sakata introduced the theory of neutrino flavour mixing and flavour oscillations [42]. Great interest in neutrino physics was raised by the discovery of lepton flavour non-conservation. The first hints for this phenomenon date back to the late '60, with R. Davis Homestake radiochemical experiment [1], when a deficit in the solar neutrino flux was observed. It took about thirty years to completely understand the problem. In 1998, the Super-Kamiokande experiment reported conclusive evidence that a significant fraction of muon-type atmospheric neutrinos disappeared when travelling from the other side of the Earth to their detector. Later, the conclusive solution of the so called solar neutrino problem came in 2002 thanks to the Sudbury Neutrino Observatory (SNO) [3], which confirmed that the missing ν_e were actually converted into neutrinos of other flavours. These data have led to the conclusion that the cause for the disappearance is the mixing of the neutrino flavours, producing the oscillation of one flavour of neutrino into others [2].

One of the strongest consequence of oscillations is that neutrinos must be massive particles. However, there are several questions that cannot be addressed by neutrino oscillation experiments: being to the leading term sensitive to the difference of the squared values of neutrino masses, oscillation experiments are not able to probe the absolute mass scale. Also the mechanism responsible for the generation of the neutrino masses cannot be investigated using oscillation experiments.

Exploring the absolute mass scale is currently one of the leading research topics in neutrino physics.

1.2 Neutrino Oscillations

The most astonishing evidence of the not null rest mass of neutrinos has come from oscillation experiments. Neutrino oscillations arise as a consequence of the fact that neutrino flavour eigenstates produced in weak interaction processes do not coincide with mass eigenstates. Flavour eigenstates $|v_f>$ are related to mass eigenstates $|v_k>$ by the Pontecorvo-Maki-Nakagawa-Sakata (PMNS) neutrino mixing matrix:

$$|v_f>=\sum_{k=1}^{3} U_{fk}^{*}|v_k>, \qquad f=(e,\mu,\tau) \quad k=(1,2,3) \tag{1.1}$$

U_{fk} is the PMNS matrix [43]. However, oscillation experiments can only determine the difference in the square of the masses of each mass state $\Delta m_{ij}^2 = m_i^2 - m_j^2$ where i,j = 1,2,3.

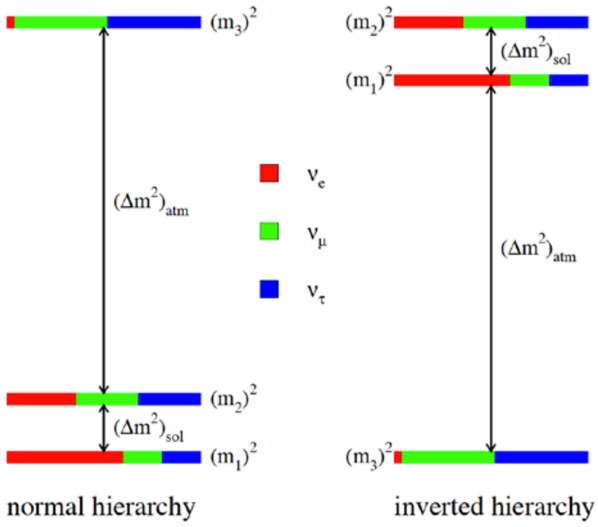

Figure 1.1: Pictorial representation of the two mass hierarchy schemes. The left picture represents the so-called normal hierarchy. The right picture represents the so called inverted hierarchy. The tree colours on each neutrino mass eigenstate represent the respective projection on the three flavour eigenstates. Note the definition $\Delta m_{sol}^2 = \Delta m_{21}^2$ and $\Delta m_{atm}^2 = \Delta m_{32}^2$. [8]

Solar and reactor neutrino experiments are sensitive to Δm_{21}^2, while atmospheric neutrinos predominantly reveal Δm_{32}^2. Measurements of matter effects in solar neutrino oscillations [44] have determined that the sign of Δm_{21}^2 is positive while the sign of Δm_{32}^2 is still unknown. The magnitude of Δm_{21}^2 is measured to be $7.54{\cdot}10^{-5}$ eV^2 and the

magnitude of Δm^2_{32} is measured to be about $2.43{\cdot}10^{-3}$ eV^2 . This situation leaves us with two possibilities for the three-neutrino mass spectrum:

- If $\Delta m^2_{32} > 0$, neutrino mass are arranged according to the so called normal hierarchy and the following relation holds: $m_1 < m_2 < m_3$;
- if $\Delta m^2_{32} < 0$, mass eigenstates are arranged to the inverted hierarchy. In this case the lightest neutrino is v_3 and the two other mass eigenstates are almost equal: $m_3 < m_1 \approx m_2$

Fig.1.1 shows a schematic view of the normal and inverted hierarchy models. As already stated, oscillation experiments give informations concerning specific properties of neutrinos and reveal aspects of neutrino physics that are blind to their Dirac or Majorana nature or to their absolute mass scale.

1.3 The neutrino mass and nature

The neutrino scenario is a puzzle. The neutrino is the only elementary particle, whose basic properties are not known till today. In contrast with the charged fermions the nature and the masses of the neutrinos has not yet been established experimentally.
The most sensitive mass measurements, involving electron neutrinos, are based on the study of the shape of the β spectrum end-point. Current best limits on m_β come from the Mainz [45] and Troitsk [46] tritium β-decay experiments: $m_\beta \lesssim 2.1$ eV. Such measurement have demonstrated that the lightest electron-type neutrino is very much lighter than the charged leptons ($m > 0.5$ MeV) and quarks ($m >$ few MeV). It appears that the mechanism responsible for the very light neutrino masses is completely different from the Higgs mechanism that generates the charged fermion masses in the Standard Model.
The neutrino can be like a Dirac particle, i.e fermion with two spin states each for neutrino and anti-neutrino. Another possibility is that only the neutrino exists with two states available: the left-handed neutrino and the right-handed neutrino. In this case the neutrino is called Majorana fermion. The existence of a Majorana neutrino will necessary imply that lepton number is not a conserved quantity [47].
If the neutrino is a Majorana fermion, we also have a natural way to understand its very light mass, though a mechanism proposed by Yanagida, Gell-Mann, Ramond

and Slansky [48–50] and known as "see-saw" mechanism. This mechanism provide the existence of heavy right-handed Majorana neutrinos that would produce a mechanism ("see-saw") to generate the very light neutrino masses implied in the neutrino oscillation experiments. Such mechanism means that the light Majorana neutrino mass is deeply related to the properties of new heavy particles at a mass scale of up to 10^{15} GeV. This is very close to the grand unified scale $\Delta_{GUT} \sim 10^{16}$ GeV above which it is believed that the electromagnetic, weak, strong and gravitational forces will unify.
The most promising approach to discriminate between these two possibilities is to search for neutrinolesss double beta decay ($0\nu\beta\beta$). Observation of neutrinoless double beta decay would not only imply that neutrinos are Majorana particles, it would also provide information on the neutrino mass hierarchy and on the absolute scale of neutrino mass.

1.4 Double beta decay

Double beta decay is a rare spontaneous process in which a nucleus (A, Z) decays to a nucleus (A, $Z \pm 2$) by emitting two electrons (or positrons) and, usually, other light particles:

$$(A, Z) \rightarrow (A, Z \pm 2) + 2e^{\mp} + \text{anything} \tag{1.2}$$

Double beta decay has a very low rate and can occur only in nuclei where single β-decay is forbidden. The parent nuclei (A,Z) must be less bound than final one (A, Z$\pm$2) but more bound than the intermediate nucleus (A, Z$\pm$1). This condition is verified in nature for several nuclei with an even number of protons and neutrons (see Fig.1.2), as a consequence of the *"pairing term"* in the nuclear binding energy, that favours energetically the even-even nuclei with respect to the odd-odd ones.
Double beta decay can be classified in various modes according to the various types of particles emitted in the decay. For $\beta^-\beta^-$, the processes $2\nu\beta\beta$ (see Fig.1.3a):

$$(A, Z) \rightarrow (A, Z + 2) + 2e^- + 2\overline{\nu} \tag{1.3}$$

is a second order process allowed in the Standard Model. Indeed, it was detected for the first time in ^{82}Se in 1987 [51] and it has been now observed in a dozen of nuclei (half-lives range from $\sim 10^{18}$ to $\sim 10^{22}$ years). This decay conserves the lepton number, cannot discriminate between Dirac and Majorana neutrinos and does not depend significantly on neutrino masses.

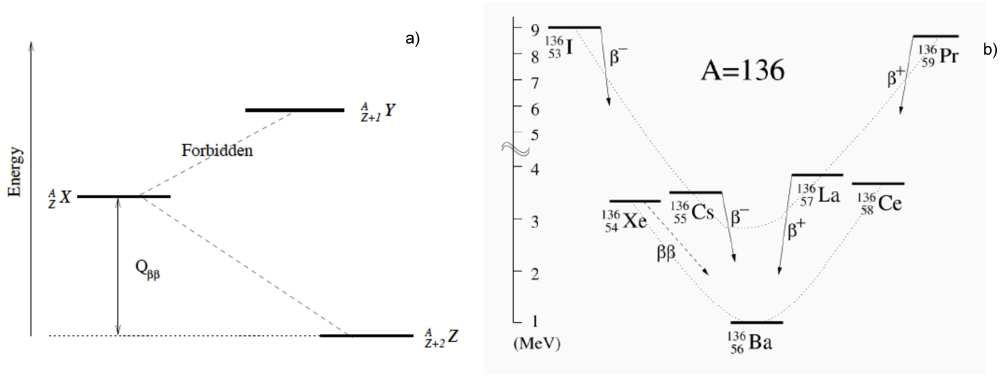

Figure 1.2: In panel a) a schematic diagram of the energy requirements for $\beta\beta$ decay: a parent nucleus ${}^{A}_{Z}\mathrm{X}$ decays to a daughter nucleus ${}^{A}_{Z+2}\mathrm{Z}$ because the intermediate single beta decay to ${}^{A}_{Z+1}\mathrm{Y}$ is energetically forbidden. In panel b) an example for the A=136 isobars. The even-even and odd-odd nuclei are connected by two distinct dotted curves. ^{136}Xe is stable for ordinary β^- decay, but unstable for the $\beta^-\beta^-$ decay. The same is true for ${}^{136}_{58}$Ce, which can decay by $\beta^+\beta^+$ decay.

There is also the possibility for double beta decay to occur without emission of neutrinos (see Fig.1.3b):

$$(A, Z) \rightarrow (A, Z + 2) + 2e^- \tag{1.4}$$

The process is of utmost importance for obtaining the neutrino mass since its decay probability is proportional to the square of "effective" neutrino mass $m_{\beta\beta}$:

$$m_{\beta\beta} = |\sum_i m_i U_{ei}^2| \tag{1.5}$$

Here the m_k are the masses of the three light neutrinos and U is the matrix that transforms states with well-defined mass into states with well-defined flavour.
This decay mode is forbidden in the Standard Model, since it violates the lepton number by two units and would imply the existence of a Majorana neutrino mass term [52].
A third process has been also considered, $0\nu\beta\beta M$ (see Fig.1.3a):

$$(A, Z) \rightarrow (A, Z + 2) + 2e^- + M^0 \tag{1.6}$$

in which a massless Nambu-Goldstone boson, called Majoron, is emitted [53]. However, most of the interest in this mode has disappeared in recent years and hence it will not be considered here.

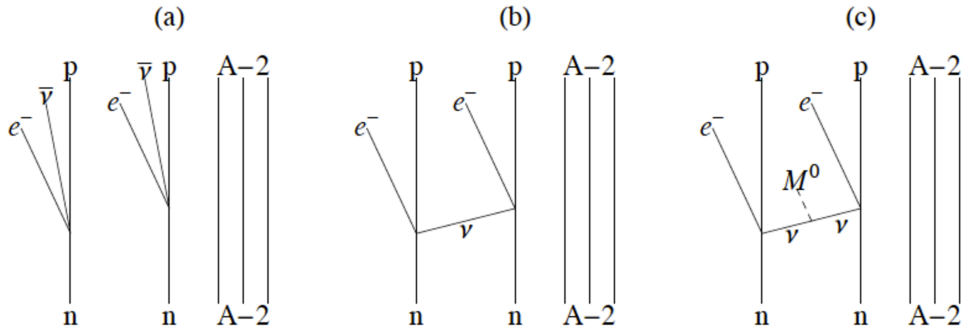

Figure 1.3: Double beta decay for (a) two-neutrino, (b) neutrinoless and (c) neutrinoless decay with Majoron emission.[54]

For $\beta^+\beta^+$ decay, the corresponding modes $2\nu\beta\beta$ and $0\nu\beta\beta$, are:

$$\begin{aligned}(A,Z) &\rightarrow (A,Z-2) + 2e^+ + 2\nu \\ (A,Z) &\rightarrow (A,Z-2) + 2e^+\end{aligned} \tag{1.7}$$

In this case, there are also the competing modes in which either one or two electrons are captured from the electron cloud, $2\nu\beta EC$, $2\nu ECEC$, $0\nu\beta EC$, $0\nu ECEC$.
For processes allowed by the standard model ($2\nu\beta\beta$,$2\nu\beta EC$, $2\nu ECEC$) the half-life can be, to a good approximation, factorized in the form:

$$\left[t^{2\nu}_{1/2}\right]^{-1} = G_{2\nu}|M_{2\nu}|^2 \tag{1.8}$$

where $G_{2\nu}$ is a phase space factor (that depends on the atomic number, the Q-values as well as on fundamental physics constants) and $M_{2\nu}$ the nuclear matrix element. For processes not allowed by the standard model, the half-life can be factorized as:

$$\left[t^{0\nu}_{1/2}\right]^{-1} = G_{0\nu}|M_{0\nu}|^2|f(m_i,U_{ei})|^2 \tag{1.9}$$

where $G_{0\nu}$ is a phase space factor that depends on the atomic number, the Q-values as well as on fundamental physics constants [54]. It includes fourth power of axial-vector coupling constant g_A and the inverse square of the nuclear radius R^2 [54, 55]. While $f(m_i,U_{ei})$ contains physics beyond the standard model through the masses m_i and mixing matrix elements U_{ei} of neutrino species and $|M_{0\nu}|^2$ is the nuclear matrix element (see Section1.6)
Neutrinoless double beta decay can proceed through many different mechanisms: almost any physics that violates the total lepton number can generate it. Light-neutrino

exchange is the "minimal" mechanism and the most commonly considered. The exchange of a light Majorana neutrino, does not require new particles or interactions. It requires the known left-handed interactions in addition to a massive Majorana neutrino. The virtual neutrino in the diagram 1.3 can be produced as an anti-neutrino at one vertex and absorbed as a neutrino, which is equal to the anti-particle thanks to the Majorana nature, at the other vertex.
Another less popular possibility is the mass contribution arising from $0\nu\beta\beta$ decay in the presence of right handed currents or heavy neutrinos in general [56, 57]. Nevertheless, Schechter and Valle [52] have shown that if $0\nu\beta\beta$ decay occurs in nature, neutrinos must be Majorana fermions, even if $0\nu\beta\beta$ decay is dominantly driven by a mechanism other than light Majorana neutrino exchange.

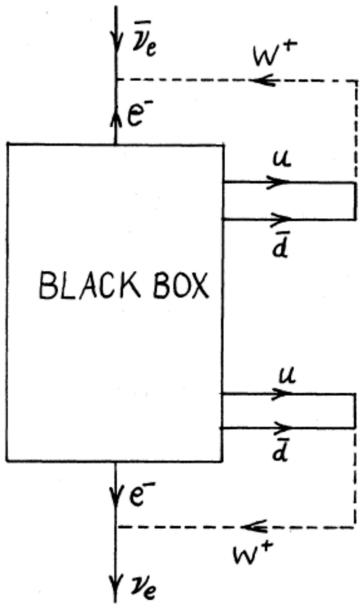

Figure 1.4: The diagram (from Schechter and Valle [52] shows how any $0\nu\beta\beta$ process induces a $\overline{\nu}_e$ to ν_e transition, that is, an effective Majorana term.

They constructed the diagram in Fig.1.4, in which whatever mechanism is responsible for $0\nu\beta\beta$ decay goes inside the "black-box". By connecting the external lines appropriately, a contribution to the neutrino propagator is obtained that turns an anti-neutrino into a neutrino thereby inducing a Majorana mass term for the neutrino. Thus, an experimental observation of $0\nu\beta\beta$ decay would provide model-independent proof that neutrinos are Majorana fermions. To determine the mechanism driving $0\nu\beta\beta$ decay,

measurements of $t_{1/2}^{0\nu\beta\beta}$ for multiple nuclides and well as accurate nuclear matrix elements are necessary.

1.5 Experimental aspects of $0\nu\beta\beta$ decay

The discrimination between the $2\nu\beta\beta$ decay and $0\nu\beta\beta$ one is, in principle, very simple and is based on the shape of the spectrum obtained by summing on the energies of the two emitted electrons. In fact, this spectrum is determined by the phase space of the other emitted particles.

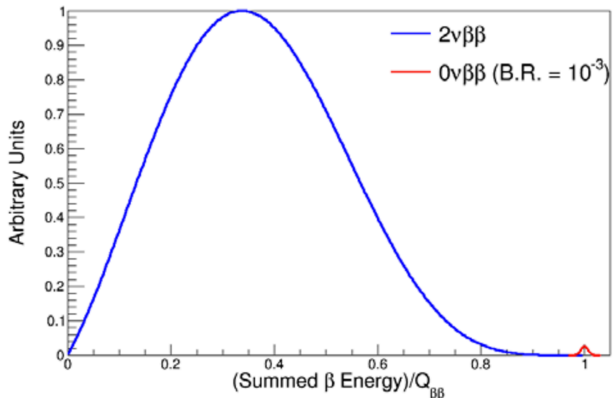

Figure 1.5: Illustration of a hypothetical two-neutrino (blue) and zero-neutrino (red) double beta decay energy spectrum. [8]

As shown in Fig.1.5, $2\nu\beta\beta$ is a four body decay, with a continuous spectrum featuring a maximum value around one third of the Q-value. On the contrary, the two electrons retain all the available kinetic energy in $0\nu\beta\beta$. For this reason, the spectrum is just a spike at the Q value of decay.

Therefore, double beta decay experiments are searching for a rare peak (see Fig.1.5) upon a continuum of background. Observing this small peak and demonstrating that it is truly $0\nu\beta\beta$ is a challenging experimental design task. Since double beta decays are low-energy second-order weak processes, the decay rates of $2\nu\beta\beta$ are of the order of 10^{20} yr, and the rates of $0\nu\beta\beta$ are even much smaller than $2\nu\beta\beta$-decay rates, depending on the assumed light neutrino mass in the case of the Majorana neutrino mediated process. Then the expected $0\nu\beta\beta$ half-lives are of the order of 10^{26} and 10^{27} yr in the case of the IH (inverted hierarchy) mass of 30 meV and the NH (normal hierarchy) mass of

3 meV, respectively [47]. Consequently, to record a sizeable number of $0\nu\beta\beta$ events over its operation time, an experiment needs to have a large amount of isotope, ranging from 100 Kg to few tonnes. On the other hand, the decay signature exploited by most experiments is simply based on monochromatic energy of the two emitted electrons. Unfortunately, there are several sources that can produce background counts in the same energy region, such as the natural radioactivity of detector components. The characteristics that make an ideal $0\nu\beta\beta$ experiment have been discussed in different reports [9–11].

Several candidate isotopes are available for neutrinoless double beta decay searches. The choice of isotope used in an experiment is guided by consideration about Q-value, nuclear matrix element, natural isotopic abundance, as well as the detector technology available to study the isotope. The 11 isotopes with a Q-value larger than 2.0 MeV are ^{48}Ca, ^{76}Ge, ^{82}Se, ^{96}Zr, ^{100}Mo, ^{110}Pd, ^{116}Cd, ^{124}Sn, ^{130}Te, ^{136}Xe, and ^{150}Nd. Most of them are currently part of a $0\nu\beta\beta$ experimental programs. Table 1.1 reports an inventory of the some present active $0\nu\beta\beta$ projects. They are in different phases of development, ranging from data taking to initial R&D.

Table 1.1: Compilation of the some present active initiatives searching for $0\nu\beta\beta$. For each of them, it is reported the candidate isotope, the used technique, the status and the location

Project	**Isotope**	**Technique**	**Status**	**Location**
GERDA [58]	^{76}Ge	^{enr}Ge semicond. det.	Upgrade to Phase II	LNGS
Cuore-0/Cuore [59]	^{130}Te	TeO_2 bolometers	Data taking Commissioning	LNGS
MAJORANA [60]	^{76}Ge	^{enr}Ge semicond. det.	Commissioning	SURF
SuperNEMO [61]	^{82}Se	^{enr}Se foils/tracking	R&D, Construction	LSM
EXO-200 [62]	^{136}Xe	Liq. ^{enr}Xe TPC/scint.	Data taking	WIPP
KamLAND-Zen [63]	^{136}Xe	^{enr}Xe in liq. scint.	Data taking	Kamioka
SNO+ [64]	^{130}Te	Nd loaded liq. scint.	R&D, Construction	SNOLAB
CANDLES [65]	^{48}Ca	CaF_2 scint. crystals	R&D, Construction	Kamioka
Cobra [66]	^{116}Cd	CZT semicond. det.	R&D	LNGS

The observation of the $0\nu\beta\beta$ in different isotopes is mandatory to confirm and certify a discovery.

If neutrinos are Majorana particles, measuring the effective Majorana mass provides information on the neutrino mass scale and hierarchy. This is possible because there is a relationship between the effective Majorana mass and the mass of the lightest neutrino [8]. Fig.1.6 shows the range of allowed values for $m_{\beta\beta}$ for each value of lightest neutrino masses. There are distinct bands of allowed $m_{\beta\beta}$ depending on the hierachy. The bands overlap in the degenerate mass regime. Present neutrinoless double beta decay experiments set upper limits on $m_{\beta\beta}$ [67].

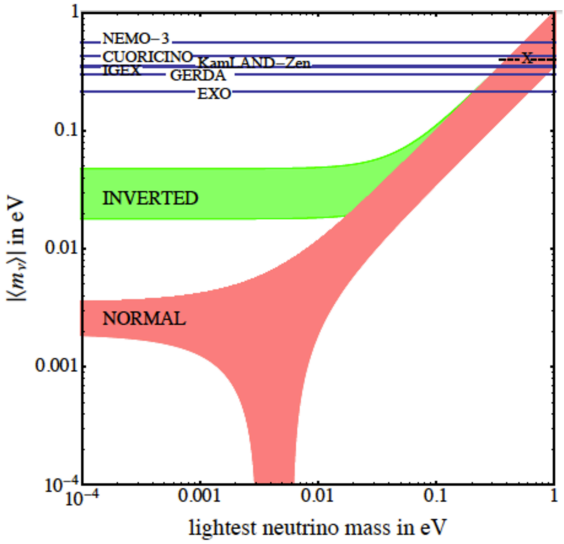

Figure 1.6: Allowed values for the effective Majorana mass as a function of the mass of the lightest neutrino. The green band represents the allowed value in the case of inverted neutrino mass hierarchy, while the red band is for the normal hierarchy case. The limits to $m_{\beta\beta}$ from CUORICINO [68], IGEX [69] , NEMO-3 [70], KamLAND-Zen [63], EXO and GERDA [58] $0\nu\beta\beta$ experiments are shown [67].

1.6 Nuclear matrix elements

The major source of uncertainty converting the half-life of $0\nu\beta\beta$ process into a neutrino mass is given by the involved nuclear transition matrix elements (see eq.1.9). A precision of about 20-30% on the nuclear matrix elements is mandatory to guarantee a reasonable accuracy in the conversion from half-lives to neutrino masses.

1.6.1 Transition operators

Before proceeding with the discussion on the nuclear matrix elements, the type of transition operators entering the $0\nu\beta\beta$ decay process will be summarized, reported the formulation of Simkovic et al. [56].
The transition operator in momentum space, $p = |\vec{q}|$, is written as:

$$T(p) = H(p) f(m_i, U_{ei})$$

where for light neutrino exchange

$$f(m_i, U_{ei}) = \frac{< m_\nu >}{m_e}, \qquad < m_\nu >= \sum_{k=light} (U_{ek})^2 m_k$$

while for heavy neutrino exchange

$$f(m_i, U_{ei}) = m_p \langle m_\nu^{-1} \rangle, \qquad \langle m_{\nu_h}^{-1} \rangle = \sum_{k=light} (U_{ek})^2 \frac{1}{m_{k_h}}$$

The operator $H(p)$ consist in a combination of Fermi (F), Gamow-Teller (GT) and tensor (T) ones:

$$H(p) = \sum_{n,n'} \tau_n^\dagger \tau_{n'}^\dagger [-h^F(p) + h^{GT}(p) \vec{\sigma}_n \cdot \vec{\sigma}_{n'} + h^T(p) S_{nn'}^p] \tag{1.11}$$

with the tensor operator:

$$S_{nn'}^p = 3[(\vec{\sigma}_n \cdot \hat{p})(\vec{\sigma}_{n'} \cdot \hat{p})] - \vec{\sigma_n} \cdot \vec{\sigma}_{n'} \tag{1.12}$$

The Fermi h^F, Gamow-teller h^{GT}, and tensor h^T are given by [56] and can be further factorized as:

$$h^{F,GT,T}(p) = v(p) \tilde{h}^{F,GT,T}(p) \tag{1.13}$$

$\tilde{h}^{F,GT,T}(p)$ are the form factor. A list of form factors is given in Ref. [56, 71]. The $v(p)$ is called the neutrino potential. The expression of $v(p)$ for light neutrino exchange and right neutrino exchange is reported in Ref.[56, 71]. Therefore, the nuclear matrix element $M^{0\nu}$ consists of the Fermi (F), Gamow-Teller (GT) and tensor parts as:

$$M^{0\nu} = -\left(\frac{g_v}{g_A}\right)^2 M_F^{0\nu} + M_{GT}^{0\nu} + M_T^{0\nu} \tag{1.14}$$

where $g_V = 1.0$ and $g_A = 1.25$ are the vector and axial coupling constants, respectively.

1.6.2 $0\nu\beta\beta$-decay nuclear matrix elements

Interpreting existing results as a measurement of $| < m_\nu > |$ and planning new experiments depend crucially on the knowledge of the corresponding nuclear matrix elements (NMEs) that govern the decay rate. The NMEs for $0\nu\beta\beta$-decay must be evaluated using tools of nuclear structure theory. Till now there are no observables that could be directly linked to the magnitude of $0\nu\beta\beta$-decay nuclear matrix elements and, thus, could

be used to dermine them in a essentially model independent way. As a consequence, the the evaluation of the matrix element is presently limited to model calculations. The calculation of the $0\nu\beta\beta$ NMEs is a difficult problem because ground and many excited states (if closure approximation is not adopted) of open-shell nuclei with complicated nuclear structure have to be considered. The frameworks used for estimating the matrix elements have been largely provided by the Quasi-Particle Random Approximation (QRPA), the nuclear shell model (NSM), the neutron-neutron Interacting Boson Model (IBM-2), Projected Hartree-Fock-Bogoliubov Method (PHFB) and Energy Density Functional Method (EDF).

- The QRPA [13, 14] constructs ground state correlations by iterating two-quasiparticle excitations on top of BCS or HFB vacuum, then imposes a quasiboson approximation on the excitation. It is successful in describing overall features of nuclear properties. QRPA depends on some simplifying assumptions and is thus often not quantitatively accurate in describing the details of nuclear structure. On the other hand, large model spaces can easily be accommodated.

- In Shell Model calculations [12] the interactions are described by an effective Hamiltonian which is diagonalized over all configurations of a chosen subset of valence single-particle states. The shell model can generally describe nuclear structure more quantitatively, but there are limits in the model space of orbitals that can be included in the calculations.

- Detailed aspects of nuclear structure can also be described using the so-called algebraic approaches, where the Interacting Boson Approximation (IBA) [15] has been found to be very useful. The basic idea of this model is a truncation of the very large shell model space to states built from pairs of nucleons with $J = 0$ and 2, followed by a replacement of those pairs with bosons. The boson Hamiltonian and electromagnetic transition operators are then fit to low-lying collective states in nuclei near the one of interest. It does an excellent job in reproducing trends for spectra and $E2$ transitions involving collective state across isotope and isotope chains.

- In the PHFB [16] wave functions of good particle number and angular momentum are obtained by projection on the axially symmetric intrinsic HFB states. In

application to the calculation of the $0\nu\beta\beta$ NMEs the nuclear Hamiltonian was restricted only to quadrupole interaction. The PHFB is restricted in its scope. With a real Bogoliubov transformation without parity mixing one can describe only neutron pairs with even angular momentum and positive parity.

- The EDF [17] is considered to be an improvement with respect to PHFB. The density functional methods based on the Gogny functional are taken into account [72]. The particle number and angular momentum projection for mother and daughter nuclei is performed and configuration mixing within the generating coordinate method is included. A large single paricle basis (11 major oscillator shells) is considered.

The differences among the listed methods of NMEs calculations for the $0\nu\beta\beta$-decay are due to following reasons:

- The mean field is used in different ways. As a result, single particle occupancies of individual orbits of various methods differ significantly from each other [73].
- The residual interactions are of various origin and renormalized in different ways.
- Various sized of the model space are taken into account.
- Different many-body approximations are used in the diagonalization of the nuclear Hamiltonian.

Each of the applied methods has advantages and drawbacks, whose effect in the values of the NME can be sometimes explored. The advantage of the ISM calculations is their full treatment of the nuclear correlations, which tends to diminish the NMEs. On the contrary, QRPA, EDF and IBM underestimate the multipole correlations in different ways and tend to overestimate the NMEs. The drawbacks of the ISM are related to the limited number of orbits in the valence space and they are as consequence the violation of Ikeda sum rule and underestimation of the NMEs.
Accurate determination of the NMEs, and a realistic estimate of their uncertainty is of great importance. Nuclear matrix elements need to be evaluated with uncertainty of less than 20 - 30% to establish the neutrino mass spectrum and CP violating phases of the neutrino mixing.

1.6.3 Constrains and uncertainties in calculated NMEs

The improvement on the calculation of the $0\nu\beta\beta$-decay NMEs is very important and challenging problem. The uncertainty associated with the calculation of the $0\nu\beta\beta$ decay NMEs can be diminished by suitably chosen nuclear probes. Complementary experimental information from related processes like charge-exchange and particle transfer reactions, muon capture and so on are used [18–22].

Till now, the most helpful experimental constraint comes from measured $2\nu\beta\beta$ rates. While certain aspects like the effect of correlations on two-neutrino and neutrinoless matrix elements are similar, there are fundamental differences between the two processes, for example caused by the quite different amount of linear momentum available in the intermediate channel. Indeed, the matrix elements of the $2\nu\beta\beta$ decay process are calculated by allowing for the virtual excitation of states in the intermediate nucleus between the parent and the daughter. Since the momentum provided by one of the beta decays is of the order of $\sim$1 MeV/c, only the lowest multipolarities (0^+, 1^+ states) at the lowest excitation energies can contribute significantly. For $0\nu\beta\beta$ decay, the two neutrons decaying into protons emit virtual neutrinos that must annihilate in a short distance ($\sim$ 2 fm) within the nucleus and such a distance implies high virtual momenta, up to $\sim$ 100 MeV/c. Consequently, the multipolarities involved in the intermediate virtual excitation can be quite high (up to $l = 8$) and a broadening of the excited states of the intermediate nucleus can be quite large ($\sim$ 20-30 MeV). Because of these differences, it does not seem reasonable to assume that a theory successfully describing the matrix elements for double beta decay with neutrinos represents any assurance that the same method can also reliably predict the neutrinoless mode [22].

High precision experimental information from single charge-exchange are used to constraint the calculations. But this approach works only if the $0\nu\beta\beta$ shows single state dominance in the intermediate channel. Actually it has been shown that the $2\nu\beta\beta$ proceeds through low-lying (Fermi Surface) states [74], in agreements with observations by charge exchange reactions.

In addition some common assumption in the different competing calculations could causes overall systematic uncertainties [8], above all the closure approximation and quenching of g_A.

The $0\nu\beta\beta$-decay matrix elements are usually calculated using the closure approxima-

tion for intermediate nuclear states. Within this approximation energies of intermediate states $(E_n - E_i)$ are replaced by an average value $E \sim 10$ MeV, and the sum over intermediate states is taken by closure, $\sum_n |n><n| = 1$. This simplifies the numerical calculation drastically. The calculations with exact treatment of the energies of the intermediate nucleus were achieved within the QRPA-like methods [73, 75, 76]. The effect of the closure approximation was studied in detail in Ref. [77].

Regarding the quenching phenomenon, it is well known that the calculated strengths of Gamow-Teller β-decay transitions to individual final states are significantly larger than the experimental ones. That effect is known as the axial-vector current matrix elements quenching. To account for this, it is customary to quench the calculated GT matrix elements up to 70%. Formally, this is accomplished by replacing the true value of the coupling constant $g_A = 1.269$ by a quenched value $g_A^{eff} = 1.0$. The origin of the quenching is not completely known. This effect is assigned to the Δ-isobar admixture in the nuclear wave function or to the shift of the GT strength to higher excitation energies due to the short-range tensor correlations. Quenching is very important for the double beta decay because g_A^{eff} appears to the fourth power in the decay rate. If it occurs also for the $0\nu\beta\beta$-decay, it could significantly reduce the $0\nu\beta\beta$-decay half-life by as much as a factor of 2-3. The axial-vector coupling constant g_A^{eff} or, in other words, the treatment of quenching, is also a source of differences in the calculated $0\nu\beta\beta$-decay NMEs [71].

The estimated matrix elements $M^{0\nu}$ for light neutrino exchange are shown in Fig.1.7 [71], where the NMEs obtained though IBM-2, QRPA [76] and ISM [78]. It is possible to note in Fig.1.7 that the comparison between different models shows discrepancy factors higher than two [67]. Therefore, it is not at all clear that any of the calculations is near the truth, the ambiguities in the models are still too large and the constraints too loose to reach accurate values of the NMEs.

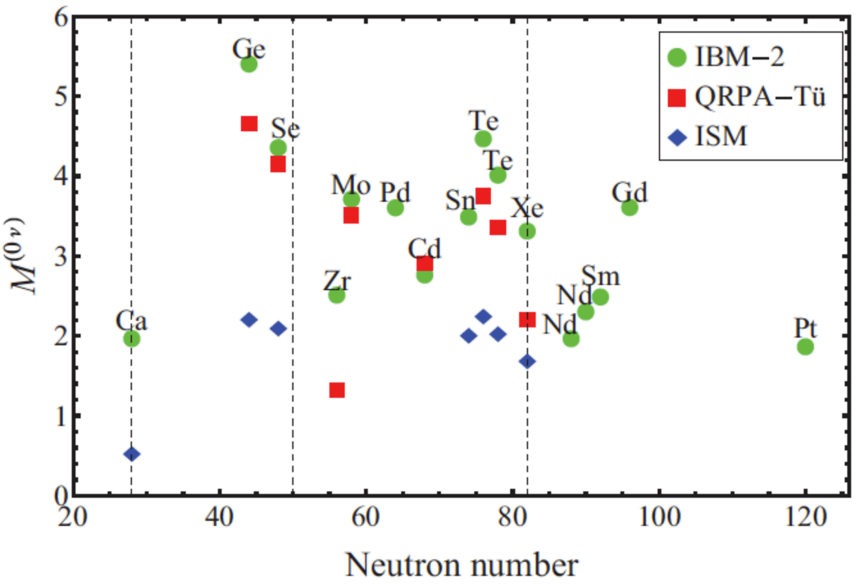

Figure 1.7: Nuclear matrix element $M^{0\nu}$ for $0\nu\beta\beta$ decay in IBM-2 [71] compared with QRPA [76] and ISM [78].

From the experimental point of view, in literature very few experimental tests of transitions that change nuclear charge by two units are present. For example, the double pion charge exchange might be used to test $\beta\beta$ decay transition matrix elements was rather quickly debunked, due to the very different nature of the operators and momentum transfers. In the next Chapter, the past experimental attempts to deduce the NMEs will be discussed and a novel idea to use nuclear reactions induced by heavy-ion accelerated beams as a tool to determine the $\beta\beta$ decay nuclear matrix elements will be described.

Chapter 2

The double charge exchange reactions

As discussed in Chapter 1, the evaluation of the $0\nu\beta\beta$-decay nuclear matrix elements are essential for extracting neutrino masses. The experimental study of nuclear transitions, where the nuclear charge is changed by two units leaving the mass number invariant, in analogy to $\beta\beta$ decay, could give important information. In nature the Double Charge Exchange reactions (DCE) are the only nuclear processes that have this characteristic and can be investigated in laboratory.

In the past, many attempts to study DCE using pion beams via the (π^+, π^-) or (π^-, π^+) reactions were done [23–26], but all of these were unsuccessful. Despite pion double charge exchange, involves the transformation of two neutrons into two protons, like $\beta\beta$-decay, the responsible nuclear operators have very different structure in the two cases [8]. Moreover, the pion has zero spin, therefore pions are unlikely to excite the fundamental spin-flip GT excitations.

Over the years, only very few explorative studies of DCE processes induceed by heavy-ion were performed. Most of them were not conclusive because of the very poor yields in the measured energy spectra and the lack of angular distributions, due to the very low cross-sections involved. Due to discouraging results the study on DCE and its relation with $\beta\beta$ decay was not carried out. Nowadays the situation is more favourable, thanks to the advent of new facilities for the detection of the reaction products, which could allow to face the experimental challenges and to extract quantitative information from DCE reactions.

In this Chapter, an overview on the state of the art of heavy-ion DCE will be presented, describing the past attempts and above all the renewed interest of the scientific community in the recent years. Then the similarities among the heavy-ion DCE reaction and $0\nu\beta\beta$ decay will be investigated. Finally the best experimental conditions to study the DCE processes will be discussed and the first pioneering study on the heavy-ion DCE performed at LNS-INFN will be presented.

2.1 The Heavy-Ion Double charge exchange reaction

Double charge-exchange reactions (DCE) are characterized by the transfer of two units of the isospin third component ($\Delta T_z = \pm 2$), leaving the mass number unchanged;

$$a(N_a, Z_a) + A(N_A, Z_A) \rightarrow b(N_a \pm 2, Z_a \mp 2) + B(N_A \mp 2, Z_A \pm 2)$$

The interest in double charge exchange comes from three important features:

- the possibility to investigate unstable nuclei even by using stable beam nuclei and/or target;
- the possibility to probe two-nucleon pairing correlations inside nuclei;
- their connection with $\beta\beta$ decay.

The latter aspect is the idea at the basis of the study presented in this thesis.

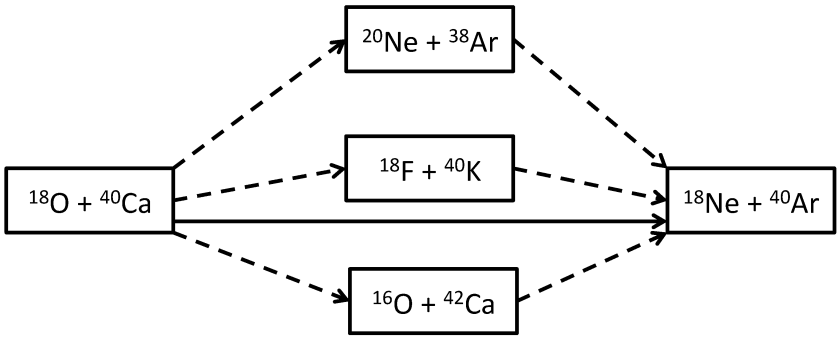

Figure 2.1: Sketch of the main channels involved in the ^{40}Ca(^{18}O, ^{18}Ne)^{40}Ar.

In analogy to the single charge-exchange reactions, DCE can proceed both via an exchange of mesons induced by isovector components of nuclear force (direct mechanism) or by the exchange of nucleons in multi-step transfer processes (sequential mechanism).

These reaction mechanisms have quite different origin: the meson exchange one is a typical nucleon-nucleon collision process, while the multi-nucleon transfer is triggered by the action of the mean field of the colliding nuclei.
An example of a DCE reaction is the ^{40}Ca(^{18}O,^{18}Ne)^{40}Ar one, which is studied in the present thesis work. The most relevant involved channels in this case are indicated in Fig.2.1. It is of particular importance to know the experimental conditions where the meson exchange mechanism is dominant, since the desired nuclear structure information connected with the $\beta\beta$ decay is available only from the direct process. The two mechanisms contribute coherently to the cross section.

2.1.1 Past attempts

There are very few instances of reported heavy-ion induced double charge exchange reactions. To our knowledge, the first case was (^{18}O, ^{18}Ne) on ^{24}Mg and ^{26}Mg [79], but these experiments were characterized by high background and very low collected yield (see Fig.2.2).

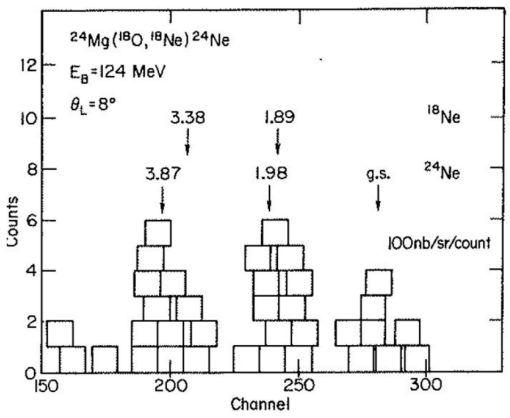

Figure 2.2: The ^{24}Mg(^{18}O, ^{18}Ne)^{24}Ne at 124 MeV and 8° (lab) [79].

Another interesting work was performed by Drake et al. [27], about the (^{14}C,^{14}O) reaction on ^{40}Ca at 51 MeV. The choice of the T =1 ^{14}C beam was motived by the authors since the ground state transitions ^{14}C→ ^{14}O is a double analog transition between members of the same isospin triplet. In addition, the ^{14}O has no particle-stable excited states, and clean spectra of residual nuclei populated in the (^{14}C,^{14}O) reaction can be extracted by missing mass technique. The transitions to the 0^+ ground state

and first 2^+ state (1.46 MeV) of ^{40}Ar were studied (see Fig.2.3).

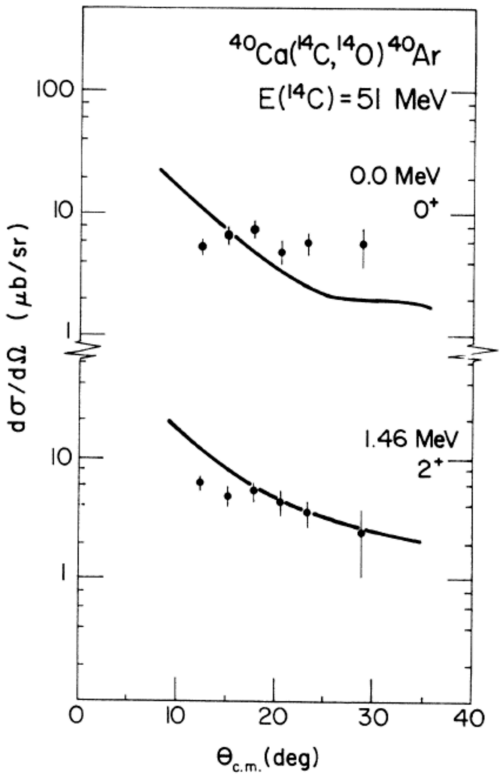

Figure 2.3: Theoretical angular distribution obtained for the excitation of the 0^+ and 2^+ states in the ^{40}Ca(^{14}C,^{14}O)^{40}Ar reaction from Ref.[80]. Experimental data are from Ref.[27]

The cross section of the $^{40}Ar_{g.s.}$ was shown to be 5-10 μb/sr and angular distributions showed a flap shape. Dasso and Vitturi [80] performed a theoretical description of the mechanism involved. Their approach to the problem was based on the idea of treating the transition to the residual ^{40}Ar states as double-phonons built over a ^{40}Ca core. They considered these modes as independent degrees of freedom in order to describe the observed cross sections. From this study the authors concluded that the independent transfer of two neutrons and pick up of two protons from the target was the leading reaction mechanism. An indication favouring such two-step description was provided by the appreciably large cross section, measured in the same experiment of the two-proton pick-up reaction ^{40}Ca(^{14}C,^{16}O)^{38}Ar ($\sim$ 1 mb/sr). This could signal that the transit through the two-proton transfer channel is well favoured in the DCE reaction

close to the Coulomb barrier.

As a sequel to this experiment, ^{14}Be by the similar ^{48}Ca(^{14}C, ^{14}Be) reaction at 87.4 MeV was studied, but not a single ^{14}Be nucleus was detected. Since one count would have corresponded to 20 nb/sr, the authors estimated an upper limit for the cross section to 40 nb/sr [81].

In Ref. [28], the first observed double charge exchange reaction which did not proceed through an analog $\Delta T = 0$ transition from the projectile to the ejectile was described. In particular, the (^{18}O,^{18}C) reaction at 100 MeV on ^{48}Ca was studied in order to provide a measurement of the mass of the very neutron-rich ^{18}C isotope, and to shed some light on the feasibility of reactions of this type to observe other exotic nuclei.

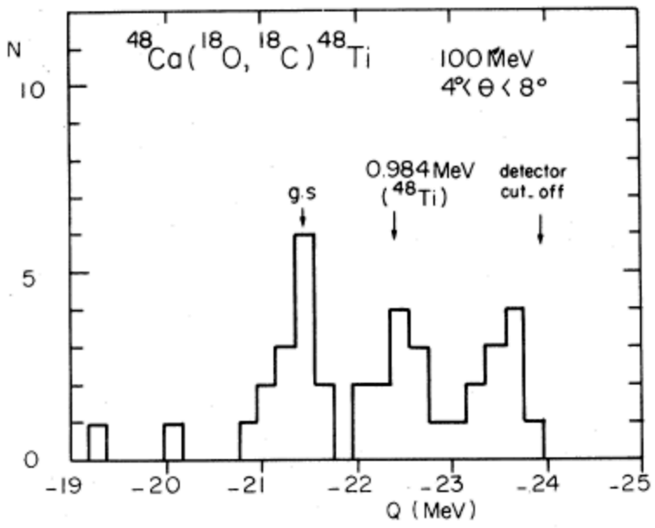

Figure 2.4: Energy spectrum of the ^{18}C nuclei emerging from the ^{18}O (100 MeV) + ^{48}Ca reaction. One count corresponds to a cross section of 3 nb/sr. The energy resolution is 1.1 MeV [28]

Also in this case the study was not conclusive because the reaction was characterized by a very low cross section, in fact, in the transition to the ground state 14 events were counted, which correspond to about 40 nb/sr.

Blomgren et al indicated, for the first time, a possible connection among the DCE reaction induced by heavy-ion and $\beta\beta$-decay [29]. The authors set out to study the double Gamow-Teller strength via the ^{24}Mg(^{18}O,^{18}Ne)^{24}Ne reaction at 76 A MeV. In the paper the authors showed the angular distributions for different integrated excitation energy

intervals (see fig.2.5). They concluded that the statistical uncertainty prevented any far-reaching conclusions, and the only interesting feature was the rather flat angular distributions for the low-energy excitation intervals. Moreover they deduce that in 0°-1° (C.M.) interval, the average differential cross section to states lying below the neutron breakup threshold (E_x = 8.9 MeV), where they supposed to find the significant concentration of DGT strength in ^{24}Ne, was about 20 nb/sr.

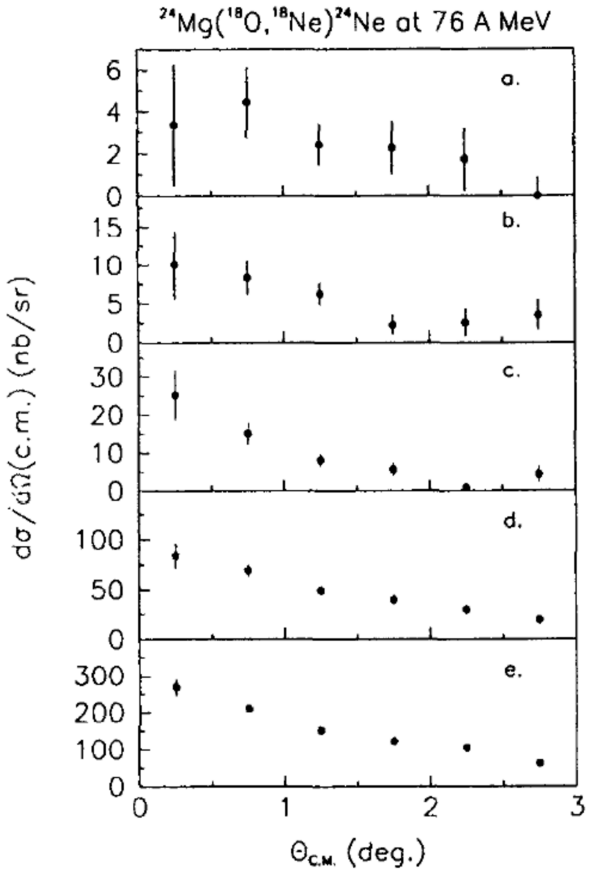

Figure 2.5: Angular distribution for different excitation energy intervals. (a) 0.0 - 4.5 MeV, (b) 4.5 - 7.5 MeV, (c) 7.5 - 10.0 MeV, (d) 10.0 - 15.0 MeV and (e) 15.0 - 20.0 MeV [29]

There, the authors explained the measured low cross-section by the possibility of a destructive interference between the direct and the sequential processes. In the conclusion of this paper, the measurement of the two-proton and two-neutron transfer channel separately was also suggested.

Therefore, it is possible to conclude that in the past few not encouraging experiments have been performed and most of them were not conclusive because of the very low cross-sections, ranging from about 4 - 50 nb/sr [28, 29] to 10 μb/sr [27] involved and the consequent lack of measurements of angular distributions.

2.1.2 Recent attempts

The interest in the study of the heavy-ion double charge exchange reaction is still alive as demonstrated by recent activity reports [82–84]. Indeed, Matsubara et al., have recently used heavy-ion double charge exchange (^{18}O,^{18}Ne) reaction as probe to study neutron rich nuclei. The authors have focused their attention on investigations of unbound ^{9}He and ^{12}Be nuclei populated through the stable ^{9}Be and ^{12}C ones. The experiment was performed at Research Center for Nuclear Physics (RCNP) of the Osaka University. A primary beam of ^{18}O was accelerated at 80 MeV/u. The ejectiles were detected and analyzed by the Grand Raiden spectrometer. Fig.2.6 shows preliminary excitation energy spectrum for the (^{18}O,^{18}Ne) reactions at 0° on ^{9}Be and ^{12}C.

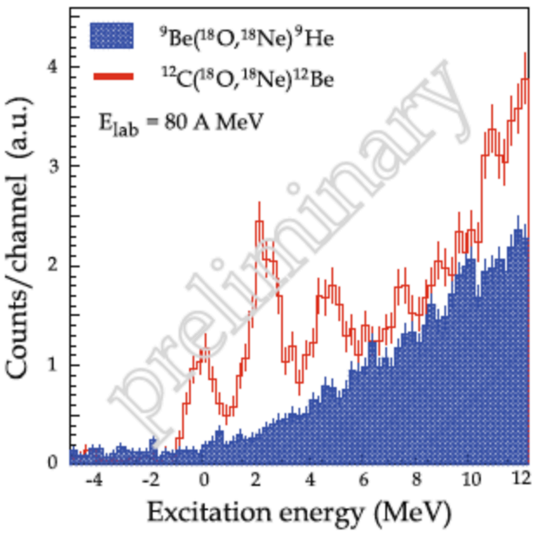

Figure 2.6: Excitation energy spectra of ^{9}He and ^{12}Be for the (^{18}O, ^{18}Ne) reactions at 0° on ^{9}Be and ^{12}C, respectively.[82]

The authors have also measured the cross-section angular distribution for the different observed transitions in the case of ^{12}C(^{18}O, ^{18}Ne) reaction. The different shapes of the angular distributions suggest a sensitivity to multipolarities. (Fig.2.7)

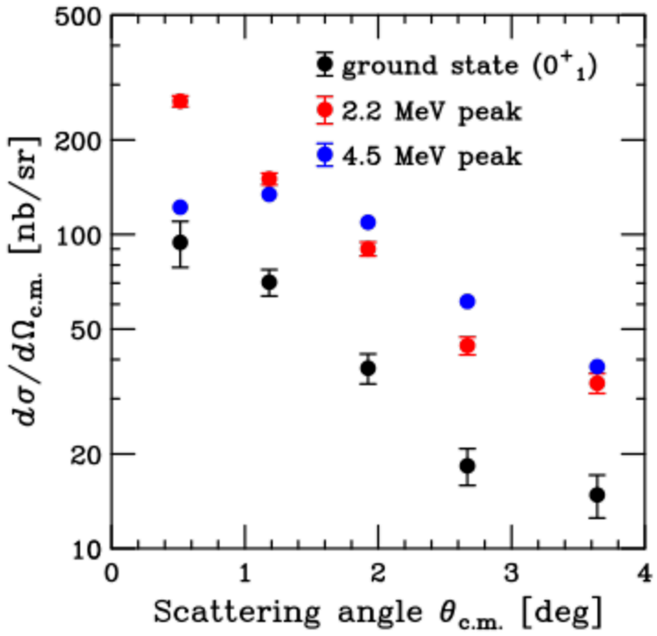

Figure 2.7: Angular distributions of differential cross sections for the ^{12}C(^{18}O, ^{18}Ne)^{12}Be reaction at 80 MeV/u for the observed three peaks: the ground state (closed black circle), the 2.2 MeV peak (closed red circle) and the 4.5 MeV peak (closed blue circle) [83]

The authors conclude that the present result is a valid benchmark for developing the DCE reaction model and that DCE reaction can be a powerful spectroscopic tool for unstable nuclei.

2.2 DCE reactions and $0\nu\beta\beta$ decays

The novel idea at the basis in the present thesis is to use, for the first time, double charge exchange reactions induced by heavy-ion accelerated beams as a tool to determine the $\beta\beta$ decay nuclear matrix elements. As discussed before, these are processes characterized by the transfer of two units of the isospin component (two protons transformed into two neutrons or vice versa). In the boson exchange model of nuclear interaction DCE are determined by the exchange of two isovector mesons as π, δ and ρ.
Despite the basic interaction is different in DCE compared to the $0\nu\beta\beta$ decay, there are a number of important similarities among them:

- Parent/daughter states of the $0\nu\beta\beta$ are the same as those of the target/residual nuclei in the DCE;
- Short range Fermi, Gamow-Teller and rank-2 tensor components are present in both the transition operators, being their relative weight tunable in DCE by changing the incident energy;
- In $0\nu\beta\beta$ decaying nuclei, the momentum of the neutrino in the intermediate channel is estimated by the uncertainty principle. Assuming a finite range of about 2 fm, a momentum spread of the order of 0.5 fm^{-1} is extracted, which in turns corresponds to about 100 MeV/c [67]. The momentum available for the neutrino in the intermediate channel is also available for the nuclear wave function in order to preserve momentum conservation.
  DCE process is also a finite range one, since the same two nucleons converted in $\beta\beta$ decay are involved, the momentum spread of the same amount is present for the same reason in the intermediate channel. Therefore, both DCE and $0\nu\beta\beta$ operators map the same portion of nuclear wave function in momentum space. This is a crucial similarity since other processes cannot probe this feature [85].
- The two processes are non-local and are characterized by two vertices localized in the same pair of valence nucleons. Indeed the $\beta\beta$-decay is a process where an even-even nucleus in its 0^+ ground state is transformed into another even-even nucleus in its 0^+ ground state. The same kind of nuclear transitions can be studied by a DCE reaction. The only way to obtain such transition from a 0^+ ground state in an initial nucleus to a 0^+ ground state in a final nucleus is to act on a pair of valence nucleus. Otherwise, the final populated state would be either not 0^+ or not the ground state.
- Both processes take place in the same nuclear medium. In medium effects are expected to be present in both cases, so DCE data could give a valuable constraint on the theoretical determination of quenching phenomena (described in Section.1.6) on $0\nu\beta\beta$ decay.
- An off-shell propagation through virtual intermediate channels is present in the two cases. The virtual states do not represent the asymptotic channels of the reaction and their energies can be different from those (measurable) at stationary

conditions. Indeed, in the limited time during which they live, the energy-time uncertainty principle allows that the energy balance can be violated of an amount given by $\Delta E \Delta t \sim \hbar$ in the sense described in Ref.[86]. In practice, a supplementary contribution of several MeV to the line width is present in the intermediate virtual states. This is related to the transit time of a particle (neutrino in one case and a pair of nucleons in the other) along the distance of the two vertices of the $0\nu\beta\beta$ and DCE processes. The situation is very different in single charge exchange reactions, where intermediate states of $0\nu\beta\beta$ are populated as stationary ones and in $2\nu\beta\beta$, where the neutrinos and electrons are projected out from the nucleus, No effective broadening of the line width is thus probed by this lhe processes.

Thus, even if the two processes are mediated by different interactions, the involved nuclear matrix element are connected and the determination of the DCE reaction cross sections can give important information on the $\beta\beta$ matrix elements. Indeed, the difference in the coupling constants between weak and strong interaction does not enter in the NMEs, being part of the $G_0^{0\nu\beta\beta}$ phase space factor in the expression of the $0\nu\beta\beta$ half-life. The description of NMs extracted from DCE and $0\nu\beta\beta$ presents the same degree of complexity, with the advantage for DCE to be "accessible" in laboratory.
Despite a detailed study of the relation among $\beta\beta$ decay and the heavy-ion induced DCE cross section by modern theoretical approach is still missing, a simple relation between DCE cross sections and $\beta\beta$-decay half-lives is not trivial and needs to be explored. In Chapter 6 an innovative technique to infer the nuclear matrix elements by measuring the cross-section of a double charge-exchange nuclear reaction will be discussed [87].

2.3 Optimal experimental conditions to study the DCE processes

As discussed in Section 2.1.1 the past attempts to study heavy-ion induced double charge-exchange reactions (DCE) were not conclusive. Nowadays the use of modern high resolution and large acceptance spectrometers allows to face the experimental challenges and to extract quantitative information from DCE reactions. Indeed, the measurement of DCE high resolution energy spectra and accurate cross sections at

very forward angles are crucial to identify the transitions of interest. Furthermore the concurrent measurement of the other relevant reaction channels allows to isolate the direct DCE mechanism from the competing transfer processes.
In order to select the best experimental conditions to investigate DCE process, several aspects regarding the structure of the involved nuclei and the dynamical conditions have to be considered, as explained in the following subsections.

2.3.1 The choice of the projectile

As written before, the DCE reaction rates are expected to be small. A way of increasing them is to use as a projectile and ejectile nuclei which belong the same SU(4) multiplet in spin S and isospin T. This is in practice fulfilled only when the projectile and ejectile are located symmetrically around $N = Z$. The (^{18}O,^{18}Ne) is particularly advantageous because:

- The ^{18}O is the lightest non-radioactive $T = 1$ nucleus so it can be easily produced with high intensities.
- The $J^{\pi} = 1^{+}$, $T = 0$ to $J^{\pi} = 0^{+}$, $T = 1$ transition in A = 18 shows particularly good SU(4) symmetry in that nearly 100% of the GT sum-rule strength $3(N-Z)$ [88] is exhausted by the lowest energy 1^{+} state [89]. The ^{18}O, (0^{+}, $T = 1$) to ^{18}Ne (0^{+}, $T = 1$) double GT transition through the intermediate ^{18}F (1^{+}, $T = 0$) state provides a particularly strong and simple transition for this study. Furthermore the state at 1.05 MeV exhausts the Fermi strength [89].
  A schematic view of the ^{18}O$\rightarrow$ ^{18}F $\rightarrow$^{18}Ne is shown in Fig.2.8, where the GT strength for involved two-step in the transitions are also indicated.

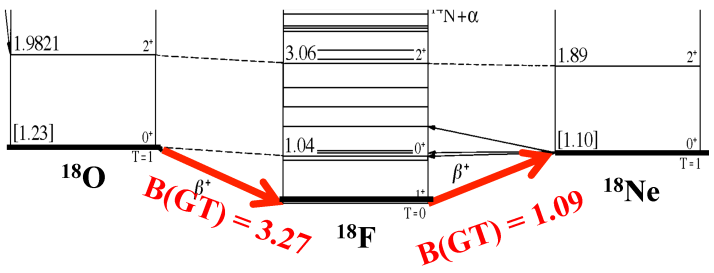

Figure 2.8: Scheme of the ^{18}O $\rightarrow$ ^{18}F $\rightarrow$ ^{18}Ne projectile transition

This reaction allows to populate target-residual system in the $\beta^+\beta^+$ kind, while most of the research on $0\nu\beta\beta$ is on the opposite side. It is important stressing that none of the reactions of $\beta^-\beta^-$ kind looks like as favourable as the (^{18}O,^{18}Ne). For example the (^{18}Ne,^{18}O) requires a radioactive beam, which cannot be available with comparable intensity. On the other hand, the reaction that use a stable beam, such as (^{20}Ne,^{20}O) or the (^{12}C,^{12}Be) have smaller $B(GT)$, so a sensible reduction of the yield is foreseen in these cases.

2.3.2 The choice of the target

From the target point of view, in principle, it would be convenient that the complementary double GT channel in the target is as strong as possible. The target used in the reaction studied in this work is $T = 0$ ^{40}Ca. In this case, the ^{40}Ca $\rightarrow$ ^{40}Ar DCE transition is not double analog transition between members of the same isospin multiplet since $T(^{40}\text{Ca}) = 0$ while $T(^{40}\text{Ar}) = 2$, thus the GT transition are not super allowed as in the case of the projectile. On the other hand, in order to carry out a study on DCE process the ^{40}Ca target turns out to be an optimal choice. First and foremost, the Fermi transition is exhausted by the 0^+ at 4.4 MeV [90] and the GT strength in not much fragmented in the intermediate channel. Indeed the high resolution ^{40}Ca(^{3}He,t)^{40}Sc data not yet published from Y. Fujita et al. [90], show that the GT strength is manly distributed in the ^{40}K 1^+ states up to excitation energy of $\sim$ 8 MeV. In particular, the state at 2.73 MeV is strongest 1^+ state, which carries a strength of $B(GT; 2.73) = 0.069 \pm 0.006$, but there are other ten satellites of the fragmented GT strength. The two largest ones are the states at 2.33 and 4.40 MeV, which account for $B(GT; 2.33) = 0.014 \pm 0.001$ and $B(GT; 4.40) = 0.018 \pm 0.002$, respectively. These data are in agreement to previous results taken from literature: the ^{40}Ca(p,n)^{40}Sc reaction at 134 MeV from [91] and at 159 MeV from [92]. Chittrakarn et al. [91] give zero-degree cross section 0.48 mb/sr and a value of $B(GT; 2.73) = 0.084$ for the transition to the 1^+ state of ^{40}K at 2.73 MeV. Taddeucci et al. [92] also show that the GT strength is concentrated to the transition 1^+ state of ^{40}K at 2.73 MeV , but the authors give zero-degree cross section 1.2 mb/sr and a value of $B(GT; 2.73)$ = 0.21 for the transition to the 1^+ state of ^{40}K at 2.73 MeV. To be thorough, the result of B. K. Park et al [93] should be also cited. The authors extract $B(GT; 2.73)$ = 0.14 $\pm$ 0.02 from multiple decomposition analysis of the zero-degree cross section of

the ^{40}Ca(n,p)^{40}K at 170 MeV. However, the results of Park et al. could be influenced by large systematic errors, due to the poor energy resolution and the uncertainties of the multiple decomposition analysis. The high resolution experiment of Fujita confirm the GT strength distribution in the different transitions of ^{40}K and agrees with the obtained value of Chittrakarn about the GT strength.
A schematic view of the ^{40}Ca $\rightarrow$ ^{40}K $\rightarrow$ ^{40}Ar is shown in Fig.2.9, where the GT strength for two step involved in the transition is also indicate.

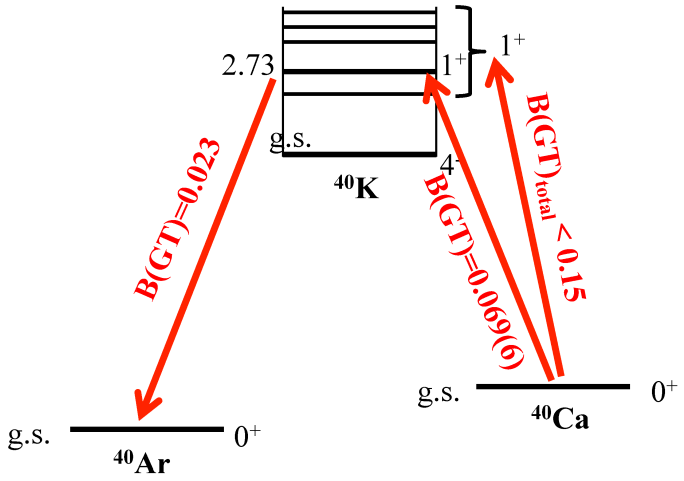

Figure 2.9: Scheme of the ^{40}Ca$\rightarrow$ ^{40}K $\rightarrow$^{40}Ar projectile transition

The small value of $B(GT)$ for the ^{40}Ca is a consequence of the Pauli blocking in this doubly magic system. In fact the wave function of ^{40}Ca$_{g.s.}$ can be expressed as:

$$|^{40}\mathrm{Ca}_{g.s.}>= 0.88|[1d_{3/2}\otimes 1d_{3/2}]^{0+}> +0.06|[1f_{7/2}\otimes 1f_{7/2}]^{0+}> +0.06|[1f_{5/2}\otimes 1f_{5/2}]^{0+}>$$

The GT and F transitions take place only through the small $1f_{7/2}$, $1f_{5/2}$ particle and $1d_{3/2}$ hole components of the ^{40}Ca$_{g.s.}$ wave function, which correspond to about 14% of the total [94, 95].
From the experimental point of view, the advantage in using ^{40}Ca target is that it can be produced with high purity, becayse it comprises about 97% of naturally occurring calcium. Regarding possible contaminants, ^{40}Ca is an easily oxidizable material and Carbon is also a typical background. However the (^{18}O, ^{18}Ne) reactions on the contaminants element in the target have a larger Q-value then ^{40}Ca one. In fact the ^{40}Ca(^{18}O, ^{18}Ne)^{40}Ar is characterized by a quite low Q-value ($\sim$ -5.9 MeV), while the ^{16}O(^{18}O,

^{18}Ne)^{16}C and ^{12}C(^{18}O, ^{18}Ne)^{12}Be ones have a Q-value of about -24.53 MeV and -31.175 MeV, respectively. Therefore the data characterized by a excitation energy of ^{40}Ar up to 18 MeV are originated only from the reaction on ^{40}Ca.

2.3.3 The choice of beam energy and matching condition

The choice of the proper beam energy is crucial in order to favour the experimental conditions suitable for studying the direct process involved in DCE reactions. Since our intent is to explore the double GT and F transitions, it is necessary to work in conditions where the sequential transfer of the pair is suppressed and the direct charge-exchange route is dominant. An accurate prediction of the conditions where it happens is beyond the present possibilities of the theory. Nevertheless, simple estimations of both the contributions to the cross-section can be done. In particular, to study the transfer mechanism one can use the well established Brinks kinematical matching conditions that relate the cross section to the reaction Q value and the angular momentum transferred [96]. Using beam energy of 270 MeV and following the Brink's kinematical conditions results that:

- the ^{40}Ca(^{18}O, ^{18})^{40}Ar reaction proceeding via two proton transfer and two neutron pick-up is matched at $Q_{opt} \sim 50$ MeV and favoured at L transfer of $L_{opt} \sim 6$.

- the ^{40}Ca(^{18}O, ^{18})^{40}Ar reaction proceeding via two neutron transfer and two proton pick-up is matched at $Q_{opt} \sim 55$ MeV and favoured at L transfer of $L_{opt} \sim 6$.

Therefore, the sequential transfer processes to ^{40}Ar ground and low lying states are very mismatched.
A simple model describes the direct channel as sequential two single charge-exchange routes. It is known in single charge exchange reaction that, the shape of the cross section for a zero angular momentum transfer ($L = 0$) (Fermi o Gamow-Teller) is in general given by a square of Bessel function ($J_0(qR)$):

$$F(q,\omega) \sim \left| \frac{\sin(qR)}{qR} \right|^2 \tag{2.1}$$

where q is a linear momentum transfer and R is the radius $R = R_0\left(A_T^{1/3} + A_P^{1/3}\right)$. This procedure is known to work well for the direct single charge-exchange, as shown in Fig.2.10.

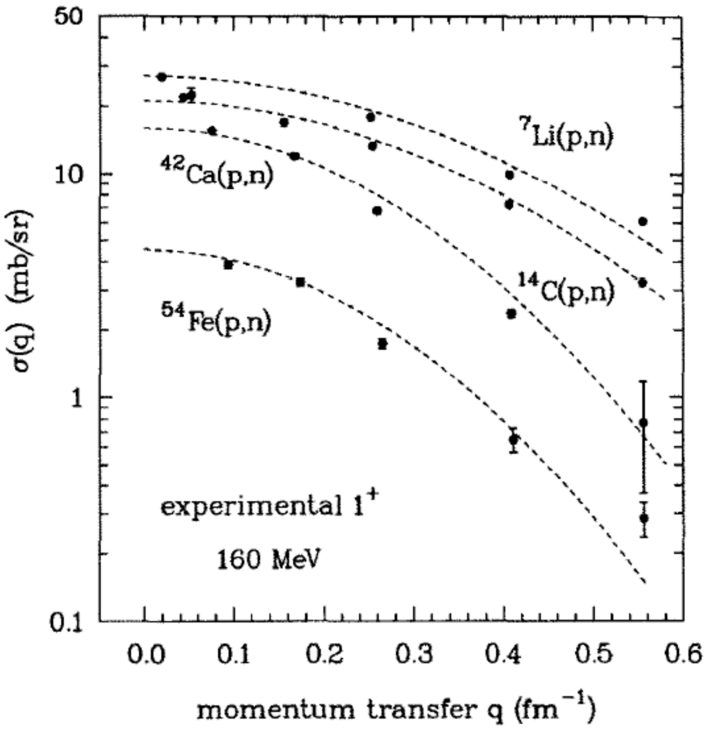

Figure 2.10: Gaussian dependence of the differential cross section on the momentum transfer. [97]

Under the hypothesis of DCE proceedings via two single charge-exchange, one can estimate the shape of the direct DCE cross-section as:

$$F(q,\omega) \sim \left| \sqrt{\frac{\sin(q_1 R)}{q_1 R} \frac{\sin((q-q_1)R)}{(q-q_1)R}} \right|^2 \sim \left| \frac{\sin(qR)}{qR} \right|^2 \tag{2.2}$$

where q_1 and q are the momentum transferred in the first step and in the overall transition, respectively.

Thus, the shape of the angular distribution for the transition ^{40}Ca(^{18}O,^{18}Ne$_{g.s.}$)^{40}Ar$_{g.s.}$ should have the trend of bessel function for L=0.

2.3.4 Studying the DCE process via (^{18}O,^{18}Ne) on ^{40}Ca at 270 MeV

In the present thesis is described the first pioneering DCE measurement, performed at INFN-LNS (Catania, Italy). In experiment a ^{18}O Cyclotron beam at 270 MeV incident energy collided on a ^{40}Ca target. In order to estimate the contribution of the concurrent channels also the ^{40}Ca(^{18}O,^{20}Ne)^{38}Ar two-proton transfer reaction, the ^{40}Ca(^{18}O,^{16}O)^{42}Ca two-neutron transfer reaction and the ^{40}Ca(^{18}O,^{18}F)^{40}K intermediate channel (see Fig.2.11) were studied.

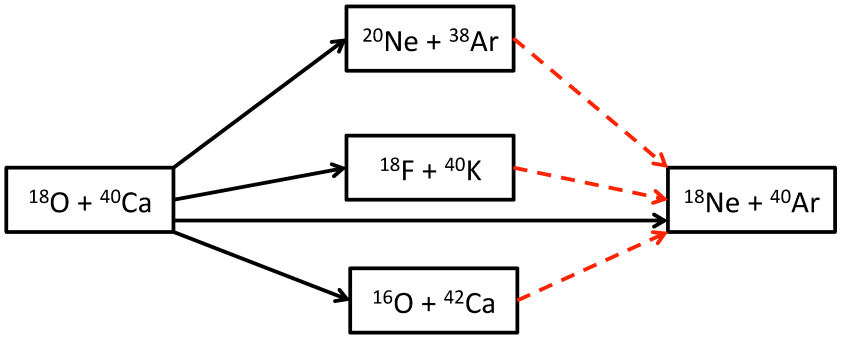

Figure 2.11: Scheme of the direct and the main sequential routes in ^{40}Ca(^{18}O,^{18}Ne)^{40}Ar. The continuum arrow indicate the measured reaction, while the dashed-red arrow the no-measured transitions

A qualifying aspect of this research is the use of the MAGNEX magnetic spectrometer. The availability of the MAGNEX large acceptance device to detect the reaction ejectiles could represent a unique opportunity to shed light on the still obscure DCE reaction mechanism. Indeed MAGNEX is an appropriate instrument to explore heavy-ion collisions characterized by cross-sections even down to 100 nb/sr or less, producing high resolution energy spectra and angular distributions, as shown in recent papers [98–100]. The details about MAGNEX will be described in the next Chapter.

Chapter 3

The Experimental Set-up

In this Chapter the experimental set-up and measurement strategy of ^{40}Ca(^{18}O,^{18}Ne)^{40}Ar Double charge-exchange (DCE) reaction performed at the INFN-LNS laboratory in Catania on April 2013 are described.
As discussed in Chapter 2 the ^{40}Ca(^{18}O,^{18}Ne)^{40}Ar DCE reaction was studied together with intermediate reaction ^{40}Ca(^{18}O,^{18}F)^{40}K single charge exchange and the competing processes: ^{40}Ca(^{18}O,^{20}Ne)^{38}Ar two-proton transfer and ^{40}Ca(^{18}O,^{16}O)^{42}Ca two-neutron transfer at 270 MeV incident energy.
Key aspects of the measure are:

- The K800 Superconducting Cyclotron (CS) for the acceleration of the required heavy-ion beams;
- the MAGNEX large acceptance magnetic spectrometer for the detection of the ejectiles.

The CS accelerator provides beams with an energy resolution of $\sim$1/1000 and emittance 5π mm$\times$mr as demonstrated in [100]. MAGNEX is a large acceptance magnetic spectrometer that allows to investigate processes characterized by very low yields. It conjugates good energy and angular resolutions with a large acceptance both in solid angle and momentum.
This experiment represents the first measurement at 0° performed by MAGNEX, therefore particular care was put on the beam transport and spectrometer setting. The experimental set-up is described in section 3.1 while sections 3.2 and 3.4 are dedicated to a concise description of MAGNEX and of its Focal Plane Detector (FPD). For further

information, a vast number of article [101–103] and PhD thesis [104, 105] are available about the facility. The section 3.5 concerns a detailed description about the technique used to set the spectrometer.

3.1 Experimental Set-up

The $^{18}O^{4+}$ beam was accelerated by the K800 Superconducting Cyclotron (CS) [106] at an energy of 270 MeV. It was transported in the MAGNEX scattering chamber without the use of any collimation system. This choice was adopted in order to avoid beam halos coming from the scattering of the primary beam on any cutting diaphragms or slits. In a previous attempts to measure at 0°, the presence of the beam halos, characterized by an isotropic distribution in energy, inside the FPD would have made prohibitive the count rate and consequently the dead time of the acquisition.

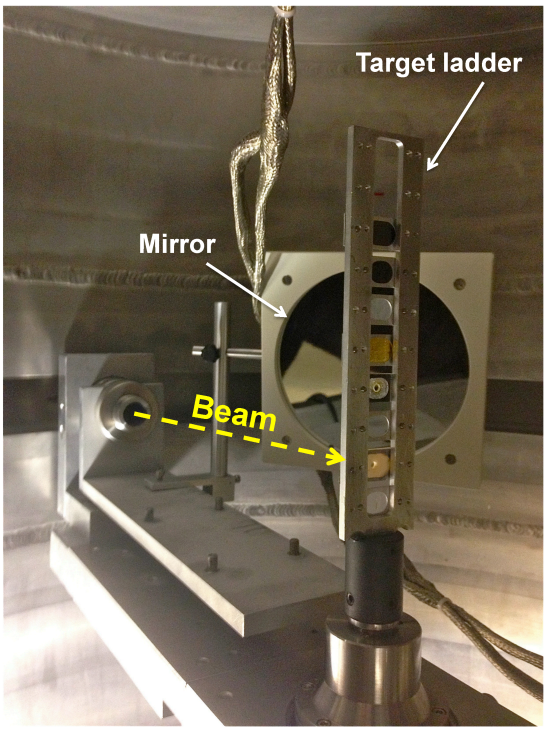

Figure 3.1: A picture inside the scattering chamber. The target ladder and the mirror system are visible. The yellow arrow indicates the beam direction.

An accurate optical alignment (∼0.1 mm) was performed in order to make the beam

hitting the target at the object point of the spectrometer. This request was checked by the use of a bubble level.

The beam spot and size were periodically checked by several alumina fluorescent targets located along the transport line and inside the scattering chamber. In particular the last alumina target (located inside the scattering chamber) was observed through mirror to estimate the beam spot size at object point of the spectrometer. A picture of scattering chamber containing the target ladder and the mirror is shown in Fig.3.1. The spot size was about 2 mm diameter, warranting a good matching with the optical properties of the spectrometer.

The target used in the experiment was a 279 $\mu g/cm^2$ ^{40}Ca film evaporated on a carbon backing of 26 $\mu g/cm^2$. Since ^{40}Ca is an easily oxidizable material, the target foil was covered by a layer of 15 $\mu g/cm^2$ carbon. The target was produced at the LNS chemical laboratory.

The ejectiles were momentum analysed by the MAGNEX spectrometer working in full acceptance mode (solid angle $\Omega \sim 50$ msr and momentum range $\Delta p/p \sim 24\%$). The spectrometer main features will be described in Section 3.2. In the DCE and two-proton transfer reactions, the optical axis of the spectrometer was centered at $\theta_{lab}^{opt} = 4^\circ$ in the laboratory reference frame, while in the two-neutron transfer and single charge-exchange reactions, it was located at $\theta_{lab}^{opt} = 7^\circ$. Considering the large angular acceptance of MAGNEX (-5.16°, +6.0° horizontal and ±7.16° vertical), these settings correspond to an angular range $0^\circ < \theta_{lab} < 10^\circ$ in the first case and $2^\circ < \theta_{lab} < 13^\circ$ in the second one. For the zero degree measurement particular care was taken to stop the beam (see Sect.3.5): the magnetic field was set in order to stop the beam inside a "big" Faraday cup (described in Section.3.5.2), placed in the focal plane area aside the Mylar entrance windows of the FPD. The current signal was then sent to a Digital Integrator [107] and was stored in the memory of a Latching Scaler [108]. In this way both the instantaneous beam current and the total collected charge were measured. A picture of the focal plane area is shown in Fig.3.2, where the "big" Faraday cup and the valve between the dipole magnet and focal plane are visible.

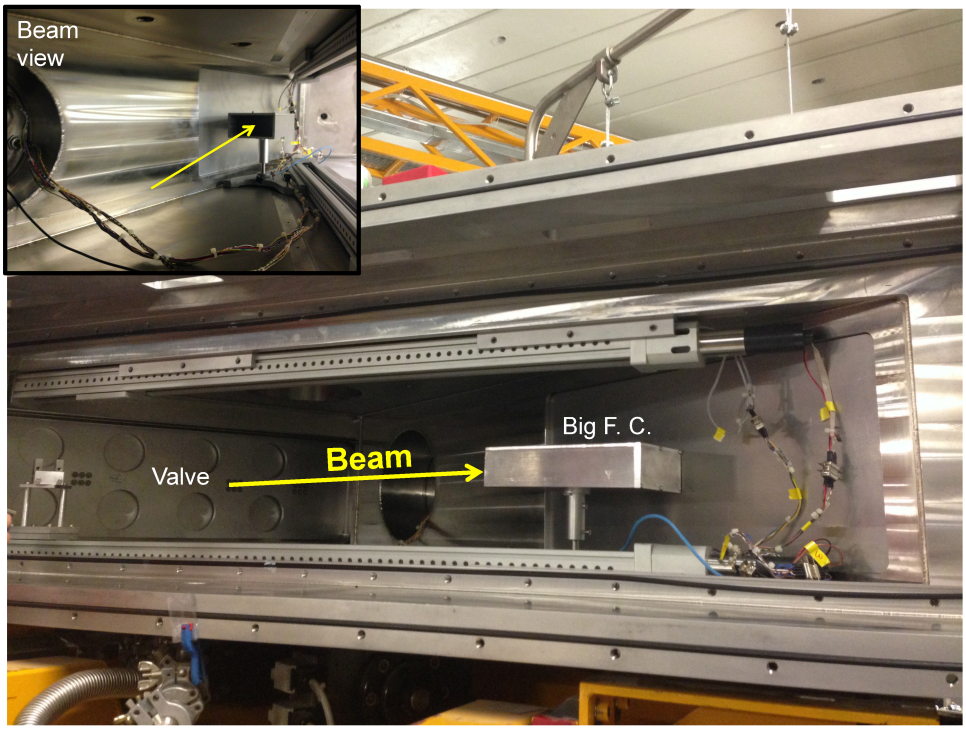

Figure 3.2: A picture of the focal plane area. The "big" Faraday Cup, the valve between the dipole magnet and focal plane are visible. In the insert the beam view is shown.The yellow arrow indicates the beam.

For the measurement at $\theta_{lab}^{opt} = 7°$, the beam intensity was measured by a 8 mm diameter Faraday cup, mounted inside the scattering chamber 15 cm downstream the target ladder along the beam direction. An electron suppressor, polarized at -200 V, was used at the entrance hole of the cup in order to enhance the efficiency of the charge collection.

The average beam intensity in ten-days experimental run was about 3-4 pnA with maximum values not exceeding 6-7 pnA, which it is the maximum rate accepted by MAGNEX FPD compatibly with the 0° measurement. Short runs at a beam current slightly above this limit demonstrated that the response of the gas section of the FPD was unacceptably deteriorated. In particular the particle identification was quickly compromised. In addition the dead time of the acquisition system and the rise of the inverse current in the silicon detectors at the end of the FPD were also prohibitive.

3.2 The MAGNEX spectrometer

3.2.1 General features

MAGNEX is a large acceptance magnetic spectrometer installed at the INFN-LNS laboratory in Catania [101, 102]. It is characterized by a high angular, mass and energy resolution in a large-accepted phase space. MAGNEX was designed to investigate several processes also characterized by very low yields in different fields of nuclear physics, ranging from nuclear structure to the characterization of reaction mechanisms in a wide interval of energies and masses. It is a high-performance device merging the advantages of the traditional magnetic spectrometry [109] with those of a large angular (50 msr) and momentum (-14%, +10.3%) acceptance detector.
From the mechanical point of view, MAGNEX is a QD spectrometer composed of two large aperture magnets, a quadrupole magnet (Q) followed by a 55° dipole (D) and a Focal Plane Detector (FPD) for the detection of the emitted ions. The apparatus is shown in Fig.3.3.

Figure 3.3: General view of MAGNEX spectrometer. From the left to the right the scattering chamber, the quadrupole (red) and the dipole (blue) magnets, and the FPD are visible.

The quadrupole magnet focus in the non dispersive (vertical) direction, while the dipole magnet provides the dispersion and the focusing strength in the dispersive direction (horizontal). The horizontal focus is obtained by the inclination of both the entrance and exit dipole boundaries by an angle of -18°. The accepted magnetic rigidities range

from $\sim$ 0.2 to $\sim$ 1.8 Tm, corresponding to energies of the detected ions ranging from $\sim$0.2 to $\sim$40 AMeV, depending on their mass and charge. A sizeable improvement in the treatment of aberrations is obtained by using special algorithms to reconstruct the relation between the initial phase space coordinates of the ions with those measured at the position of the FPD. The main actual parameter are listed in Table 3.1.

Table 3.1: Main optical characteristics of MAGNEX spectrometer.

Optical characteristics	**Actual values**
Maximum magnetic rigidity (Tm)	1.8
Solid angle (msr)	50
Horizontal angular acceptance (mr)	-90,+110
Vertical angular acceptance (mr)	$\pm$125
Momentum acceptance (δ)	-0.14,+0.1
Central path length (cm)	596
Momentum dispersion (cm/%)	3.68
First order momentum resolution	5400
Focal plane rotation angle (degrees)	59.2
Focal plane length (cm)	92
Focal plane height (cm)	20

3.2.2 Reference frame, matrix formalism and aberrations

The standard description of a beam of charged particles is done choosing one of them as the reference particle (see, e.g., Ref.[110]). Its momentum and path through the magnetic elements are the reference momentum p_0 and trajectory, respectively. The positions and momenta of the other particles are defined relative to the reference one. At any point along the reference trajectory, a longitudinal or **t** axis lying in the direction of the reference momentum is defined, while the two transverse axes **x** and **y** are chosen perpendicular to it.

In this reference frame, the momentum of a particle of the beam is decomposed in its p_x and p_y components along the x and y directions respectively and the fractional deviation δ from the reference momentum, defined as $\delta = (p - p_0)/p_0$. It is more convenient to consider the quantities $x' = p_x/p_t$ and $y' = p_y/p_t$, where p_t is the momentum longitudinal component along the reference trajectory. Since p_x and p_y are small when

compared to p_t, x' and y' can be approximated by the horizontal θ and vertical ϕ angles with respect to the reference trajectory. To have a complete phase space coordinate set it is necessary to have two more quantities: the two transverse distances of the particles from the central trajectory x and y. Summarizing, the complete phase space coordinate set for a generic particle can be written as $P \equiv (x, \theta, y, \phi, \delta)$.
In particular, as the charged particle beam moves through the spectrometer, the final position $P_f \equiv (x_f, \theta_f, y_f, \phi_f, \delta_f)$ is connected to the initial one $P_i \equiv (x_i, \theta i, y_i, \phi_i, \delta_i)$ through the relation:

$$\mathcal{M} : P_i \rightarrow P_f \tag{3.1}$$

that describes a general non-linear transport relation, characteristic of the particular optical system. More explicitly:

$$\begin{aligned} x_f &= \mathcal{M}_1(x_i, \theta_i, y_i, \phi_i, l_i, \delta_i) \\ \theta_f &= \mathcal{M}_2(x_i, \theta_i, y_i, \phi_i, l_i, \delta_i) \\ y_f &= \mathcal{M}_3(x_i, \theta_i, y_i, \phi_i, l_i, \delta_i) \\ \phi_f &= \mathcal{M}_4(x_i, \theta_i, y_i, \phi_i, l_i, \delta_i) \\ \delta_f &= \delta_i \end{aligned} \tag{3.2}$$

where the last equation expresses the conservation of the ion momentum modulus in a magnetic field, when electric fields and degrading elements are absent. Exploiting the tensor notation, eq.(3.2) can be written in terms of Taylor expansion as:

$$x_f(f) = \sum_k R_{jk}(i) x_k(i) + \sum_{k,l} T_{jkl} x_j(i) x_l(i) + ... \tag{3.3}$$

where x_j is the generic phase space coordinate and R_{jk} and T_{jkl} are the first and second order transfer matrix elements, respectively. The coefficients of the second and higher order terms in eq.(3.3) are typically referred as *aberrations*, since they determine deviations from the ideal first order optical properties. The first order truncation of eq.(3.3) gives a good description of the particle dynamics in case of magnetic spectrometers with very small angular acceptance devices [103]. The crucial problem of aberration is faced in MAGNEX, using hardware solutions and sophisticated software algorithms. From the hardware point of view, a minimization of the aberrations has been obtained with a carefully shaping the magnets and using other specific solutions [103]. For example, in order to compensate the 2^{nd} order aberration T_{126}, the FPD [111] was installed with the entrance surface rotated of θ_{tilt}=59.2° with respect to the central trajectory.
However, hardware solutions did not provide a satisfactory minimization of all the

important aberration terms, so a sophisticated software correction was implemented, based on a fully algebraic approach to determine the ion trajectory inside the spectrometer [112]. The technique, called *Ray-Reconstruction technique*, requires an accurate knowledge of the geometric and magnetic structure of the spectrometer [113–116], the use of powerful algorithms for solving the high-order transport equation [117] and the precise measurement of the ions positions and directions at the focus by a suitable FPD. The FPD detector was conceived in order to provide an accurate measurement of the final phase space vector $P_f \equiv (x_f, \theta_f, y_f, \phi_f, \delta_f)$, as described in the Section 3.4.

3.3 Ray-reconstruction technique

3.3.1 Creation of the direct transport map

The starting point of the ray-reconstruction procedure is the construction of a transport map which describes the evolution of the phase space parameters from the target point to the focal plane. Using the matrix formalism introduced in Section 3.2.2, the initial coordinates $P_i \equiv (x_i, \theta_i, y_i, \phi_i)$ are connected to the final ones $P_f \equiv (x_f, \theta_f, y_f, \phi_f)$ through the relation 3.1. For the MAGNEX spectrometer, this task is achieved using the COSY INFINITY program [118], in which the solution of equation 3.1 up to the 10^{th} order is obtained by Runge Kutta integration technique, based on the formalism of the differential algebra [117][119].

The COSY INFINITY input contains the geometry of the spectrometer (distances between the magnetic elements, length of the drift space, and slits defining the solid angle), the size and location of the FPD and the values of the quadrupole and the dipole magnetic fields, which are described as three-dimensional Enge functions [120]. Important input parameters for the creation of the transport matrices are the Effective Field Boundaries (EFB) of the dipole magnet, which are mathematically represented as 5^{th} order polynomials. In fact, there is a weak dependence of the shape of the entrance and exit EFB on the magnetic field strength and therefore they were carefully optimized for each magnetic setting looking at the resulting transport simulations, as described in the Section 4.4.1.

3.3.2 Creation of the inverse transport map

An iterative procedure implemented in COSY INFINITY allows to construct the inverse transport map $\mathcal{M}^{-1}$ up to very high order (10^{th}) in the case of MAGNEX. As a result, each initial phase space parameter, for example θ_i, is given by:

$$\theta_i = \sum_{n=1}^{10} \left(\frac{\partial^n \theta_i}{\partial x_f^m \partial \theta_f^p \partial y_f^q \partial \phi_f^r} \right)_{opt} \cdot x_f^m \theta_f^p y_f^q \phi_f^r \quad \text{with } (m+p+q+r) = n \tag{3.4}$$

The application of the inverse map to the final measured parameters allows to compensate the effect of the high order aberrations that affect the spectrometer, because they are contained in the constructed transport operator

3.4 The MAGNEX Focal Plane Detector

The MAGNEX FPD is a gas-filled hybrid detector followed by a wall of 60 silicon detectors. It measures the horizontal and vertical positions of each incident ion at four sequential points along the ions trajectory. Also, it allows to measure the energy loss in the gas region and the residual energy released in the silicon detectors wall. The FPD design and operation principle are described in details in ref.[111]. In the following Sections some of the main features are reported. A schematic view of the FPD detector is shown in Fig.3.4.

3.4.1 FPD layout

The FPD is placed 1.91 m after the exit pole face of the MAGNEX dipole. The FPD vessel is mounted on a movable carriage that can translate of ±0.08 m along to the spectrometer optical axis, in order to match the detector position to different focus conditions [101, 103]. As anticipated in Section 3.2.2, the detector is installed such that the normal to its entrance surface is rotated of 59.2° with respect to the MAGNEX central trajectory.

The drift chamber active volume is 1400 mm wide, 200 mm high, 100 mm deep with a cathode plate below (usually at applied voltage between -900 V and -1500 V) and a Frisch grid above (see Fig. 3.4). The typically used gas is 99.95% pure isobutane at pressure between 5 and 100 mbar, depending on the experiments. The gas purity

and pressure are preserved through a continuous flowing system. A 1.5 μm Mylar entrance windows of area 920×220 mm^2 separates the gas region from the vacuum. It is supported by twenty silicon coated stainless multistrands wires 0.9 mm in diameter, arranged horizontally and spaced 10 mm each other. The Frisch grid, connected to the ground, is composed by 10 gold-plated tungsten wires, 50 μm in diameter, spaced 5 mm between centers.

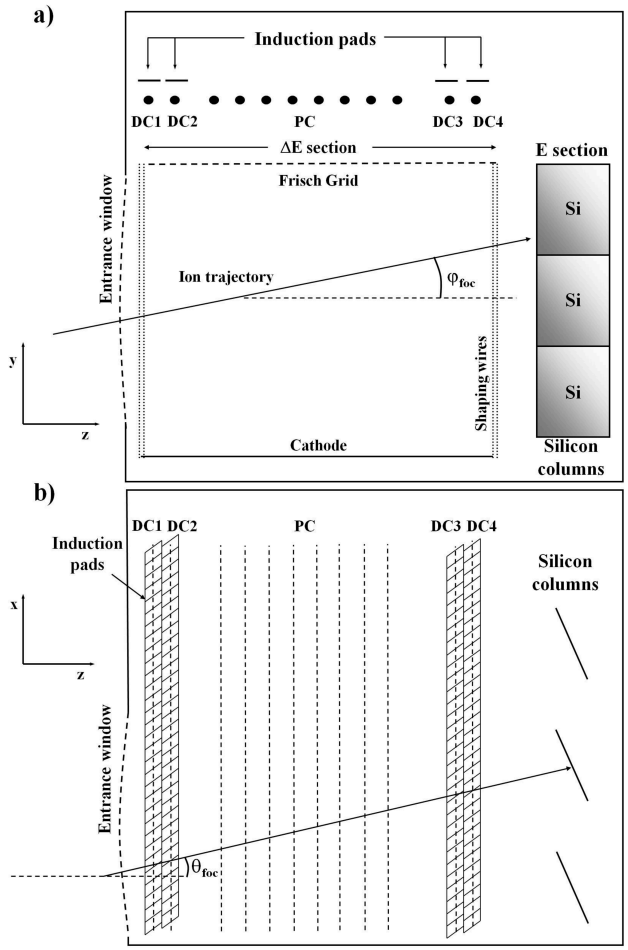

Figure 3.4: Schematic side (a) and top (b) views of the MAGNEX FPD.

The uniformity of the electric field in the region between the cathode and the Frisch grid is guaranteed by a partition grid consisting of 41 rectangular rings parallel to the cathode and arranged 5 mm one from the other.

The proportional counter section includes five sets of gold-plated tungsten amplifying wires, sequentially defined as DC_1, DC_2, PC, DC_3, DC_4 (see Fig.3.4), located 20 mm above the Frisch grid. Each DC wire is a unique amplifying wire of 20 μm diameter, while PC wires, made up of 8 single wires connected in common, are 100 μm thick. The high voltage to the proportional wires (usually form 600 V to 1300 V) is provided by a common power supply.

A set of 224 anode pads orientated along the spectrometer optical axis is located 5 mm above each DC proportional wire. Each pad is 8 mm long and 5.9 mm wide and separated by 0.1 mm from its neighbour. A picture of the anodic plate is shown in Fig.3.5.

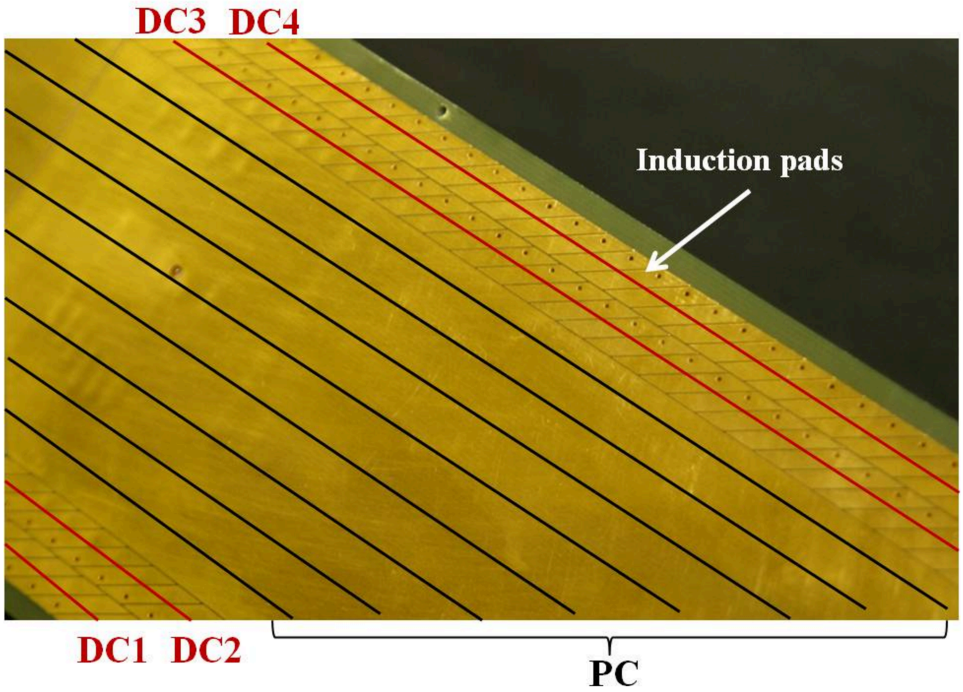

Figure 3.5: Picture of the induction plate showing the segmented pads and the DC and PC proportional wires.

A wall of 60 silicon pad detectors is located downstream of the gas detector. The silicon detectors, with an active area of 70 mm height × 50 mm width and 500 μm thickness, are arranged in 20 columns and 3 rows. The columns are mounted orthogonally to the spectrometer optical axis. A view of silicon detector wall is shown in Fig.3.6.

Figure 3.6: Picture of the FPD silicon detectors wall.

3.4.2 FPD principle of operation

The ions deflected by the dipole cross the FPD Mylar window and leave a track of ionized atoms and primary electrons in the gas (see Fig.3.4a). Under the action of the uniform electric field of about 50 V/cm, these electrons drift towards the Frisch-grid with typical velocities of 3-5 cm/µs,depending on the actual voltage and gas pressure [121]. Beyond the grid, the production of secondary electrons takes place due to the grow steeply of the electric field, in the proximity of the DC and PC wires, where a multiplication factor of about 100-200 for each primary electron occurs. The avalanche produces a signal proportional to the energy loss (ΔE_1, ΔE_2, ΔE_{PC}, ΔE_3, ΔE_4) for each event. Charge sensitive preamplifiers with a sensitivity of 200 mV/MeV (silicon equivalent) [122] are used to shape the signals, which have typical rise time of about 150 ns. The signals are split and distributed to a shaping amplifier and a constant fraction discriminator (CFD) with a 200 ns delay time. The shaped output, proportional to the energy loss and with a shaping time of 6 µs, is used for the particle identification, while the logic output, extracted only for the DC wires, is used as the stop signal for the electrons drift time measurement. A schematic diagram of the electronics and read-out of the ΔE_i measurements is shown in Fig.3.7.

The information about the horizontal position is retrieved thanks to the signal induced by the electron avalanche on the closest induction pads. These signals are then pre-amplified and shaped by an analog multiplexed read-out system based on 16 channels GASSIPLEX chips [123] mounted on the upper side of the induction pads board in the gas environment [124]. The mutiplexed signals from each of the four DC chains are read-out and digitally converted by C-RAMS modules [125]. A dedicated algorithm [126] is used to extract the center of gravity of the charge distribution at each DC section. Exploiting the regular pattern of the segmented electrode, it is possible to obtain a unique correspondence between the measured centroid and the absolute horizontal position X_1, X_2,X_3,X_4 in the MAGNEX reference frame. In this way, four position are independently determined, allowing the extraction of the horizontal and angle of the ion track at the spectrometer focal plane. Note that these measured quantities are referred to the spectrometer optical axis (X_{foc}, θ_{foc}) to be used for the ray-reconstruction.
The charged particles crossing the gas section reach the silicon detector wall. Charge pre-amplifiers [122], typically with sensitivities from 5 to 40 mV/MeV depending on the experimental needs, are used. The outputs are sent to 16-channel MEGAMP (shaping amplifier + CFD) module [127]. The shaped outputs are connected to the residual energy (E_{resid}) of ions after crossing the gas. The logic signals are used as multi-purpose timing signals of MAGNEX. The logic OR is used as start signal for the electrons drift times measurements and also to trigger the data acquisition and to generate the gate for the ΔE and drift time measurements.
The four vertical positions Y_1, Y_2, Y_3, Y_4 are extracted from the measurement of the electrons drift time in the gas region. This latter is measured by the delay between the logic signal generated by the silicon detectors (START) and the DC wires (STOP), using four TAC+ADC read-out chains. The vertical coordinates need an external absolute calibration to be correctly transformed in the optical reference frame, as described in Section 4.1. In this way, the vertical position Y_{foc} and angle ϕ_{foc} of the ion track at the focal plane are determined. The schematic diagram of the circuit read-out of E_{resid}, ΔE_i and Y_i measurements is shown in Fig.3.7.

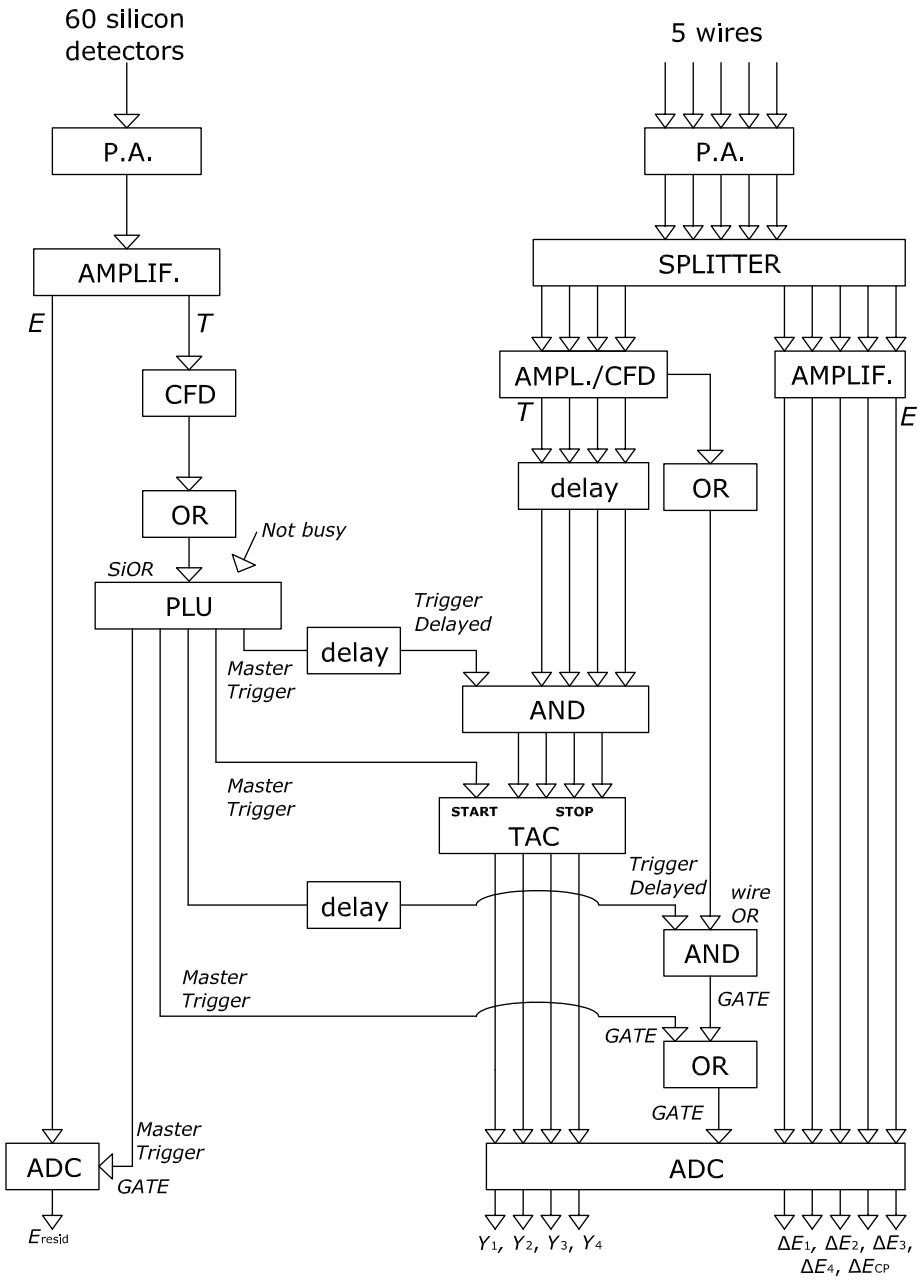

Figure 3.7: Schematic diagram of the electronics and read-out of the E_{resid}, ΔE_i and Y_i measurements.

3.5 Spectrometer setting: the 0° measurement

In this section the procedure for the spectrometer positioning and setting for the measurement at 0° it is described in details.
The magnetic fields for the quadrupole and the dipole are deduced by the focusing condition of the reaction ejectiles at the focal plane detector [105]. These magnetic fields are calculated using the COSYsetup program [128], specifically designed for searching the best parameters to set-up the MAGNEX magnetic field. When the kinematic parameters of the studied reaction and the desired δ are given as input, the COSYsetup program searches the correct setting of the magnetic fields among a set of tabulated values, calculated for several configurations. In the quadrupole, four permanent Hall probes, placed at 0.1815 m from the symmetry axis, are used to monitor long term drifts and possible hysteresis effects. The dipole magnetic field is measured by a NMR probe inserted in a socket of the magnet vacuum chamber. A detailed map of the fields given by the manufacturer and an accurate mathematical interpolation procedure makes it possible to extract for each magnet, the field at each point of the beam envelope, with an estimated error of $\sim$0.1% [114] in the 3D space.
However, in the measurement described in this thesis the choice of the magnetic setting was constrained by the necessity to stop the beam aside the FPD. In particular, two possible solution were considered to achieve this purpose:

- stop the beam inside the dipole chamber, where a series of metallic wings are present for this purpose (see Fig.3.8a);

- stop the beam downstream the dipole in a "safe" place aside the FPD.

The choice of one of the two options, strongly depends on the MAGNEX angular positioning. Fig.3.8 shows two schematic plan view of the spectrometer: in panel a) it is rotated by a negative angle with respect to the (fixed) incident beam in the laboratory, while in panel b) it is rotated by a positive angle. In order to stop the beam inside the dipole it is appropriated consider the configuration shown in Fig.3.8a, while to stop the beam in a safe area downstream the dipole the configuration in Fig.3.8b. Two different options at θ_{opt} = -4° and θ_{opt} = 4° were studied.

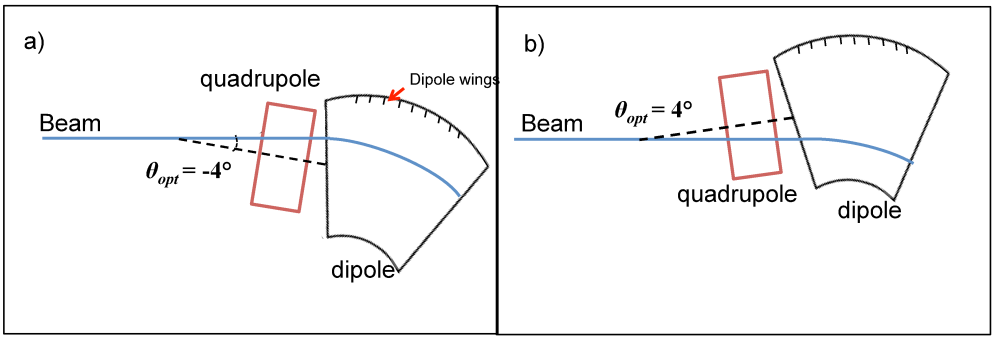

Figure 3.8: Plane view of the MAGNEX spectrometer, the blue line corresponds to the beam trajectory inside the spectrometer. Panel a) represents the configuration at θ_{opt} = -4°. Panel b) represents the configuration at θ_{opt} = 4°

3.5.1 The option at θ_{opt} = -4°.

The magnetic fields of the MAGNEX quadrupole and dipole were calculated, in order to bend the $^{18}O^{3+}$ beam up to the dipole wings, corresponding to a relative momentum of the beam at $\delta = 0.34$. The spectrometer parameters are reported in Table 3.2.

Table 3.2: Magnetic setting for the θ^{opt}_{lab} = -4° case.

δ	θ^{opt}_{lab}	**Bρ (Tm)**	**B$_Q$(T)**
0.34	-4°	0.93920	0.5205

Using this set of fields the ^{18}Ne ejectiles corresponding to the $^{40}Ar_{g.s.}$ are focused in the focal plane position corresponding to a relative momentum $\delta = 0.06$. The ejectiles of the other reactions studied in this work, are focused out of the momentum acceptance of the FPD (-0.14 < δ < +0.10), the corresponding δ are listed in Table 3.3.

Table 3.3: Position in the focal plane, in terms of relative momentum δ, for each reaction.

Reaction	δ
^{40}Ca(^{18}O,^{18}Ne)^{40}Ar	0.06
^{40}Ca(^{18}O,^{18}F)^{40}K	0.184
^{40}Ca(^{18}O,^{20}Ne)^{38}Ar	0.141
^{40}Ca(^{18}O,^{16}O)^{42}Ca	0.281

With the purpose of studying the beam trajectory, the ray-reconstruction technique was

applied to describe the evolution of the phase space parameters from the target position to the entrance, half and exit of the dipole and to the focal plane. The transport map was calculated up to 10^{th} order by COSY INFINITY program as described in Section 3.3. A set of events corresponding to the ^{18}O beam was generated by Monte Carlo routines [128] and transported through the spectrometer by the application of the direct map. In the simulations, the beam spot is very important to describe the real conditions of the transport The Cyclotron beams are characterized by an emittance of 5π mm×mr and a spot of 2 mm ($\Delta\theta$ = 2.5 mrad, $\Delta\phi$ = 2.5 mrad). In Fig 3.9 a plan view of the MAGNEX spectrometer is shown. The simulated trajectories are indicated with a green band. Under the simulated conditions the beam ions stops near the socket where the NMR probe is inserted. Consequently, the choice of stopping the beam inside the dipole was considered not convenient because could have interfered with the NMR probe.

3.5.2 The option at $\theta_{opt} = 4°$.

As discussed above, the second evaluated option consisted in stopping the beam in the area of the focal plane. In order to obtain the best focusing conditions, the magnetic fields were calculated for different values of δ. In Table 3.4 the magnetic setting for each δ are listed.

Table 3.4: Magnetic settings fot the option at $\theta_{opt} = 4°$.

δ	θ_{lab}^{opt}	$\mathbf{B\rho}$ **(Tm)**	$\mathbf{B}_Q$**(T)**
0.289	4°	0.97604	0.5409
0.239	4°	1.01588	0.5629
0.188	4°	1.05911	0.5869

For each magnetic setting the procedure described in the previous section was applied to calculate the trajectory of the beam along the spectrometer. The results in Fig.3.9 show that the best solution is obtained with δ = 0.239 (blue band) in since the beam reaches a region of the focal plane where it is possible to place a Faraday cup without creating a shadow on the FPD.
Since the beam spot at the focal plane is ∼1 cm horizontally and 0.5 cm vertically, a large Faraday cup of 105 mm wide, 55 mm high, 245 mm deep was built (see Fig.3.2).

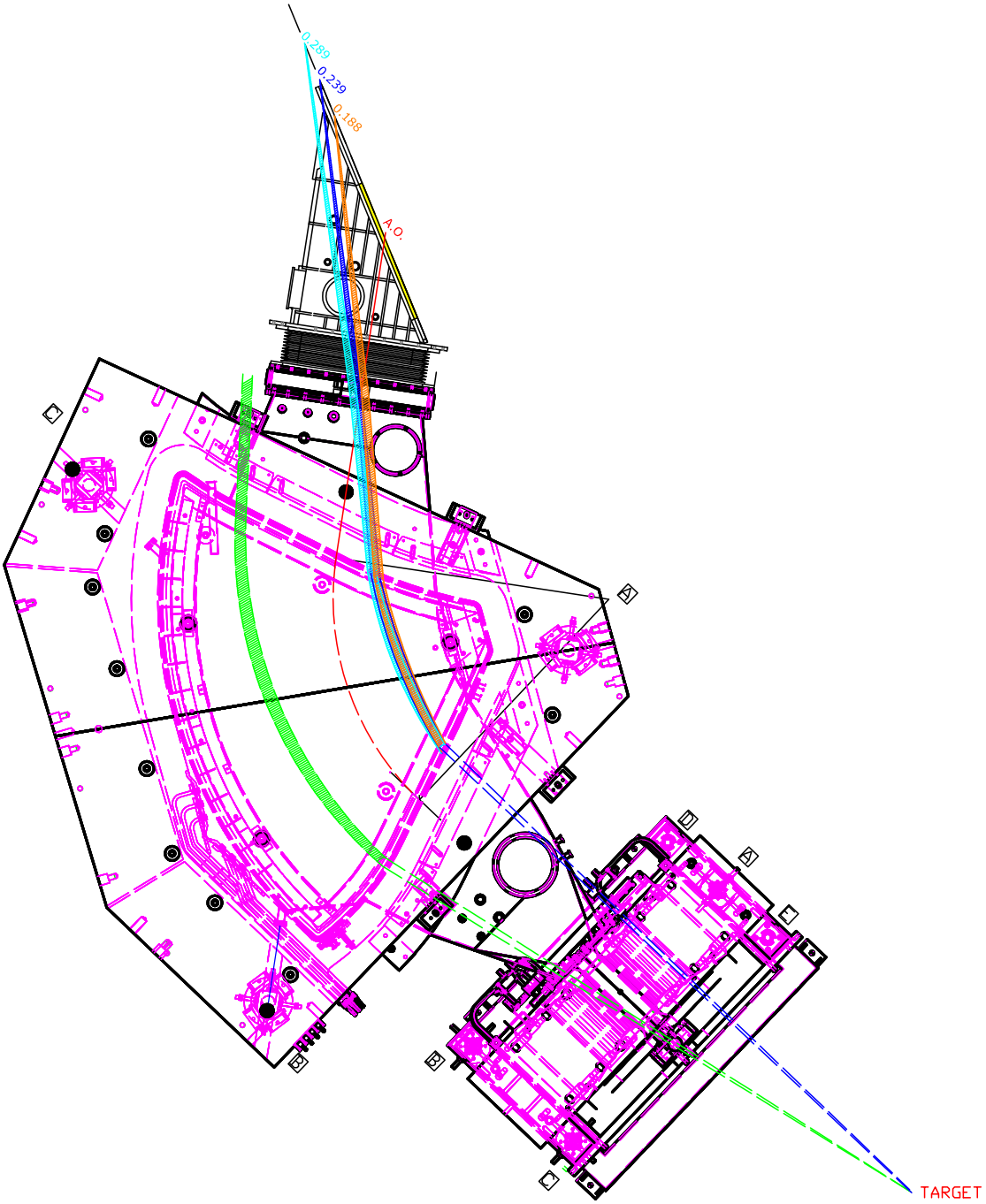

Figure 3.9: Plane view of the MAGNEX magnetic layout. The green band corresponds to the trajectory at θ_{lab}^{opt} = -4° and $\delta = 0.34$. The cyan, blue and orange bands correspond to $\theta_{opt} = 4°$ and $\delta = 0.289$, 0.239, 0.188 respectively.

A schematic view of the focal plane region is shown in Fig.3.10, in which the trajectory of the beam and the Faraday cup are also drawn.

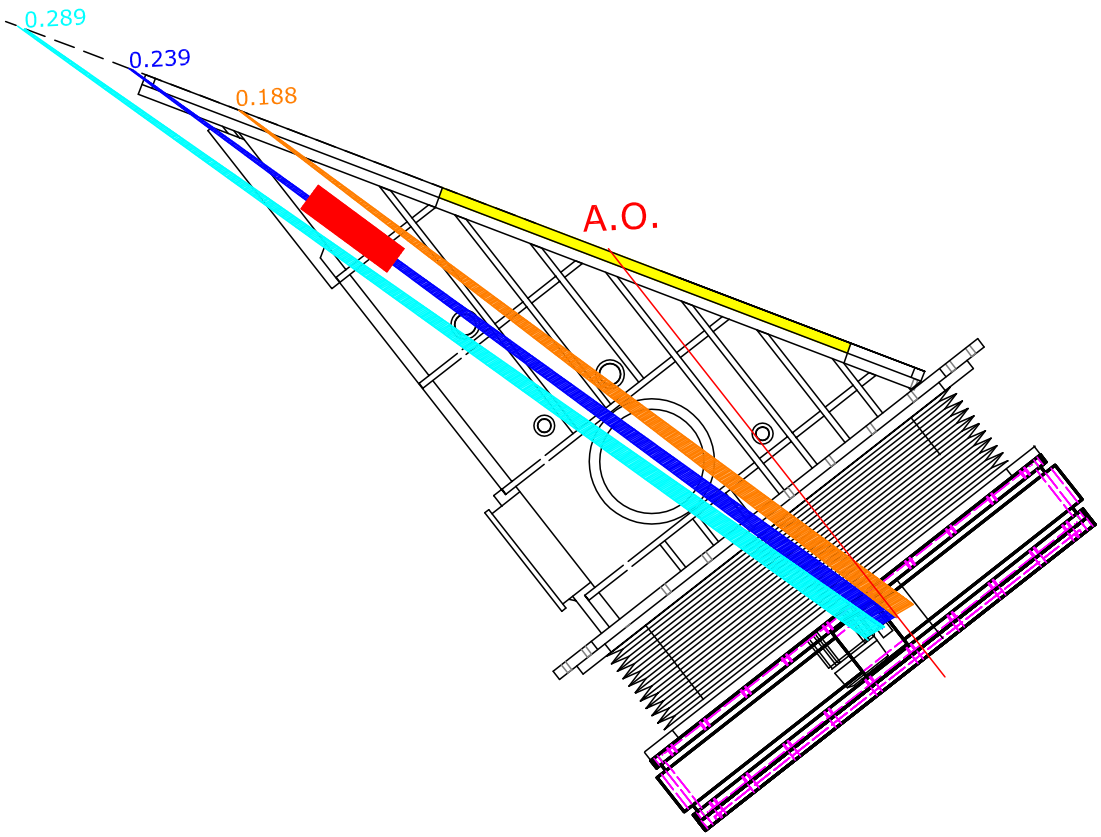

Figure 3.10: Plane view of the focal plane region. The FPD acceptance is indicated as yellow area. The cyan, blue and orange bands are the same shown in Fig.3.3. The "big" Faraday cup is represented in scale as the red rectangle.

Using this magnetic setting, the ejectiles of the reactions studied in this thesis are bent at focal plane positions corresponding to the δ values listed in Table 3.5. The ^{18}F and ^{16}O ejectiles, corresponding to the $^{40}K_{g.s.}$ and $^{42}Ca_{g.s.}$ respectively, are bent out the focal plane detector, so that it was necessary using a specific magnetic setting for these latter reactions.

Table 3.5: The position in the focal lane, in terms of relative momentum δ, for each of the listed reactions.

Reaction	δ
^{40}Ca(^{18}O,^{18}Ne)^{40}Ar	-0.02
^{40}Ca(^{18}O,^{18}F)^{40}K	0.11
^{40}Ca(^{18}O,^{20}Ne)^{38}Ar	0.06
^{40}Ca(^{18}O,^{16}O)^{42}Ca	0.18

3.5.3 The magnetic setting for the ^{40}Ca(^{18}O,^{18}F)^{40}K and ^{40}Ca(^{18}O,^{16}O)^{42}Ca reactions.

For the ^{40}Ca(^{18}O,^{18}F)^{40}K and ^{40}Ca(^{18}O,^{16}O)^{42}Ca reactions, the MAGNEX optical axis was put at $\theta_{lab}^{opt} = 7^{\circ}$, so that the beam was stopped in the Faraday cup located in the scattering chamber downstream the target ladder. The procedure used to estimate the magnetic fields is the standard one described at the beginning of this section. Therefore, the spectrometer parameter were set in order to bent the ejectiles in the focal plane position corresponding to a relative momentum δ = -0.01. The spectrometer parameters set for each reaction are listed in Table 3.6.

Table 3.6: Magnetic setting for each of the listed reactions.

Reaction	**Bρ (Tm)**	**B$_Q$(T)**
^{40}Ca(^{18}O,^{18}F)^{40}K	1.12088	0.6214
^{40}Ca(^{18}O,^{16}O)^{42}Ca	1.21284	0.6727

3.5.4 FPD setting

The FPD shift was fixed at d = -0.08 m for all the runs. The FPD was filled with 99.95% pure isobutan gas (C_4H_{10}) at 15.15 mbar pressure. The cathode was supplied at -1200 V while the Frisch-grid was grounded. The high voltage in the proportional wires DC_1, DC_2, DC_3, DC_4 and PC was +680 V, and the shaping partition grid between the Frisch-grid and the proportional wires was supplied by a separate generator at -450 V. The silicon detectors were powered with 60 V voltage to work in a full depletion mode.

Chapter 4

Data reduction

This chapter is devoted to the detailed description of the data reduction procedure, made up of several steps. First, an accurate calibration of the ions horizontal and vertical position measured by the FPD is necessary, since such parameters are used as input for the 10^{th} order ray-reconstruction procedure. These must be determined in the spectrometer reference frame, where the transport equations are defined. In addition, the ejectiles must be identified, in atomic number (Z), mass number (A) and charge (q) this is obtained by combining two techniques: the usual ΔE-E one for the Z identification and an innovative identification of the A and q based on the motion of the ions in the magnetic field of the spectrometer. Once the ions track are measured at the focal plane position, the spectrometer transport map is optimized up to 10^{th} order. This procedure completely characterizes the investigated event, providing the ion kinetic energy and scattering angle in the laboratory reference frame. Moreover, it allows to take into account the loss of the transmission efficiency through the spectrometer. This aspect is of fundamental importance in order to extract the absolute cross section of the investigated reaction. After the application of the ray-reconstruction technique to the identified data at the focal plane, the excitation energy spectra and the cross section angular distribution are extracted.

The whole procedure is described for the data collected for the ^{40}Ca(^{18}O,^{18}Ne)^{40}Ar reaction at 270 MeV. The same procedure was also applied to the other data analysed in the present work.

4.1 Calibration of the horizontal and vertical positions

4.1.1 Relative calibration of the pads response

As discussed in Chapter 3, the four horizontal positions X of the ion track inside the gas region of the FPD are given by the response of the induction pads above each DC wire. Before extracting the horizontal positions, a relative calibration of the pads response is necessary. In order to fulfill this request, four pulses of different amplitudes (2, 3, 4 and 5 V), generated by a digital pulser, were sent directly to each DC wire in a specific calibration run. In this way the same charge is instantly induced in each pad above a given wire, and the corresponding charge histograms are constructed. A reference pad is chosen for a given DC wire and a linear fit correlating the amplitudes of the charge signal for each pad with those of a reference one was performed. An example of this correlation plot is shown in Fig.4.1.

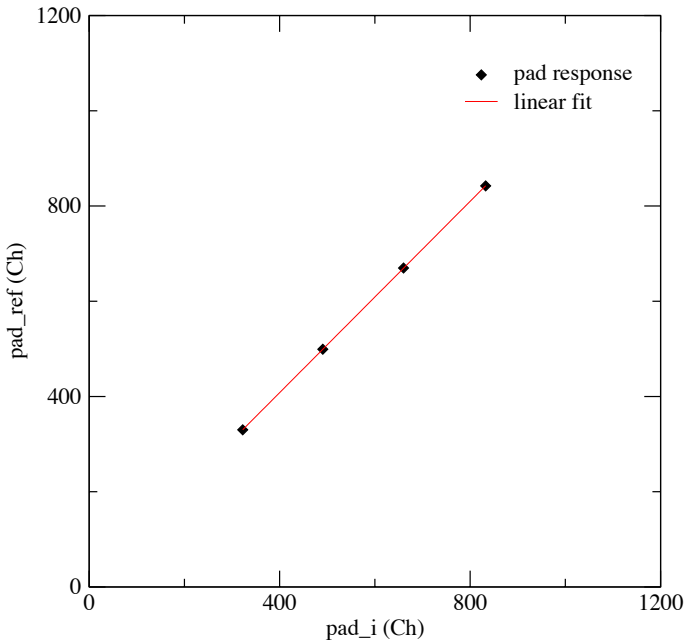

Figure 4.1: Linear fit correlating the response of a given pad with that of the reference one, induced by a common pulse in the wire of 2, 3, 4, 5 V.

After the calibration, the center of gravity of the charge distribution is extracted for each event of the collected dataset. An algorithm, specifically developed for the MAGNEX

FPD, is used for this aim. This code described in Ref.[126] takes into account the large variation of the number of excited pads as a function of the incident angle. This effect causes very different shapes of the charge distributions, thus making any standard centroid-finding algorithm [129, 130] quite unreliable.

The horizontal positions X_1, X_2, X_3, X_4 are finally determined from the corresponding centroid positions, considering that each pad is 6.00 ± 0.01 mm wide. Using the known ΔZ_i longitudinal distances (downstream the optical axis) of the DC wires with respect to DC_1, it is possible to reconstruct the ion horizontal track inside the detector. An example of the correlation between the obtained X_i positions and the Z_i distances between the 4 DCs is shown in Fig.4.2.

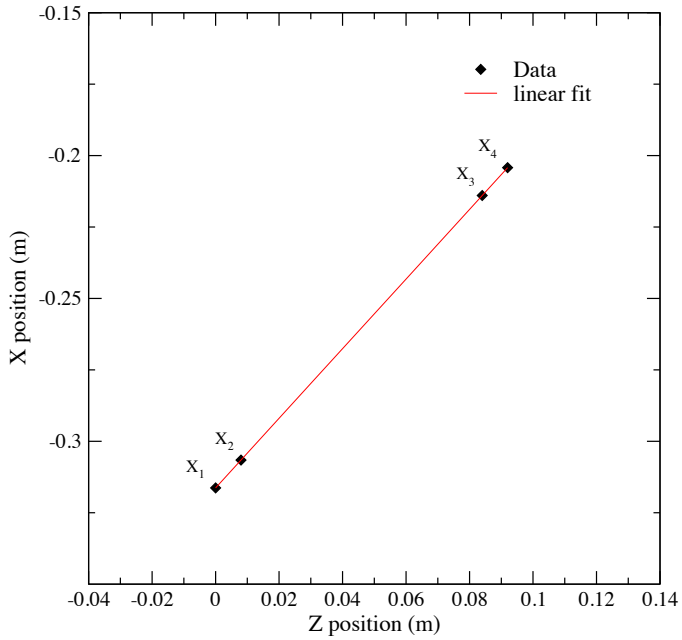

Figure 4.2: Linear correlation between the measured X_i positions and Z_i distances between the 4 DCs wires for one event. Z=0 is assumed for DC_1

.

The zero for the horizontal positions X_i are extracted by the intersection between the spectrometer optical axis, determined by a precision theodolite, and the pad-pattern above each DC_i. The X_{foc} coordinate at the focal plane is finally obtained taking into account the measured position at the FPD downstream the optical axis Z (see Fig.4.2).

The angular coefficient of the fitted line (see Fig.4.2) gives the horizontal angle θ_{foc}. The X_{foc} and θ_{foc} parameters are used as inputs for the ray-reconstruction technique.

4.1.2 Calibration of the vertical position parameter

Recalling the Section 3.4, the vertical position of the ions in the FPD is obtained at four different Z positions by the measurements of the drift times of electrons moving towards the four DC wires. The Y calibration was done taking as reference the shadows generated by the silicon coated wires used to support the Mylar window. The Mylar window and its wires support is shown in Fig.4.3.

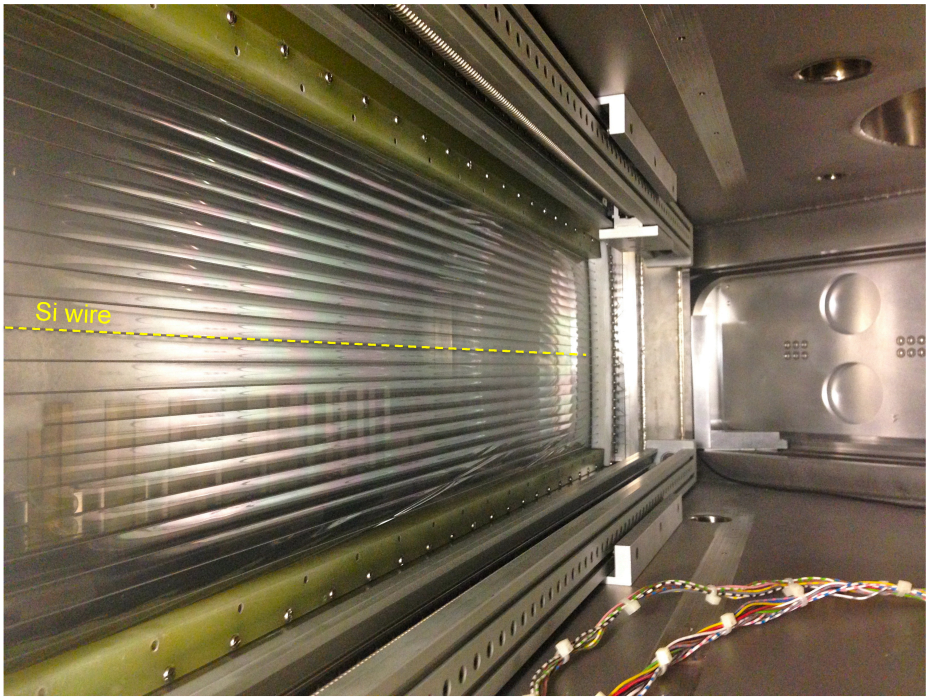

Figure 4.3: A picture of the silicon coated wires used to support the Mylar windows.

In a typical Y_i spectrum, shown in Fig. 4.4, the shadows of the wires are clearly seen as regularly spaced minima.

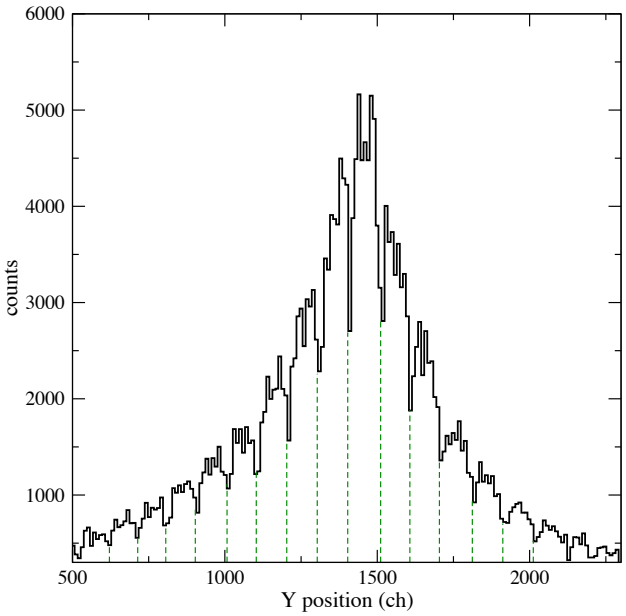

Figure 4.4: An example of Y spectrum showing the regularly spaced minima due to the shadows generated by the silicon coated wires which hold the Mylar windows. The position of the minima is indicated by the green dashed lines.

The absolute position of such wires was also determined by optical measurements in the spectrometer frame. Therefore, the final absolute calibration of the Y parameter was obtained by comparing the position of the holes in each Y_i spectrum with the known projection of the wires positions at each DC. An example of the correlation between the Y_i (ch) and the position of the silicon coated wires is shown in Fig. 4.5.

Following the same procedure adopted for the X_i calibration, the Y_i vertical positions were used to draw the ion track inside the FPD detector in the YZ plane, obtaining the Y_{foc} coordinate, while the vertical angle ϕ_{foc} is extracted from the angular coefficient of the line. An example of the correlation between the obtained Y_i positions and the Z_i distances between the 4 DCs is shown in Fig. 4.6. Both Y_{foc} and ϕ_{foc} are used as inputs for the ray-reconstruction technique.

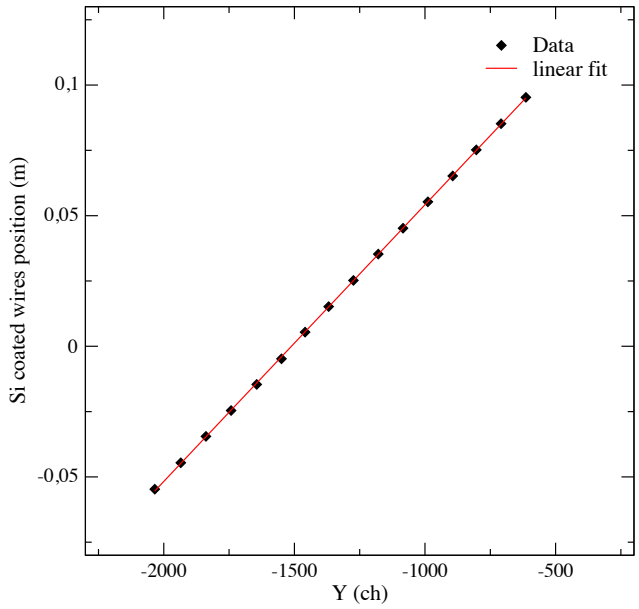

Figure 4.5: Linear correlation between the spaced minima in the Y spectrum (see Fig. 4.4 and the silicon coated wires position.

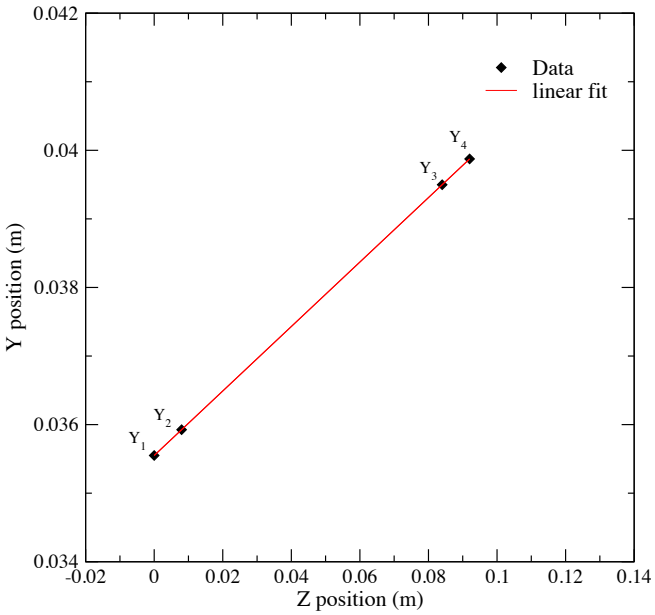

Figure 4.6: Linear correlation between the Y positions for an event and Z_i distances between the 4 DCs wires. For DC_1 $Z = 0$ is assumed.

4.2 Ejectile identification

The next step in the data reduction consists in the ejectiles identification. The procedure will be described in details for the identification of the ^{18}Ne ions.
The first step is the identification of the atomic number (Z), using the standard $\Delta E - E$ technique based on the *Bethe-Bloch formula* [131]. An example of the Z discrimination of the different ions detected for one silicon detector is shown in Fig.4.7.

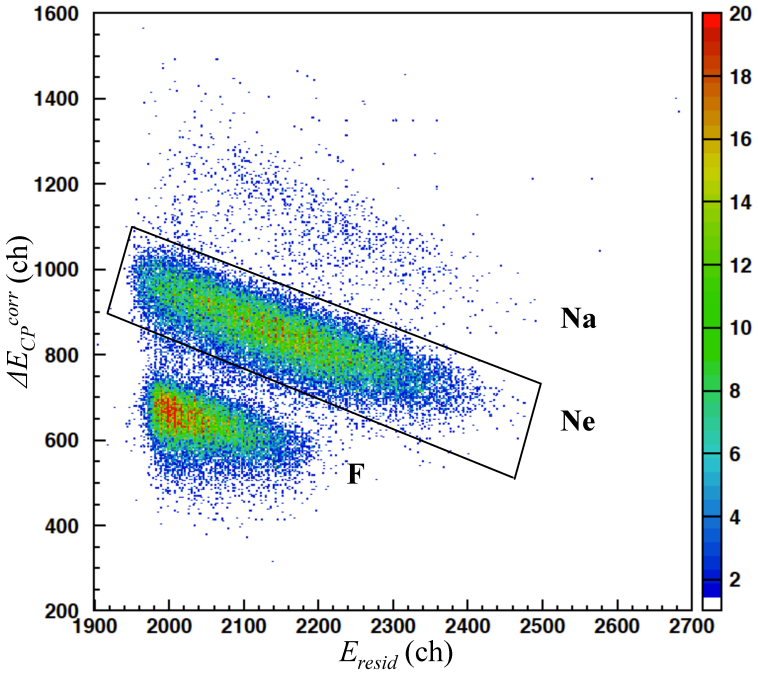

Figure 4.7: Typical $\Delta E_{CP}^{corr} - E_{resid}$ histogram plotted for the unselected ejectiles detected in the reaction ^{40}Ca + ^{18}O at 270 MeV incident energy for a single silicon detector. The different ion species and a graphical contour on the Ne region are also indicated.

The plotted parameters are the residual energy measured by the silicon detectors (E_{resid}) in abscissa, and the energy-loss in the gas measured by the CP counter, corrected for the different path lengths associated to different measured horizontal angles θ_{foc}, according to the relation:

$$\Delta E_{CP}^{corr} = \Delta E_{CP} \frac{\cos\theta_{tilt}}{\cos\theta_{foc}} \tag{4.1}$$

where θ_{tilt} is the angle between the FPD and the plane normal to the spectrometer optical axis ($\theta_{tilt} = 59.2°$).

In order to identify the different ion species a short run of elastic scattering data was performed with reduced discriminator threshold. In this way the absolute calibration of E_{resid} and ΔE_{CP}^{corr} is not necessary for identification purposes. The plot in Fig. 4.7 clarifies that the Neon isotopes locus is clearly separated by other ions loci. On the other hand the isotopic resolution for a given ion is not achievable in the $\Delta E - E$ representation.

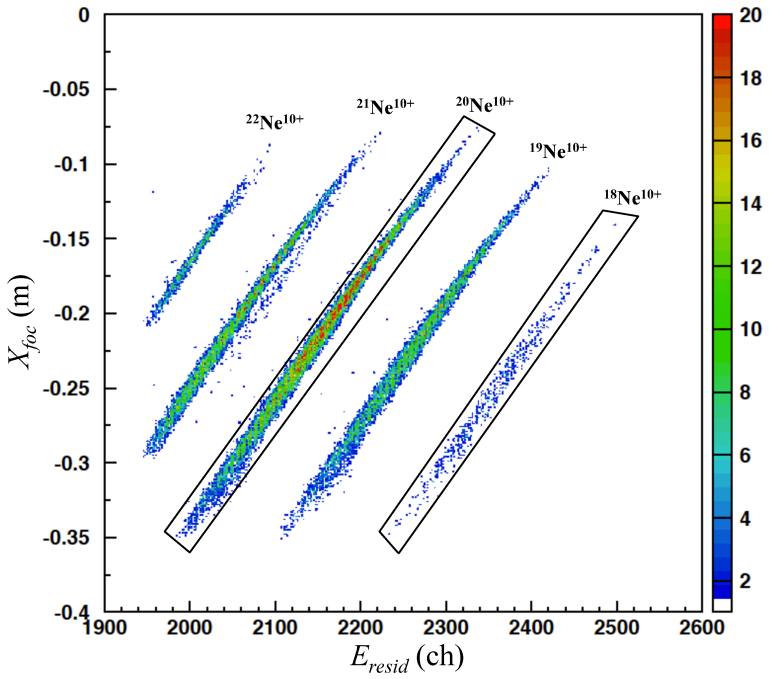

Figure 4.8: Bi-dimensional X_{foc} - E_{resid} scatter plot for a single silicon detector after selecting the Ne locus in the $\Delta E_{CP}^{corr} - E_{resid}$ plot via the graphical cut represented by the closed line in Fig. 4.7. The different Neon isotopes and two graphical contours selecting the ^{18}Ne and ^{20}Ne respectively are also indicated.

The mass number A and charge q identification is instead achieved through the correlation between the ions trajectory and their kinetic energy [132]. Such technique exploits the property of the Lorentz force, which determines the trajectory of a charged particle in a magnetic field normal to its momentum

$$\mathbf{B}\rho = \frac{\mathbf{p}}{q} \tag{4.2}$$

where $\mathbf{B}$ is the magnetic induction which forces the particle with charge q and momentum $\mathbf{p}$ to move on a trajectory with curvature radius ρ. In a non-relativistic approx-

imation, the momentum **p** is related to the kinetic energy E and, approximately, to the residual energy measured by the silicon detectors E_{resid}, by a quadratic relation $p \simeq \sqrt{2mE_{resid}}$, where m is the ion mass. Since the curvature ρ is related to the position at the focal plane X_{foc}, the relationship between the two measured quantities X_{foc} and E_{resid} is approximately quadratic with a factor depending on the factor m/q^2:

$$X_{foc}^2 \propto \frac{m}{q^2} E_{resid} \tag{4.3}$$

As a consequence, the trajectories of different isotopes of a given ion will be distributed on separated loci, according to the m/q^2 ratio, when an X_{foc} - E_{resid} plot is constructed. Theoretically, different groups should be visible corresponding to the different charge states and inside each group, the different isotopes should be clearly separated [132]. For the present data analysis, only the Ne^{10+} charge state is visible, because the ions are fully stripped at 270 MeV. Therefore, the clear separation between the different Neon isotopes is evident in Fig. 4.8, where the X_{foc} - E_{resid} matrix is shown for the data selected with the graphical condition on the ΔE_{CP}^{corr} - E_{resid} one (Fig. 4.7). It is therefore possible to sort out only $^{18}Ne^{10+}$, as required in order to study the events corresponding to the double charge-exchange process. The described identification procedure is then repeated for each silicon detector, using each time the AND condition between the Neon identification in the ΔE_{CP}^{corr} - E_{resid} plot and the $^{18}Ne^{10+}$ selection in the X_{foc} - E_{resid} plot. In this way, a unambiguous selection of all the detected ions of interest is obtained.

The same procedure was used also to identify the other ejectiles originated from each of the reactions studied in this work. In particular, using the the graphical condition on the Δ_{CP}^{corr} - E_{resid} (Fig. 4.7) and in the X_{foc} - E_{resid} (Fig. 4.8) it is possible to identify the $^{20}Ne^{10+}$.

An example of ^{18}F identification is shown in Fig.4.9 . Fig. 4.9a shows a ΔE-E bi-dimensional plot for a single silicon detectors together with a coarse graphical contour that includes the Fluorine ejectiles. Fig. 4.9b shows X_{foc} - E_{resid} scatter plot for a single silicon detector after selecting the F locus in the Δ_{CP}^{corr} - E_{resid}. A graphical contour selecting the ^{18}F is indicated. Finally an example of ^{16}O identification is shown in Fig. 4.10.

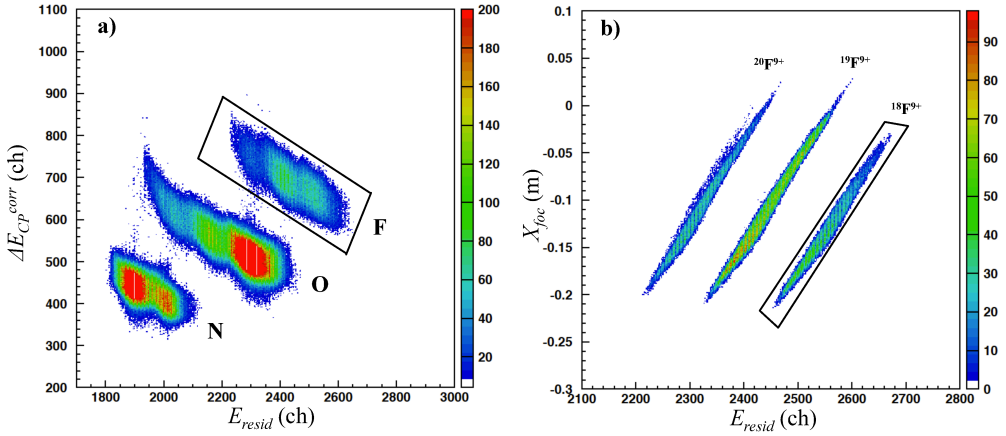

Figure 4.9: Example of identification of ^{18}F. a) Energy-loss Δ_{CP}^{corr} versus the residual energy E_{resid}. b) horizontal position at the focal plane X_{foc} vesus E_{resid}, after gating the data with the graphical condition drawn in panel a).

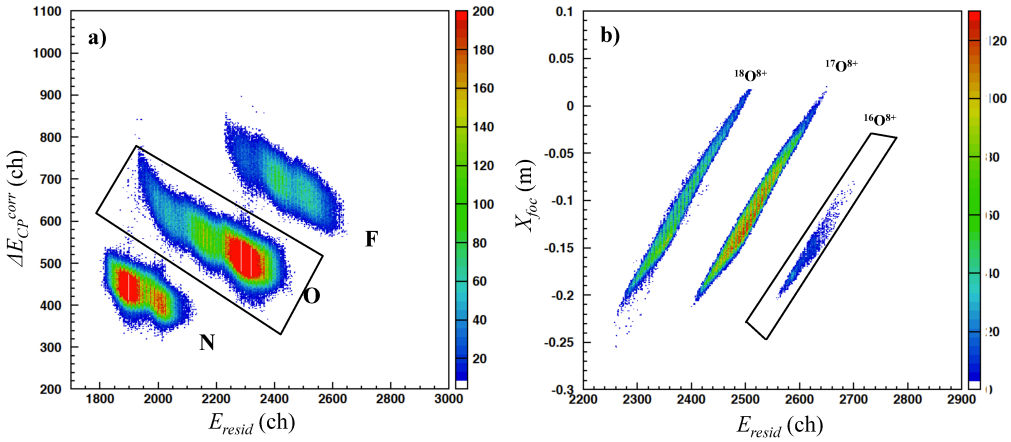

Figure 4.10: Example of identification of ^{16}O. a) Energy-loss Δ_{CP}^{corr} versus the residual energy E_{resid}. b) horizontal position at the focal plane X_{foc} vesus E_{resid}, after gating the data with the graphical condition drawn in panel a).

4.3 Final phase space parameters

Once the identification procedure was completed, the final phase space parameters (X_{foc}, θ_{foc}, Y_{foc} and ϕ_{foc}) were analysed in detail for the selected events. They provide information about the achieved horizontal and vertical focusing and about aberrations. A typical plot of the measured vertical position Y_{foc} versus the horizontal position X_{foc} show a "*butterfly*" shape [105]. This shape is characteristic of the final vertical phase space and it indicates that the vertical trajectories are focused only for a specific value of the ion momentum δ^* depending on the quadrupole and dipole field strength. This is expected in a QD spectrometer as MAGNEX, since the chromatic aberrations [101] avoid the focusing of ions with momentum deviation $\delta \neq \delta^*$. In the present case the plot, shown in Fig. 4.11, is characterized by a half-"*butterfly*" shape for $^{18}Ne^{10+}$ events, since the ejectiles corresponding to ^{40}Ar ground state own the δ^* momentum. The $X_{foc} = 0$ position in the abscissa corresponds to the spectrometer optical axis. Th horizontal lines seen in the plot are shadows produced by the silicon coated wires supporting the FPD Milar windows (Fig. 4.3).

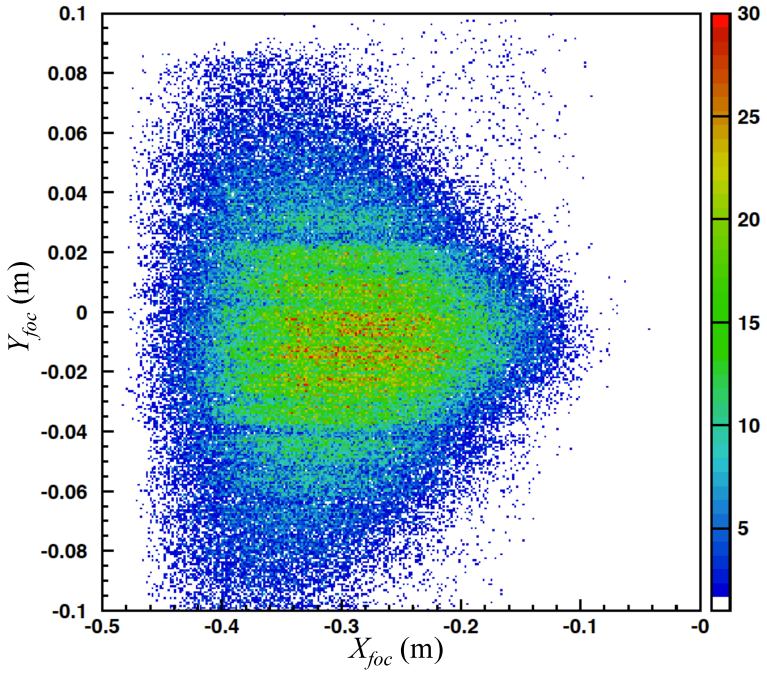

Figure 4.11: Bi-dimensional Y_{foc} *vs* X_{foc} scatter plot for the selected $^{18}Ne^{10+}$ ions from the $^{40}Ca(^{18}O,^{18}Ne)^{40}Ar$ reaction at 270 MeV.

A plot of the measured horizontal angle θ_{foc} versus the horizontal position X_{foc} is shown in Fig. 4.14, for the same events of Fig. 4.11. Since the FPD is inclined by 59.2° (1.033 rad) with respect to the plane perpendicular to the optical axis, the measured θ_{foc} are distributed around that angle in the plot. Some well correlated loci are present. They correspond to the states populated in the ^{40}Ca(^{18}O,^{18}Ne)^{40}Ar reaction. The deviation of the loci from the vertical lines is due both to the kinematical effect [103] and to second order aberrations. The curvature of the loci, especially visible near the borders, is due to the strong effect of the high order aberrations in the horizontal phase space.

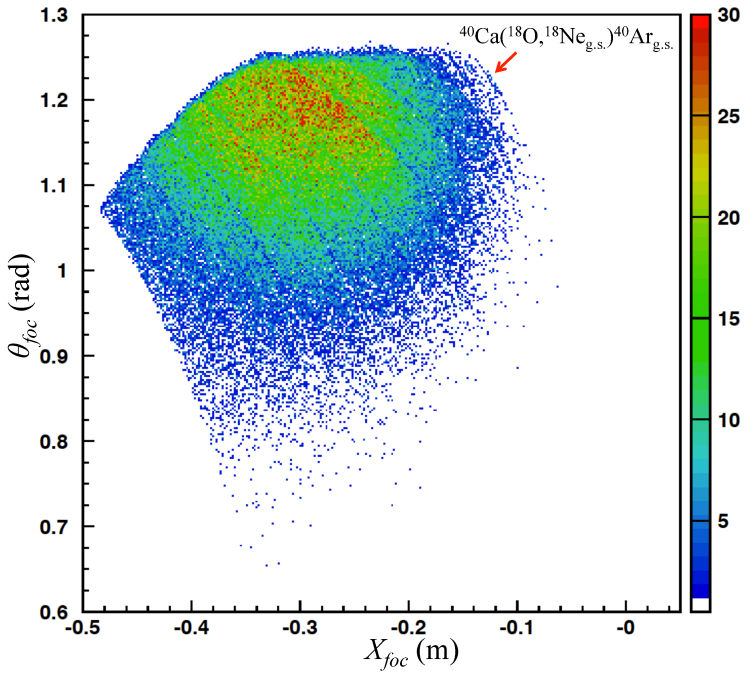

Figure 4.12: Bi-dimensional θ_{foc} *vs* X_{foc} scatter plot for the selected ^{18}Ne^{10+} ions from the ^{40}Ca(^{18}O,^{18}Ne)^{40}Ar reaction at 270 MeV.

4.4 Application of the ray-reconstruction technique

The ray-reconstruction procedure, described in Sections 3.3 is a fundamental step of the data reduction, since it allows to retrieve the ejectile momentum vector at the target and thus to reconstruct the reaction Q value and the scattering angle. The practical implementation of the method is organized in two sequential steps described in detail

in Sections 4.4.1 and 4.4.2.

4.4.1 The direct transport map

The first step of the reconstruction procedure is to built the transport map $\mathcal{M}$, necessary to describe the evolution of the phase space parameters from the target position to the focal plane. Using the COSY INFINITY program the transport map was calculated up to 10^{th} order. Once the direct transport map $\mathcal{M}$ is created, an accurate check is mandatory. Therefore a set of events corresponding to the ^{40}Ca(^{18}O,^{18}Ne)^{40}Ar reaction at 270 MeV were generated by Monte Carlo routines [128]. The ^{18}Ne ejectiles connected to the excitation of three ^{40}Ar states (g.s., 1.46 and 2.89 MeV) were tracked through the spectrometer by the application of the direct transport map. In the simulations, the beam energy needs to be properly corrected to take into account the target straggling effect on both the projectile and the ejectile, respectively, since the simulation program does not take into account energy losses.

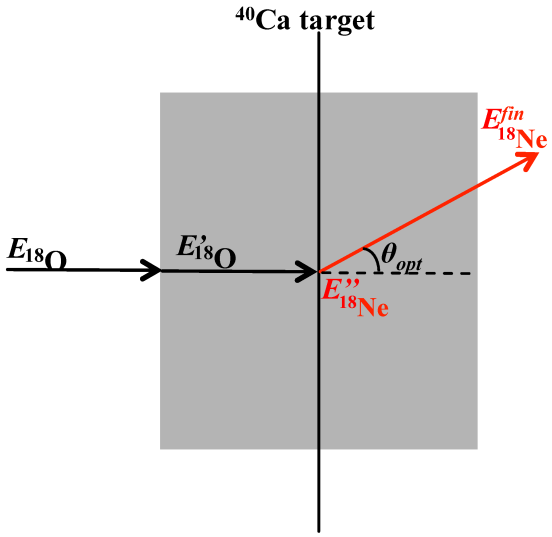

Figure 4.13: Effective beam energy calculation scheme.

Using the scheme drown in Fig. 4.13 and assuming that the reaction takes place in the middle of the target, the *effective* beam energy is evaluated by means of kinematic and energy loss calculation, as follows:

- the ^{18}O beam energy loss in the first half of the target is evaluated by the LISE++ program [133], giving the corrected energy $E'_{^{18}O}$;

- $E'_{^{18}O}$ is used as input of the program CATKIN [134], which calculates by relativistic kinematic transformations the energy $E''_{^{18}Ne}$ of the ejectiles produced in the ^{40}Ca(^{18}O,^{18}Ne)^{40}Ar reaction at the given angle $\theta_{opt} = 4°$;
- using again LISE++, the energy loss of the ^{18}Ne ejectiles in the remaining half target crossed with angle θ_{opt} is evaluated, obtaining $E^{fin}_{^{18}Ne}$.
- The final energy $E^{fin}_{^{18}Ne}$ is then taken as the reference one. Starting from this value and using CATKIN, the effective beam energy $E^{eff}_{^{18}O}$ is found. This is defined as the beam energy necessary to generate by the same process ^{18}Ne ejectiles emitted as $\theta_{opt} = 4°$ with energy $E^{fin}_{^{18}Ne}$, without any energy loss.

The effective energies obtained for each reaction discussed in this work are listed in Table4.1.

Table 4.1: Effective beams energy for the analyzed data.

output channel	θ^{opt}_{lab}	E_{beam} **(MeV)**	E^{eff}_{beam} **(MeV)**
^{18}Ne + ^{40}Ar	4°	270	269.35
^{20}Ne + ^{38}Ar	4°	270	269.35
^{18}F + ^{40}K	7°	270	269.40
^{16}O + ^{42}Ca	7°	270	269.45

As mentioned above, the quality of the result is checked comparing the simulated final phase space parameters with the experimental ones. The results of the performed simulation are shown in Fig. 4.14 and 4.15 for the dataset already shown in Section 4.3. Despite the highly non-linear aberrations, the simulated data (red points) give a rather faithful representation of the experimental ones (black points) both in the horizontal (θ_{foc} *vs* X_{foc} plot) and vertical (Y_{foc} *vs* X_{foc} plot) phase spaces. Moreover, a very accurate modelling of the dipole Effective Field Boundaries was necessary to obtain such result. The accuracy of the description of final space by the direct transport matrix is estimated about -0.5 ± 0.9 mm and 3 ± 5 mr in X_{foc} and θ_{foc}, respectively, similarly to what found in Ref.[112].

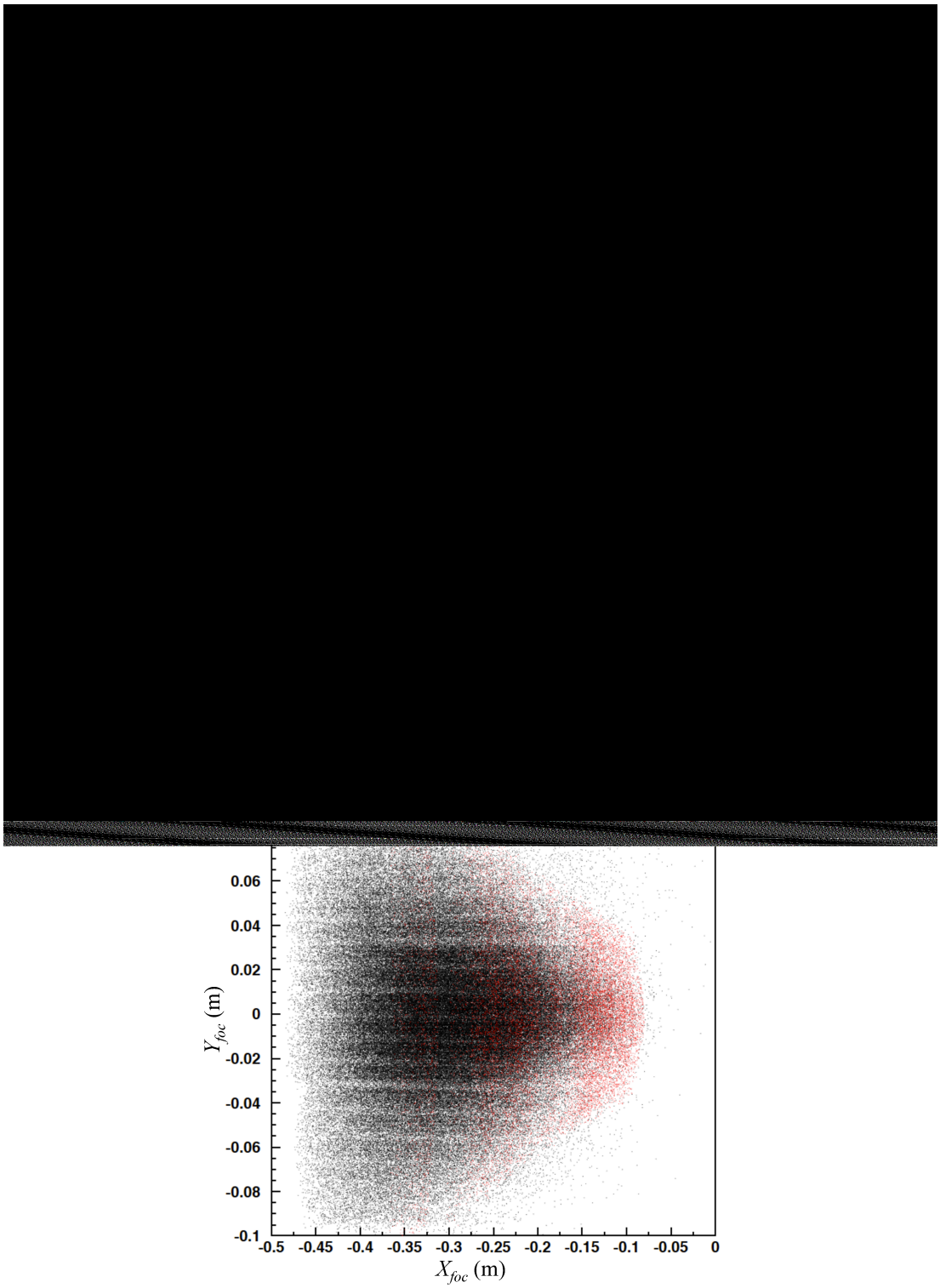

Figure 4.15: Y_{foc} *vs* X_{foc} comparison between the experimental data (black points) and the simulated ones (red points).

4.4.2 The inverse transport map and its application to the experimental data

The second step of the ray-reconstruction procedure consists in the inversion of the direct transport map by COSY INFINITY program and the use of $\mathcal{M}^{-1}$ for the calculation of the momentum vector at the target point. These are directly related to the physical quantities of interest, such as the modulus of the ejectile momentum and the scattering angle.

A plot of the reconstructed initial vertical angle ϕ_i versus the reconstructed initial horizontal one θ_i is shown in Fig.4.16. The reconstructed angular acceptance corresponds to the real one (-5.69° $< \phi_i <$ 5.69° and -5.16 ° + $\theta_{opt} < \theta_i <$ 6.3 ° + θ_{opt}).

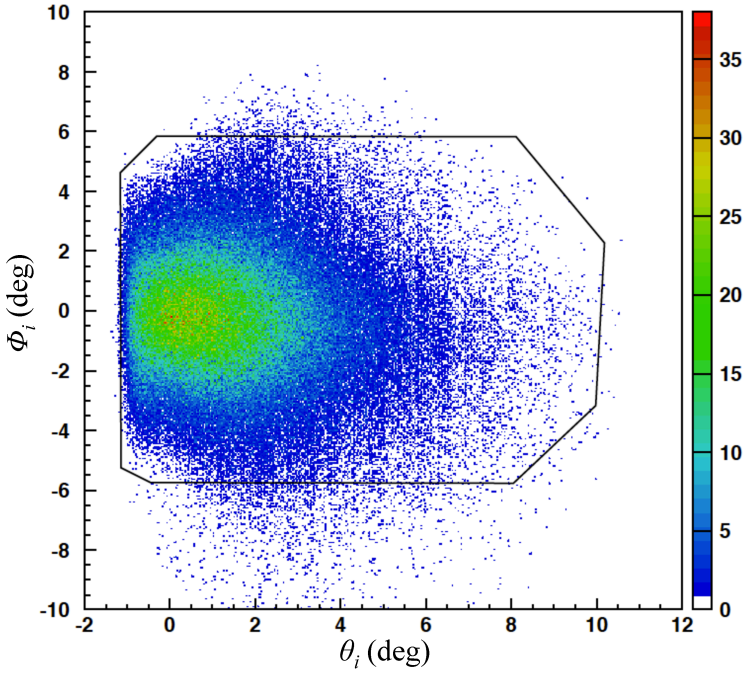

Figure 4.16: Reconstructed ϕ_i *vs* θ_i plot under the same experimental conditions of Fig. 4.11. The contour of the locus, drawn with the black line, represents the spectrometer solid angle acceptance.

The plot does not have the ideal rectangular shape. Such efficiency losses were studied in Ref.[135] and found to be due to a cut-off of the ejectile envelope by the spectrometer vacuum vessels. Nevertheless, this effect can be accurately taken into account in the cross section angular distribution extraction procedure. It will be described in details

in Section 4.6.

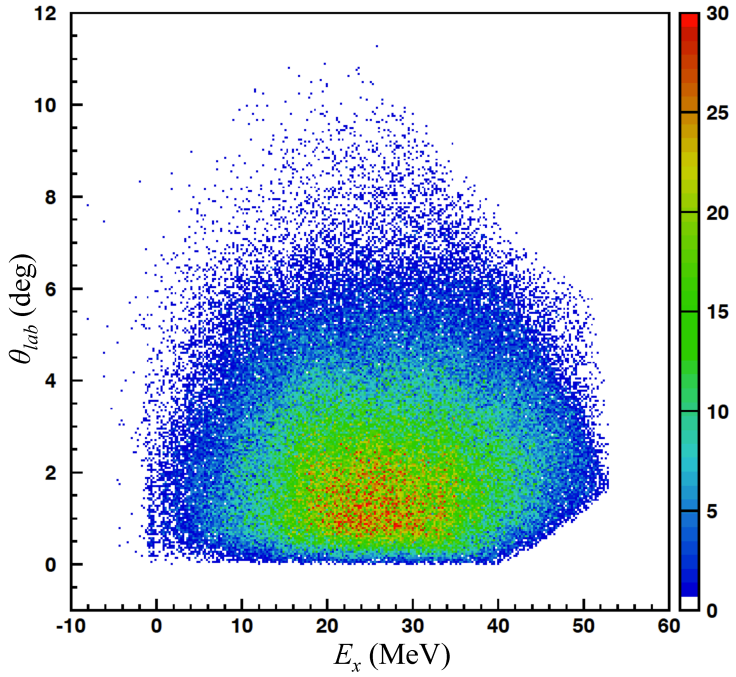

Figure 4.17: Reconstructed distribution of the events in the θ_{lab} *vs* E_x plane under the same experimental conditions of Fig.4.14.

The scattering angle in the laboratory frame θ_{lab} is extracted from the initial angles θ_i and ϕ_i through:

$$\theta_{lab} = \arccos \frac{\cos(\theta_{opt}) - \sin(\theta_{opt}) \tan(\theta_i)}{1 + \tan^2(\phi_i)} \tag{4.4}$$

Then, the initial kinetic energy of the ejectiles is deduced from the reconstructed relative momentum δ. The corresponding Q-values, or equivalently the excitation energy E_x are finally obtained by a missing mass calculation based on relativistic energy and momentum conservation laws, supposing a binary reaction:

$$E_x = Q_0 - Q = Q_0 - K\left(1 + \frac{M_e}{M_r}\right) + E_b\left(1 - \frac{M_p}{M_r}\right) + 2\frac{M_p M_e}{M_r} E_b K \cos(\theta_{lab}) \tag{4.5}$$

where M_e, M_r and M_p are the ejectile, residual and projectile masses, respectively, E_b represents the beam energy, K is the kinetic energy of the ejectile (related to the δ parameter) and Q_0 is the ground state to ground state Q-value (for the present

case Q_0 = -5.905 MeV). The two quantities θ_{lab} and E_x, are used to construct bi-dimensional plots in which the ground and excited states of the residual ^{40}Ar nucleus become evident, as shown in Fig. 4.17 for the data set of Fig. 4.14. The ^{40}Ar ground state and the several excited states are well visible as vertical and straight loci, as expected since E_x parameter does not depend on the scattering angle for transition to the ^{40}Ar states. The efficiency cut around 40 MeV excitation energy is due to the acceptance of the spectrometer [135].

4.5 Excitation energy spectra

The excitation energy spectra of ^{40}Ar nucleus are obtained from the E_x - θ_{lab} plots projecting the events on the E_x axis. A projection of the E_x spectrum in the angular region $0° < \theta_{lab} < 2°$ is shown in Fig. 4.18.

The described data reduction procedure was applied to the dataset corresponding to the other studied reaction. Examples of the obtained ^{40}K, ^{42}Ca and ^{38}Ar spectra are shown in Figs. 4.19, 4.20 and 4.21.

A Gaussian fit procedure, applied to the observed peaks, gives a mean energy resolution of about 500 keV (FWHM) in all the shown spectra. This resolution is affected by three main contributions. The first one is the spectrometer finite energy resolution, estimated in about 1/1000 [112], corresponding, in this case, to about 270 keV. The beam resolution, which is about 1/1000, is the second factor to take into account contributing, like in the previous case, for about 270 keV. The straggling effect induced by the target thickness accounts for about 300 keV, considering ^{18}O ions passing through the 279 μg/cm^2 ^{40}Ca target foil.

In the ^{40}Ca(^{18}O,^{18}Ne)^{40}Ar double charge exchange spectrum, shown in Fig. 4.18 ground state is clearly separated from the group of excited states of ^{40}Ar 2^+ at 1.460 MeV and ^{18}Ne 2^+ at 1.887 MeV. At higher excitation energy the measured yield is spread over many overlapping states.

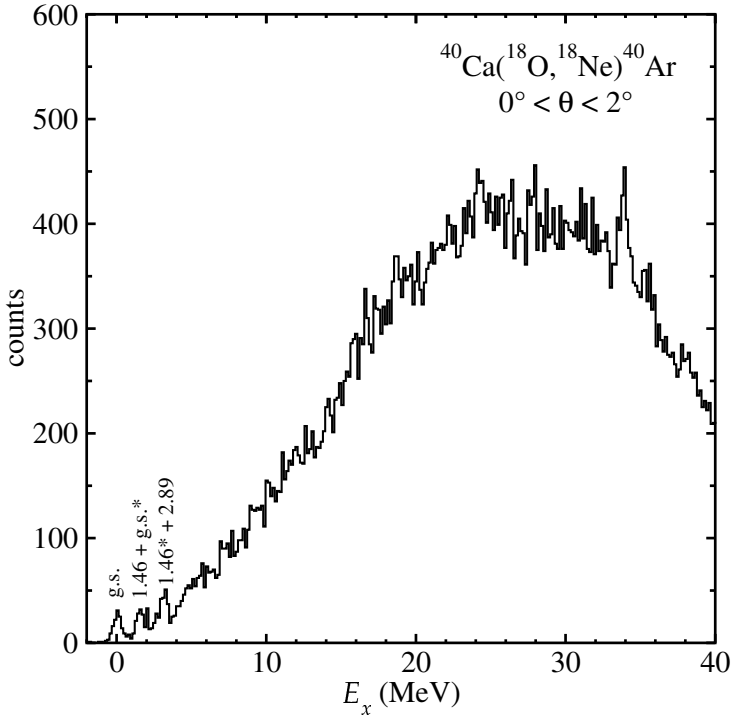

Figure 4.18: Excitation energy spectrum of the residual ^{40}Ar nucleus. The data are integrated in the angular range $0° \leq \theta_{lab} \leq 2°$. The asterisk indicates the first excited state of ^{18}Ne at 1.887 MeV.

As regards the ^{40}Ca(^{18}O,^{18}F)^{40}K single charge exchange spectrum (see Fig. 4.19) the strongest transition is to the 2^- state at 800 keV, even if higher multipolarities are visible (4^- g.s. and 3^- 30 keV state) [136]. The spectrum shows unresolved structure between 2 - 3 MeV. It is known that several states of ^{40}K are in this particular energy region [90, 136] which we cannot separate due to the experimental resolution. Therefore the group of 1^+ states at 2.27 and 2.73 MeV is also populated even if other high spin states could hide them. In particular, it is know from literature [136] the 2^-, 3^- states at 2.047 and 2.070 MeV, the 3^- state at 2.291 MeV and the 2^-, 4^- states at 2.397 and

2.419 MeV and higher spin transition at energy around 2.7 MeV can also contribute.

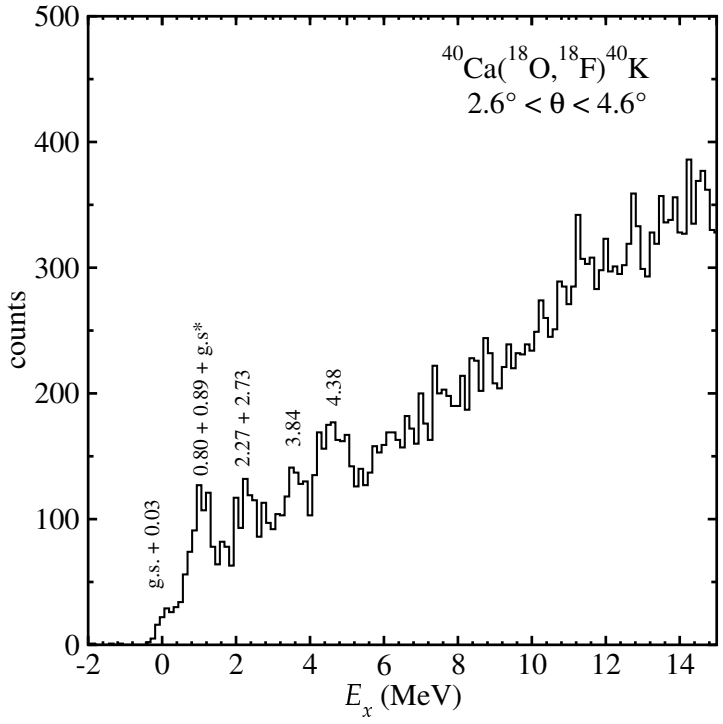

Figure 4.19: Excitation energy spectrum of the residual ^{40}K. The data are integrated in the angular range $2.6° \leq \theta_{lab} \leq 4.6°$. The asterisk indicates the first excited state of ^{20}Ne at 0.937 MeV.

In the ^{40}Ca(^{18}O,^{20}Ne)^{38}Ar two-proton transfer reaction, the ground state (0^+) is well separated from the excited states of both the ^{38}Ar (first excited state 2^+ at 2.167 MeV) and the ^{20}Ne ejectiles (first excited state 2^+ at 1.633 MeV). Furthermore, structures at 4.0, 6.5 and 9.2 MeV are clearly observed. Each peak is formed by many overlapping states of high spin known in literature [137, 138]. This result indicates the suppression of low multipolarity transitions due to L-matching conditions ($L_{opt} = 6$). The yield tends to increase with excitation energy as a consequence of the kinematical Q-matching conditions ($Q_{opt} = 32$ MeV).

The structures above $E_x \sim 12$ MeV, corresponding to the states of ^{14}C (g.s, 7.1, 8.33, 10.4 and 12.96 MeV) populated in the ^{16}O(^{18}O,^{20}Ne)^{14}C and to the states of ^{10}Be (g.s, 3.37 and 5.96 MeV) populated in the ^{12}C(^{18}O,^{20}Ne)^{10}Be. The ^{16}O and ^{12}C are contaminants present in the ^{40}Ca target.

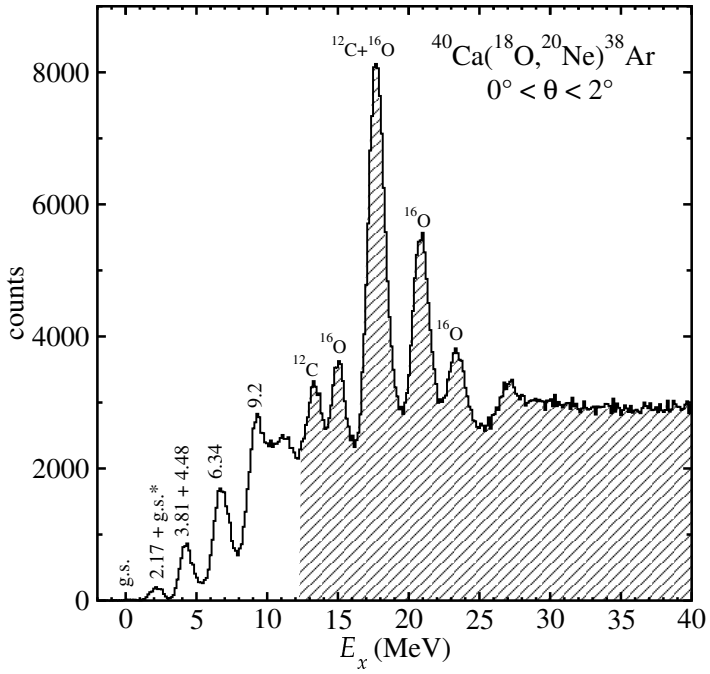

Figure 4.20: Excitation energy spectrum of the residual ^{38}Ar. The data are integrated in the angular range $0° \leq \theta_{lab} \leq 2°$. Peaks marked with an asterisk are associated to the excitation of ^{20}Ne at 2.15 MeV. Above $E_x \sim 12$ MeV structure coming from the reaction on ^{12}C and ^{16}O impurities are present in the ^{40}Ca target are labelled and indicated with hatched area.

Finally in the ^{42}Ca spectrum populated in ^{40}Ca(^{18}O,^{16}O)^{42}Ca (Fig. 4.21) the transition to the ground state and other low-lying states are strongly suppressed. The yield tends to increase with excitation energy due to the kinematical Q-matching conditions (Q_{opt} = 37 MeV). The structures visible at 15 MeV and 19 MeV correspond to the states populated via ^{12}C(^{18}O,^{16}O)^{14}C, on the carbon impurity in the target.

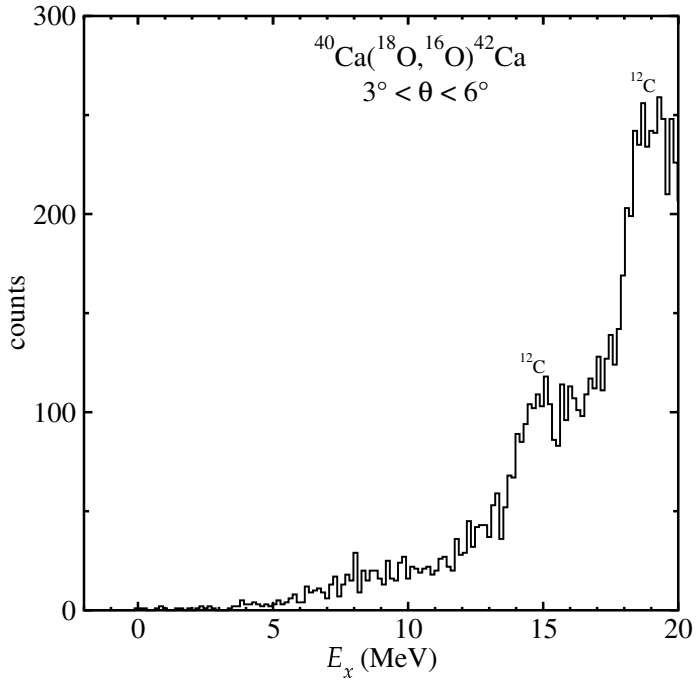

Figure 4.21: Excitation energy spectrum of the residual ^{42}Ca. The data are integrated in the angular range $3° \leq \theta_{lab} \leq 6°$.

4.6 Cross section angular distribution

The final step of the data reduction procedure is the extraction of the absolute cross section angular distributions.

The advantage of working with a large acceptance spectrometer is that, for a given set of measurements under identical experimental conditions, a wide range of scattering angles is covered. As a consequence, a consistent part of a cross section angular distribution can be measured in a single run in the same experimental conditions, resulting in a reduction of the uncertainty due to the normalization of runs at different angles. In particular, as already discussed, the large angular acceptance of the MAGNEX spectrometer gives the possibility to explore a θ_{opt} - $5° \leq \theta_{lab} \leq \theta_{opt} + 6°$ for a given central angle θ_{opt}. In the present data, this corresponds to an angular distribution which covers the range $0° \leq \theta_{lab} \leq 10°$ in the case of DCEX and two-proton transfer reaction, and the range $2° \leq \theta_{lab} \leq 13°$ for CEX and two-neutron transfer reactions.

In general, for a given nuclear transition, the differential cross section is defined as:

$$\frac{d\sigma}{d\Omega}(\theta) = \frac{N(\theta)}{N_{beam} N_{target} \Delta\Omega t_{live} \epsilon} \tag{4.6}$$

where $N(\theta)$ is the number of ejectiles detected at a given angle θ, N_{beam} is the number of incident ions, N_{target} is the number of scattering centers per unit surface, $\Delta\Omega$ is the solid angle covered by the detector, t_{live} is a factor which takes into account the acquisition dead time and ϵ is an overall detection efficiency factor. The number of incident ions is retrieved integrating the beam current measured by the Faraday cup. A digital integrator (see Chapter 3) gives the total charge Q collected in each run. At the considered energy, the ^{18}O ions are totally stripped after passing through the target [139], therefore the number of the beam ions is simply evaluated as $N_{beam} = Q/Ze$, where $Z = 8$ and $e = 1.602{\cdot}10^{-19}$C. Actually, a dedicated VME scaler measured directly the integrated charge Q_{live} corrected for the acquisition dead time, thus already including the factor t_{live} of eq. 4.6. The obtained N_{beam} values for each investigated reactions are listed in Table 4.2.

Table 4.2: Total number of collected ions N_{beam} for each investigated reaction.

^{18}O + ^{40}Ca	**N_{beam}(10^{13} ions)**
^{18}Ne + ^{40}Ar	200±10
^{20}Ne + ^{38}Ar	57± 3
^{18}F + ^{40}K	5.0 ± 0.3
^{16}O + ^{42}Ca	2.3 ± 0.1

The number of target nuclei for unit surface N_{target} is calculated from the known target density and thickness. The obtained value is $N_{target}^{^{40}Ca} = 4.2 \pm 0.1 \cdot 10^{18}$ atoms/cm^2.
As regards the evaluation of the solid angle $\Delta\Omega$, the geometry relevant for its determination is show in Fig. 4.22. In principle, the spectrometer solid angle acceptance is defined by 4 slits located 260 mm downstream the target and upstream the quadrupole entrance (green line in Fig. 4.22b). However, the overall efficiency losses in the spectrometer correspond to an effective reduction of the solid angle, as demonstrated in

Ref. [135]. The actual solid angle acceptance is deduced taking the contour of the reconstructed (θ_i, ϕ_i) locus in the laboratory frame, as shown in Fig. 4.16. The technique used to calculate the differential solid angle $\Delta\Omega$ is shown in Fig. 4.22b, where (θ_i, ϕ_i) contour for $\theta_{lab}^{opt} = 4°$ is drawn and the circular rings corresponding to laboratory angle bins of $\Delta\theta_{lab} = 0.3°$ are superimposed. The area defined by the interception between the circular ring enclosed in the (θ_{lab}, $\theta_{lab} + \Delta\theta_{lab}$) interval and ($\theta_i$,$\phi_i$) contour was calculated (full black area), thus obtaining the actual differential solid angle for each θ_{lab} bin, with an estimated error of about 2% for the central bins.

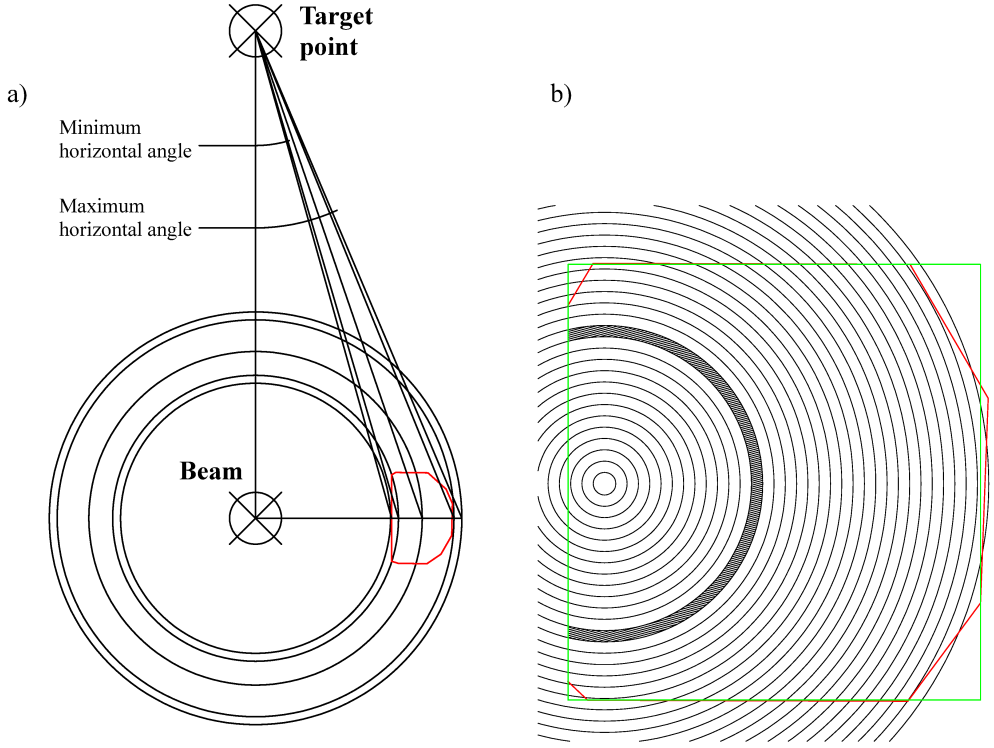

Figure 4.22: a) Geometry for the determination of the solid angle for a general θ_{opt}. b) Differential solid angle determination for $\theta_{opt} = 4°$. The effective spectrometer aperture, (determined by the same (θ_i, ϕ_i) contour of Fig. 4.16) and the spectrometer diaphragms aperture are indicated as the red and green line, respectively. The differential solid angle for a single angular bin is defined by the interception between the circular ring enclosed in the (θ_{lab}, $\theta_{lab} + \Delta\theta_{lab}$) interval and the ($\theta_i$, ϕ_i) contour (black hatched region).

The measured scattering angles in the laboratory frame were then transformed in the centre of mass one, multiplying by the Jacobian determinant of the transformation,

which depends on the angle and excitation energy. The overall efficiency factor ϵ is estimated taking into account the FPD detection efficiency (∼88%) and the efficiency in the ray reconstruction procedure (∼90%) . The latter is obtained from the ratio between the number of the events identified by the FPD and the number of the well reconstructed events. The number of detected ions $N(\theta)$ is extracted from the E_x - θ_{lab} spectra, after a proper selection of the events of interest. In the following three Sections the results for the ^{40}Ca(^{18}O, ^{18}Ne)^{40}Ar, ^{40}Ca(^{18}O, ^{20}Ne)^{38}Ar and ^{40}Ca(^{18}O, ^{18}F)^{40}K reactions will be presented.

4.6.1 ^{40}Ca(^{18}O, ^{18}Ne)^{40}Ar case

The transition to the ground state and first two excited states of ^{40} Ar were considered. The relative loci are quite well separated in the reconstructed E_x - θ_{lab} plot, shown in Fig. 4.23. In the same figure, the graphical cuts that selects the events of these transition are indicated.

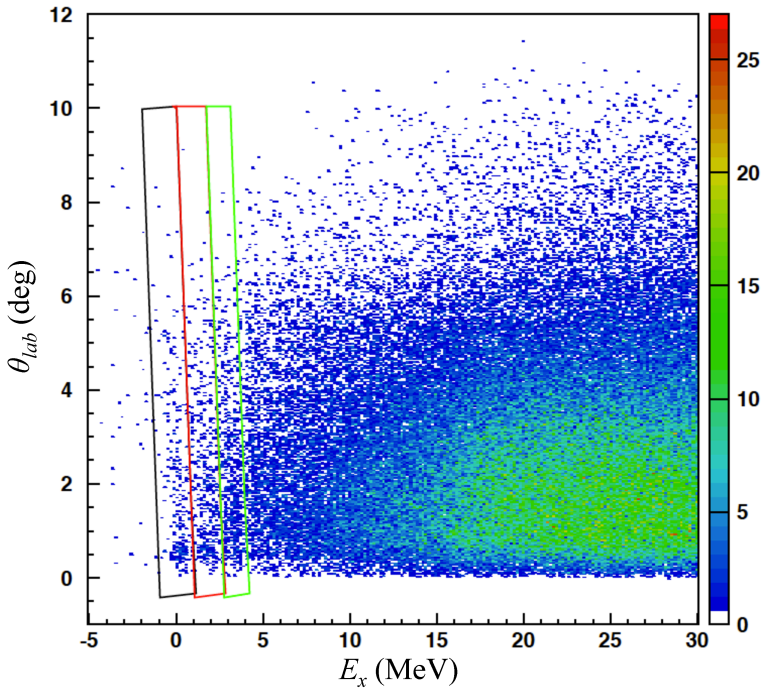

Figure 4.23: (E_x,θ_{lab}) plot. Graphical contours used to determine the angular distribution of the ^{40}Ar g.s (black line) 1.46 MeV (red line) and 2.89 MeV (green line) states.

The number of counts $N(\theta)$ for these transitions was determined using the graphical selections in the (E_x, θ_{lab}) plot (as shown in Fig. 4.23) and projecting on the θ_{lab} axis choosing an angular bin of $\Delta\theta_{lab} = 0.4°$. Once the $N(\theta)$ were extracted at each θ the angular distribution of the absolute cross sections were built following eq. 4.6. The resulting angular distributions are shown in Fig. 4.24.

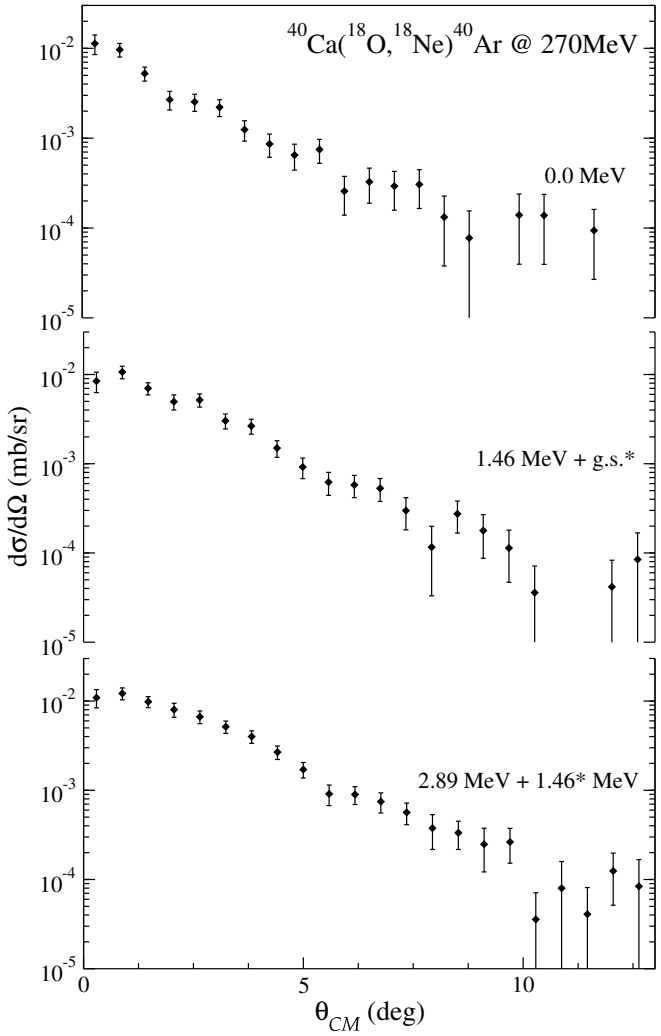

Figure 4.24: Angular distributions for transitions to the ^{40}Ar g.s., to the 1.46 MeV and 2.89 MeV excited states. The excited states are contaminated by the excitation of the ejectile.

In the angular distributions plots, the error bars are drawn for the vertical axis (see Section 4.6.4 for their evaluation), since the uncertainty on the angle determination is

quite small ($\sim 0.2°$).

4.6.2 The ^{40}Ca(^{18}O,^{20}Ne)^{38}Ar case

In the case of ^{40}Ca(^{18}O, ^{20}Ne)^{38}Ar reaction the transition to the ground state was studied. The procedure to extract the angular distribution is identical to that described above. The locus related to the ground state is separated from excited states of ^{38}Ar at 2.167 MeV and ^{20}Ne at 1.663 Mev in the E_x *vs* θ_{lab} plot , shown in Fig. 4.25. The projection of the selected events on the θ_{lab} axis gives $N(\theta)$ for each angular bin $\Delta\theta$. Then the angular distribution for the transition to the g.s. was constructed by eq. 4.6.

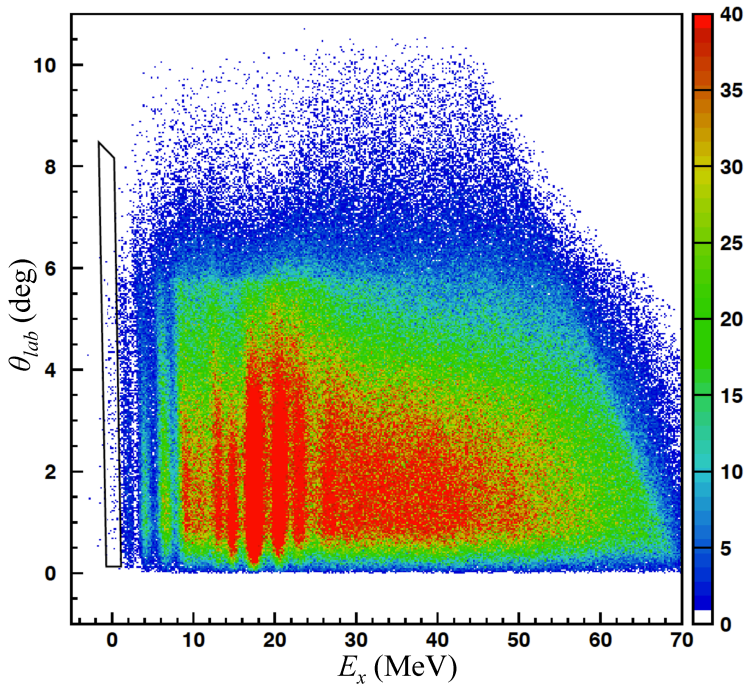

Figure 4.25: (E_x,θ_{lab}) plot. The graphical contour used to select the transition to ^{38}Ar g.s is indicated by the black line.

The result for the distribution is shown in Fig. 4.26.

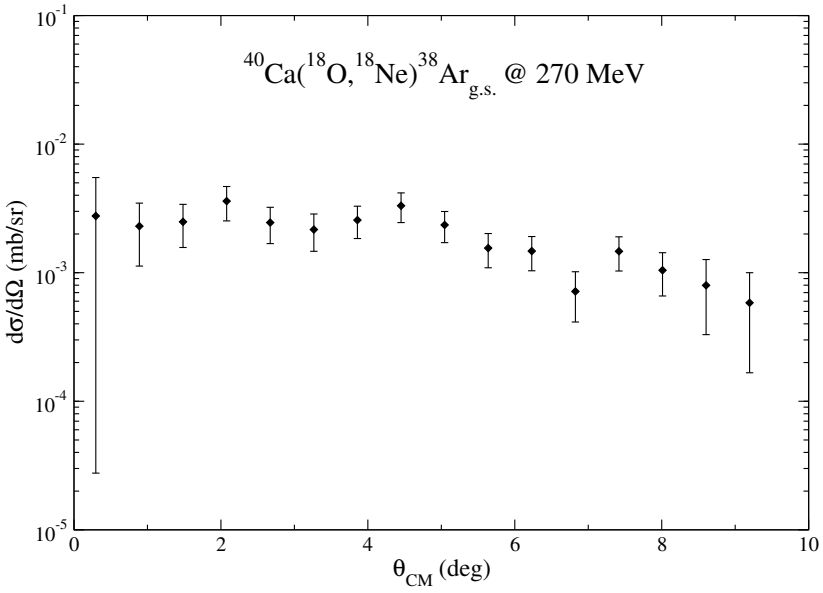

Figure 4.26: Angular distributions for transitions to the ^{38}Ar g.s.

4.6.3 The ^{40}Ca(^{18}O,^{18}K)^{40}K case

In the case of the ^{40}Ca(^{18}O, ^{20}Ne)^{38}Ar reaction the transition to the 1^+ states was studied. As discussed in Section 4.5, the group of 1^+ states at 2.27 and 2.73 MeV [136] could be hide by other high spin states. In order to do an approximate estimation of the cross section of them, a Gaussian fitting model was applied in the one-dimensional energy spectra in a energy region between 2-3 MeV. The routines of MINUIT [140] were used for this purpose. The results are shown in Fig. 4.27. The area of the obtained Gaussian function gives the number of counts for each angular bin ($\Delta\theta = 1°$). The angular distribution for the transition to the energy region of 2-3 MeV of ^{40}K is shown in Fig.4.28.

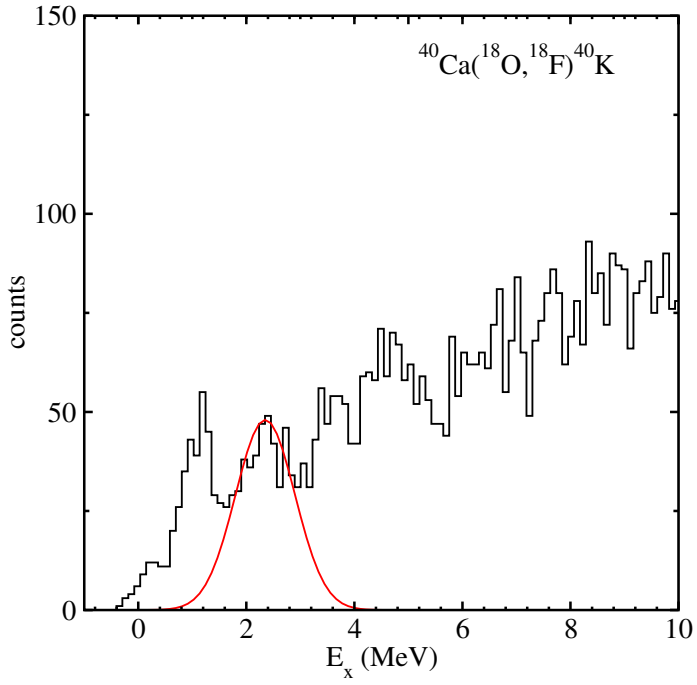

Figure 4.27: Excitation energy spectrum of the residual ^{40}K. The data are integrated in the angular range 2.6° $\leq \theta_{lab} \leq$3.6°. The fitted peak is shown within a red Gaussian function.

4.6.4 Cross section uncertainties

The cross section uncertainties were determined by applying the error propagation on eq.4.6, The uncertainties on the parameter N_{beam}, N_{target}, and ϵ are common to all the points of the angular distribution. They determine an overall uncertainty of about 10% in the absolute scale of the cross sections, which was not included in the error bars. The error on $\Delta\Omega$ depends on the uncertainties on the reconstructed vertical and horizontal angles ϕ_i and θ_i, respectively. The former is about $\Delta\phi_i = \pm$ 0.4° [112], and corresponds to a common factor for all the angular distribution bins. The latter is affected by an uncertainty of about $\Delta\theta_i = \pm$ 0.2° [112], and this influences more the bin corresponding to the border of the acceptance. The effect was evaluated considering the variation of the area (shown in Fig.4.22b) caused by variation of the θ_i within ±0.2°. The error on $N(\theta)$ is the statistical one $\Delta N(\theta) = \sqrt{N(\theta)}$, evaluated for each angular bin $\Delta\theta_{lab}$

chosen in the cross section extraction procedure.

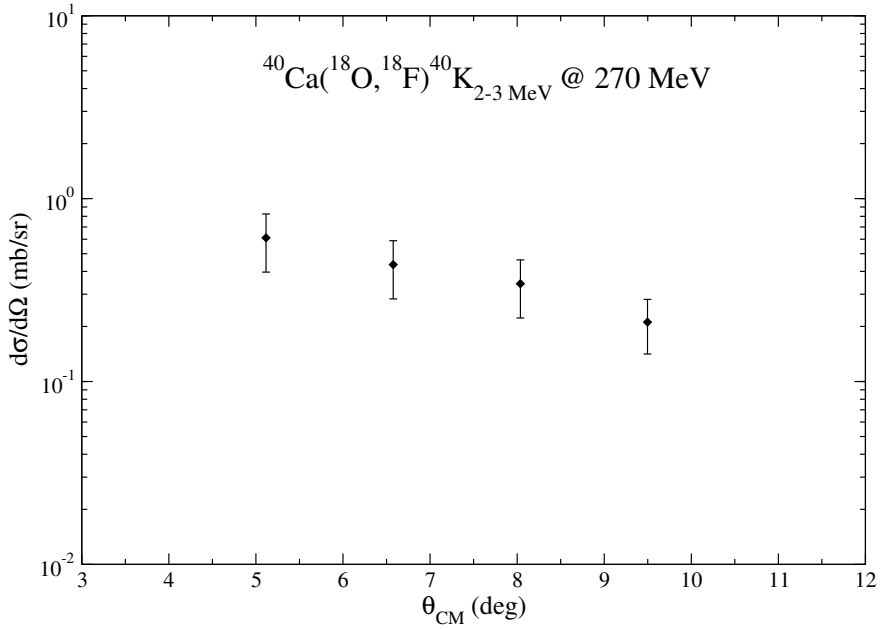

Figure 4.28: Angular distributions for ^{40}K transitions to 2-3 MeV energy region.

In the case of the angular distribution of ^{40}K the number of counts N were evaluated calculating the area (A) of the corresponding Gaussian function fit, given by:

$$A = 2\pi h\sigma \tag{4.7}$$

Considering that the error on the estimation of N is dominated by the error on the Gaussian height, since the σ parameter was fixed in each fit, and the statistical error is dominant, the error on N becomes:

$$\Delta N \approx 2\pi\sigma\Delta h \tag{4.8}$$

In summary, the cross section were extracted with typical uncertainties of about 15-25%, which is enough to learn about details of the reaction mechanism, as discussed in the following Chapters.

Chapter 5

Theoretical analysis of the ^{40}Ca(^{18}O,^{18}F)^{40}K reaction in the CEX-QRPA approach

In the present chapter, the theoretical analysis of the ^{40}Ca(^{18}O,^{18}F)^{40}K reaction is described and discussed in the fully quanto-mechanical framework of the Charge-Exchange Quasiparticle Random Phase Approximation (CEX-QRPA)[30–32] .

As already underlined in the previous Chapter, the ^{40}Ca(^{18}O,^{18}F)^{40}K reaction represents the intermediate channel for the ^{40}Ca(^{18}O,^{18}Ne)^{40}Ar DCE one. A consistent description of the intermediate reaction is the first step in order to develop a complete description of the more complex DCE reaction.

Moreover several results of the present CEX-QRPA analysis will be key ingredients for the simple model adopted to extract the DCE nuclear matrix element, as discussed in the next Chapter.

In the past, the CEX-QRPA approach was successfully used to describe the ^{11}Be, ^{15}C and ^{19}O nuclei studied via (^{7}Li, ^{7}Be) reactions [104, 141–143]. In the present case, this approach is applied to describe both the ^{18}F and ^{40}K nuclear structure. Then the nuclear structure calculation results are directly inserted into the Distorted Wave Born Approximation (DWBA) to calculate the cross sections. Consistency between structure and reaction mechanism calculations is achieved through the use of the same effective nucleon-nucleon (N-N) interaction in every step of the calculations. In fact, following the semi-phenomenological approach of refs. [144, 145], both the static mean

and pairing fields derive from the residual interaction of Hofmann and Lenske [145], which is also used in the QRPA and DWBA calculations. The Chapter is organized as follows: Sections 5.1 and 5.2 are devoted to the description of the QRPA formalism and give the details of the structure calculations, needed for the determination of the response functions based on the RPA-Greens function method [144]. The residual NN-interaction [145] is described in Section.5.3. The results of the QRPA calculations are shown in Sect. 5.4. The DWBA calculations are described in Section5.6 and their results are given in Section5.7.

5.1 The Quasi-particle Random Phase approximation

Basic mean filed models of the nuclear many-body problem, such as the shell or Hartree-Fock (HF) ones, describe the low-lying excited states of nuclei as combinations of independent single particle excitation in a mean field.

The Random Phase Approximation (RPA) theory [30], introducing correlations between particles and holes, represents the next step with respect to the mean field approach. In this model, a more careful description of the nuclear states is achieved in term of correlated 1p-1h excitations, a description which also should be valid for states at higher excitation energy and for nuclei that are not spherically symmetric.

The main finding is that a strong attractive residual interaction between particle-hole pairs reduces the energy of a highly correlated state, while a repulsive interaction has the opposite effect. This energy shift constitutes the real part of a complex quantity, called self-energy, and depends on the strength of the residual interaction and correlations. The imaginary part of the self-energy accounts for the possible broadening of the state due to the energy shift, since the decay width may change. This model practically includes weak perturbations of the mean field in the continuum.

The Quasiparticle Random Phase Approximation (QRPA) allows a treatment of the weakly bound systems in a equivalent way compared to RPA, using the quasiparticle formalism that is connected to the particle-hole formalism by the Bogoliubov-Valantin transformations. The QRPA providing that an appropriate residual interaction is used, allows to take into account the pairing correlations.

In the present case, the QRPA model is used to describe charge-exchange processes in which a quasi-proton is transformed in a quasi-neutron. As a consequence, the

CEX-QRPA operator describes the creation and annihilation of the quasi-proton and quasi-neutron, through an isovector residual interaction.

5.2 The CEX-QRPA formalism

The basic elements needed to define a RPA problem are the ground state system (GS), characterized by a N_0 neutron and Z_0 proton (or vacuum state):

$$|0\rangle = |N_0, Z_0; \mathrm{GS}\rangle \tag{5.1}$$

and the residual interaction. In RPA model the Hilbert space of the excited states is truncated to include only 1p-1h excitations on the (correlated) ground state. The general Hamiltonian for a nucleus is:

$$H = T + V = T + U + (V - U) = H_0 + V_{res} \tag{5.2}$$

where T represents the kinetic energy and V the NN-interaction. A static mean field potential U is introduced in order to separate H in two parts: the residual particle-hole interaction $V_{res} = (V - U)$ and the mean field Hamiltonian H_0.
Starting from the single particle creation and annihilation operators for fermions $a^+_{jm}(p,n)$ and $\tilde{a}_{jm}(p,n) = (-1)^{j+m} a_{j-m}(p,n)$, the one-quasiparticle (1-QP) annihilation α_{jm} and creation α^+_{jm} operators are obtained through the linear Bogoliubov-Valatin transformation:

$$\begin{aligned} \alpha_{jm} &= u_j a_{jm} - (-1)^{j+m} v_j a^+_{j-m} \\ \alpha^+_{jm} &= u_j a^+_{jm} - (-1)^{j+m} v_j a_{j-m} \end{aligned} \tag{5.3}$$

where u_j and v_j are the emptiness and occupation amplitudes, respectively, for the orbital with total angular momentum j, with $u_j^2 + v_j^2 = 1$. It is important stressing that α_{jm} and α^+_{jm} operators obey to standard commutation relations for fermion.
The two-quasiparticle (2-QP) creation operators are then constructed in the second quantisation formalism in terms of the 1-QP α_{jm} and α^+_{jm} operators:

$$Q^+_{JM}(j_n, j_p) = \sum_{m_n, m_p} \langle j_n m_n j_p m_p | JM \rangle \, \alpha^+_{j_n m_n} \alpha^+_{j_p m_p} \tag{5.4}$$

A similar formula gives the 2-QP destruction operators Q_{JM}. In eq. 5.4 the α^+_{jm} operators describe the creation of a quasi-neutron and a quasi-proton with angular

momentum j_n and j_p and magnetic quantum number m_n and m_p respectively. Since the Q_{JM} and Q^+_{JM} operators describe charge exchange transitions in which a proton is transformed into a neutron or vice versa, they depend on the Clebsch-Gordan coefficients giving the angular momentum coupling, which have to satisfy the conditions $j_p + j_n = J$ and $m_p + m_n = M$.

The complete operator for the CEX excitations ω^+_{JM} is finally obtained in the QRPA formalism considering the superposition Q^+_{JM} operator and its time reversal:

$$\omega^+_{JM} \equiv \sum_{j_n j_p} \left[X^J_{j_n j_p} Q^+_{JM}(j_n, j_p) - Y^J_{j_n j_p} (-1)^{J-M} Q_{J-M}(j_n j_p) \right] \tag{5.5}$$

In an analogous way the destruction CEX operator ω_{JM} is defined. The quantities X^J and Y^J represent the QRPA amplitudes for the direct and time reversed exchange of such quasiparticles. These amplitudes are simply related to the emptiness u_j and occupation v_j ones and will be deduced from them, i.e., from the state-dependent pairing field of Section5.4.2.

In the quasiparticle representation there is isospin mixing: the τ^+ and τ^- type excitation (where τ indicates the isospin operator) are mixed as much as the softness of the Fermi surface increases. However, projecting on the τ^+ subspace, it is always possible to separate the two contributions in the matrix elements. The action of the CEX operator ω^+_{JM} on the vacuum state of eq.5.1 leads to:

$$\begin{aligned} \omega^+_{JM} |0\rangle &= |JM; N_0 \pm 1, Z_0 \mp 1\rangle \\ \omega^+_{JM} |0\rangle &= 0 \end{aligned} \tag{5.6}$$

The CEX operator ω^+_{JM} takes into account only the 2-QP excitations. However, also higher order configurations (4-QP and so on) contribute to the eingestates of the populated nucleus. Separating all these contributions from the 2-QP component and assembling them in the operator η^+_{JM} (orthogonal to ω^+_{JM}), the state operator which generates the true eingestates can be written as:

$$\Omega^+_{JM}(\alpha) = \sum_a z^J_a(E_\alpha) \omega^+_{JM}(a) + \eta^+_{JM}(a) \tag{5.7}$$

where the summation represents the mixing of the 2-QP configurations. The spectroscopic amplitudes $z^J_a(E_\alpha)$ determine the probability to find the model states $\omega^+_{JM}(a)|0\rangle$ with eigenvalue E_a distributed over the eigenstates $\Omega^+_{JM}(a)|0\rangle$ which in general have excitation energy $E_\alpha \neq E_a$.

5.2.1 The RPA Greens function method

The QRPA equations may be found in a similar way as in the RPA theory [30]. But, the conventional RPA approach, becomes impracticable for huge configuration spaces. When it is not required to determine with high precision features of individual states, a method that allows calculating reliably the energy averaged response functions is the RPA-Green's function method [146].

5.2.1.1 The nuclear response function

A practical definition of response of a nucleus is essentially the measured differential cross section for inelastic scattering normalized by the free scattering one [144]. Assuming that all the effects not directly related to the intrinsic nuclear structure are negligible or have been removed from measured cross section $\sigma^{PT} = F\sigma^{PN}$, where σ^{PT} is the differential cross section for the reaction between projectile P and the target T, while σ^{PN} for the corresponding processes in free projectile-nucleon (PN) scattering, therefore the quantity F is closely related to the nuclear response. Since F effectively represents a sum over nuclear response in different spin-isospin channels (weighted depending on the probe), it has no meaning until the operator is specified. The nuclear response depends only on nuclear structure and, once the particular channel is specified also, it is probe independent. This means that the nuclear response in a specific channel $(S,T) \equiv \alpha$ should be the same for different probes.
In general, the probe is defined by a function $P_\alpha(\alpha : 1, \sigma, \sigma\tau....)$ [144], characterized by a precise structure (S,T), which contains the effects of the NN-interaction and distorted wave potential. For the CEX reaction, the probe function contains only isovector operators: $\alpha = \tau, \sigma\tau, ...$
The basic hypothesis of the following discussions is that the cross section can be written as:

$$\sigma(\omega, q) = \sum_{\alpha} |T_\alpha(\omega, \mathbf{q})|^2 \, R_\alpha(\omega, \mathbf{q}) \tag{5.8}$$

where ω and q indicate the transferred energy and momentum, respectively. eq. 5.8 means that it is possible to separate the structure part from the dynamics one, which are represented respectively by the response function $R_\alpha(\omega, \mathbf{q})$ and free scattering T-matrix. The total value of the integral of the response function $R_\alpha(\omega)$ is determined

by the sum rules, depending on the specific operator P:

$$S_n(P_n) = \int d\omega \omega^n R_\alpha(\omega, P_\alpha) \tag{5.9}$$

where n =0,1 represent the Non-Energy (NEWS) and Energy Weighted Sum (EWS), respectively. These are of great practical importance since are independent on the model used for R_α. In particular, the difference of the NEWS for $\beta^\pm$ transitions lead to the well known Ikeda sum rules [88], which relate the response of a nucleus to ground state properties.

The RPA nuclear response function to an incoming probe P_α is precisely defined in terms of the transition matrix elements between the vacuum state $|0\rangle$ and the excited state $|N\rangle$ of energy ω_N, for a transition induced by an external field P_α:

$$R^{RPA}(\omega, \mathbf{q}) \equiv \sum_{N\neq 0} |\langle N|P_\alpha|0\rangle|^2 \delta(\omega - \omega_N) \tag{5.10}$$

5.2.1.2 The RPA-Green's function method: the Dyson equation

Introducing the many-body Green function $G_{RPA}(\omega)$ of the Hamiltonian of eq.5.2:

$$G_{RPA}(\omega) = (H_A - \omega - i\eta)^{-1} + (H_A + \omega - i\eta)^{-1} \tag{5.11}$$

ther RPA nuclear response function of eq.5.10 may be rewritten as a ground state expectation value:

$$R^{RPA}_\alpha(\omega, \mathbf{q}) = \frac{1}{\pi} Im \langle 0|P^+_\alpha G_{RPA}(\omega) P_\alpha|0\rangle \tag{5.12}$$

Inserting a complete set of eigenstates $|N\rangle$:

$$R^{RPA}_\alpha(\omega, q) \frac{1}{\pi} Im \sum_{N=0} |\langle N|P_\alpha|0\rangle|^2 \cdot \left[(\omega_N - \omega - i\eta)^{-1} + (\omega_N + \omega - i\eta)^{-1}\right] \tag{5.13}$$

A convenient way to determine $R(\omega, q)$ in RPA is to solve the coupled Dyson equation for G:

$$G_{RPA} = G_0 + G_0 V_{res} G_{RPA} \tag{5.14}$$

where:

$$G_0(\omega) = (H_0 - \omega - i\eta)^{-1} + (H_0 + \omega - i\eta)^{-1} \tag{5.15}$$

It represents the Green function for the independent particle model, which describes the uncorrelated 2-QP excitations. The solution of the Dyson equation is based on the

knowledge of the G_0 propagator and the particle-hole interaction V_{res}, for which the interaction of Ref.[145], described in Section (5.3), is used.
In coordinate space, the Dyson equation (eq.5.14) becomes an integral equation:

$$G^{(\alpha)}_{RPA}(\mathbf{r},\mathbf{r}'\omega) = G^{(\alpha)}_0(\mathbf{r},\mathbf{r}'\omega) + \int d\mathbf{r}_1 \int d\mathbf{r}_2 G^{(\alpha)}_0(\mathbf{r},\mathbf{r}_1,\omega) V^{(\alpha)}_{res}(\mathbf{r}_1,\mathbf{r}_2) G^{(\alpha)}_0(\mathbf{r}_2,\mathbf{r}',\omega) \tag{5.16}$$

In this representation the response function is written as:

$$R^{RPA}_{\alpha}(\omega,\mathbf{q}) = \frac{1}{\pi} Im \int d(\mathbf{r}') \int d(\mathbf{r}) P(\mathbf{r}) G^{(\alpha)}{}_{RPA}(\mathbf{r},\mathbf{r}'\omega) P^*(\mathbf{r}') \tag{5.17}$$

Finally, the transition densities which will be used in DWBA calculations obtained is:

$$\rho^{(\alpha)}(\mathbf{r},\omega) = \frac{1}{\pi} \frac{\int_0^\infty d\mathbf{r}'(\mathbf{r},\mathbf{r}'\omega) M^*_\alpha((\mathbf{r}')}{\sqrt{d\omega R^{RPA}_\alpha(\omega)}} \tag{5.18}$$

where M_α denotes an auxiliary external field, used only for a computational necessity and chosen such that it accounts for the essential (S,T) properties of the probe function P_α. Indeed, since also $R^{RPA}_\alpha(\omega)$ in the denominator of eq.5.18 is calculated using the same field, the dependence of the transition densities on M_α is negligible.
Of practical interest are solutions of eq.5.17 for multipole operators of Fermi-type, $P_\alpha \sim P^{\pm}_{LM} = \tau_\pm r^L Y_{LM}$, and the Gamow-Teller type $P_\alpha \sim P^{\pm}_{JM} = \tau_\pm r^L [Y_L \otimes \sigma]_{JM}$, where $J = L$, $L \pm 1$ and $\tau_\pm$ are the isospin operators. The (reduced) matrix elements of these operators determine the β-decay properties of nuclear state.

5.3 The residual interaction

A realistic NN-interaction, including the tensor contribution, is used in both structure and dynamics calculations, as well as in the determination of the mean and pairing fields. It is the isovector part of the D3Y G-matrix interaction of Hofman and Lenske [145], which consists of direct and exchange terms with central (scalar and vector), rank-2 tensor and spin-orbit components. The latter has a small effect only, thus was neglected in the calculations. This interaction, depend on the nuclear density and the charge asymmetry is found to be well suited for light neutron-rich nuclei such as ^{11}Li and ^{19}C [147, 148], ^{11}Be [141, 142], ^{15}C and ^{19}O [104, 143].
A proper treatment of the medium effect is essential for a fully microscopic description of finite-nuclei. A well proved approach to derive in-medium NN-interactions starting

from the NN-interaction in free space is the Brueckner theory [149]. The Brueckner G-matrix for infinite nuclear matter is then applied in the Local Density Approximation (LDA) to finite nuclei [149]. However, in this way the empirical saturation properties of the nuclear matter are generally missed, at least when only 2-body correlations are included.

The solutions of the Dirac-Brueckner (DB) integral equations for asymmetric matter are parametrized in terms of appropriate meson-nucleon coupling constants acting at each vertex of the in-medium NN-interaction [147]. For finite nuclei, a phenomenological density dependence is supplemented to avoid the collapse of the nuclear matter at high densities [145]. Density dependent vertex functions are introduced as follows:

$$f_\gamma(\rho) = s(1 + \sum_{n=1}^{N_\gamma} a_n^\gamma z^{n\beta}) \tag{5.19}$$

where $z = \rho/\rho_0$, the base exponent $\beta = 1/3$ and $\gamma = (0\ ,\ \tau)$ indicates isoscalar and isovector vertex functions, respectively. The scaling factors s_γ and the coefficients a_n^γ are fitted to the saturation properties of infinite symmetric nuclear matter. These allow a first (N_τ=1) and a third (N_0=3) order approximation for f_τ and f_0, respectively. The vertices $f_\gamma(\rho)$ are used to calibrate the strength of the effective potential obtained from the DB coupling constants, leaving the intrinsic momentum structure unchanged. The latter is defined by a parametrization of the M3Y G-matrix with three Yukawa functions. Their ranges are chosen to represent the long-range tail (1.414 fm) if the One Pion Exchange Potential (OPEP) and medium and short-range parts, which corresponds to σ (0.40 fm) and ω,ρ,δ (0.25 fm) meson exchange, respectively. The meson δ appears to be important in nuclear asymmetric matter because it introduces an increased isovector strength at low density [147].

In the approach of Ref.[145], the total HF energy of a nucleus A is given by:

$$E = T + \frac{1}{2}\left\langle \overline{V} \right\rangle \tag{5.20}$$

with kinetic energy:

$$T = \sum_{k<A} \left\langle k \left| \frac{p^2}{2m} \right| k \right\rangle = \int d\mathbf{r} \frac{\hbar^2}{2m} [t_p(\mathbf{r}) + t_n(\mathbf{r})] \tag{5.21}$$

and potential energy of a two-body interaction V:

$$\left\langle \overline{V} \right\rangle = \left[\sum_{k_1,k_2} \langle k_1 k_2 | V | k_1 k_2 \rangle - \langle k_2 k_1 | V | k_2 k_1 \rangle \right] \tag{5.22}$$

where $|k\rangle$ represents single particle states and $t_q(\mathbf{r})$ is the kinetic energy density (where $q = p, n$ denotes protons and neutrons). V is expressed in terms of interactions for like ($q = q'$) and unlike ($q \neq q'$) particles, with direct and exchange contributions shown separately:

$$\begin{aligned}\langle \overline{V} \rangle = \langle V^d \rangle + \langle V^e \rangle = \sum_{qq'} \int d\mathbf{r_1} \int d\mathbf{r_2} \, \{\rho_q(\mathbf{r_1}) \\ \rho_{q'}(\mathbf{r_2}) V^d_{qq'}(\mathbf{r_{12}}) + \rho_q(\mathbf{r_1}, \mathbf{r_2}) \rho_{q'}(\mathbf{r_1}, \mathbf{r_2}) V^e_{qq'}(\mathbf{r_1}, \mathbf{r_2})\}\end{aligned} \tag{5.23}$$

Here $\mathbf{r}_{1,2}$=$\mathbf{r}_1 - \mathbf{r}_2$ is the relative coordinate and the density matrices are defined in terms of the single particle wave functions Φ_k:

$$\rho_q(\mathbf{r_1}, \mathbf{r_2}) = \sum_{k\sigma} \Phi^*(\mathbf{r_1}, \sigma, q) \Phi_k(\mathbf{r_2}, \sigma, q) \tag{5.24}$$

Due to the Pauli principle, the exchange term is non local. Its exact treatment in the HF functional leads to a coupled system of integro-differential equations. A convenient approach, especially for large charge asymmetry and variable density, is the Density Matrix Expansion (DME), invented by Negele and Vautherin [150]. This method provide a systematic expansion of the non local exchange parts of any given finite range effective N-N interaction. The basic features of interaction are retained, but results will depend on the expansion order. After a coordinate transformation into the center of mass reference system, the density matrix is expanded in Taylor series in terms of the one-body local density, where the first two terms are:

$$\rho\left(\mathbf{r} + \frac{s}{2}, \mathbf{r} - \frac{s}{2}\right) = \rho_{SL}(sq_F)\rho(\mathbf{r}) + \frac{35}{2sq_F^3} j_3(sq_F) \left[\frac{1}{4}\nabla^2\rho(\mathbf{r}) - t(\mathbf{r}) + \frac{3}{5}q_F^2\rho(\mathbf{r})\right] + ... \tag{5.25}$$

Here ρ_{SL} is the Slater density, q_F the average relative momentum between the two interacting particles, j_n the spherical Bessel of order n, $\mathbf{r}$ and $\mathbf{s}$ are the centre of mass and relative coordinates, respectively. The separation variable is achieved with this method. An even simpler formulation can be obtained [145] by defining an effective Fermi momentum:

$$q_F^2(\mathbf{r}) = \frac{5}{3}\frac{t(\mathbf{r}) - 1/4\nabla^2\rho(\mathbf{r})}{\rho\mathbf{r}} \tag{5.26}$$

With this choice, the DME eq. 5.25 reduces to the Slater approximation:

$$\rho(\mathbf{r} + \frac{\mathbf{s}}{2}, \mathbf{r} - \frac{\mathbf{s}}{2}) = \rho_{SL}(sq_F)\rho(\mathbf{r}) \tag{5.27}$$

but with a modified Fermi momentum which accounts for surface corrections. Separating the **r** and **s** coordinates and integrating on **s**, the exchange part becomes:

$$\langle V^e \rangle = \sum_{qq'} \int d\mathbf{r} \rho_q(\mathbf{r}) \rho_{q'}(\mathbf{r}) \tilde{V}^e_{qq'}(\mathbf{r}) \tag{5.28}$$

where $\tilde{V}^e_{qq'}(q_{Fq}, q_{Fq'}; \mathbf{r})$ is the interaction strength.
Once the pairing interaction (calculated as in Section 5.4.2) is introduced, to which the DME method can be equally well applied, the obtained G-matrix interaction is renormalized by the in-medium vertex functions of eq.5.19. Thus, the density dependent in-medium interaction is given by:

$$V^*_\gamma(\mathbf{r_1}, \mathbf{r_2}; \rho) = g_\gamma(\mathbf{r_1}) V^d_\gamma(\mathbf{r_1} - \mathbf{r_2}) g_\gamma(\mathbf{r_2}) \tag{5.29}$$

$$V^*_\gamma(s, \mathbf{r_2}; \rho) = g^2_\gamma(\mathbf{s}) \tag{5.30}$$

where $g_\gamma(\mathbf{r}) = g_\gamma[\rho(\mathbf{r})]$ and $g^2_\gamma = f_\gamma(\rho)$ with $\gamma = 0, \tau$ for isoscalar and isovector components, respectively. V^d and V^e represent "bare" interaction, i.e., without in-medium effects. This approach ensures a reliable treatment of the density dependence also in the surface region (where the vertices vary rapidly) i.e., for finite nuclei.

5.4 Description of the structure calculations

5.4.1 The construction of vacuum state

In the QRPA theory, a description of the single-particle states is needed to generate the vacuum state $|0\rangle$ over which the QRPA operators will act.
In this work the QRPA approach is applied to study both the projectile and the target transitions. In the case of target transition, the $|^{40}\mathrm{Ca}_{g.s.}\rangle$ is the vacuum state, while in the case of the projectile, the vacuum state is $|^{18}\mathrm{O}_{g.s.}\rangle$.
The single particle wave function ϕ were obtained as eingefunctions of a Wood-Saxon potential with nuclear, spin-orbit and Coulomb terms:

$$U(\mathbf{r}) = V_0 f(\mathbf{r}) + V_{LS} \boldsymbol{\sigma} \cdot \mathbf{L} \frac{1}{r} \frac{df}{dr} + \frac{1}{2}(1 - \tau_z) V_C(\mathbf{r}) \tag{5.31}$$

where V_c is the Coulomb potential of a uniform sphere of radius $R_c = R_0 A^{-1/3}$, with R_0 radius of the central part of the potential, and $f(\mathbf{r})$ is the Wood-Saxon function with

reduced radius r_0 and diffuseness a.

$$f(\mathbf{r}) = \left[1 + e^{\frac{r - r_0 A^{1/3}}{a}}\right]^{-1} \tag{5.32}$$

The parameters of the mean field were calculated by fitting the single particle energies in the region near the Fermi surface, obtained or through an Hartree-Fock-Bogoliubov (HBF) calculation [151] or from experimental value.
The single particle wave function were calculated solving the eingenvalue problem in the mean filed for excitation energies $E_x \leq$100 MeV and angular momenta $L \leq$6 in a box with radius of 60 fm.

5.4.2 The state-dependent pairing field

In the QRPA theory, the effective particle-hole correlations are described in terms of quasiparticle interactions, which may be taken into account by a state-dependent pairing field. As discussed, in Section 5.2, the emptiness and occupation amplitudes u_j and v_j necessary to construct the 1QP operators, are determined by pairing correlations between nucleons. In the pairing theories, like that of Bardeen-Cooper-Schieffer (BCS), these amplitudes provide the probability that a singlet even pair of particles occupies the orbital with angular momentum j. Unfortunately in the BCS theory the pairing field is independent of the state and thus not suitable for an application where the pairing interaction is expected to be not negligible.
In the present model, a state-dependent pairing field is calculated with a density dependent interaction, obtained by projection of the NN-interaction of Ref.[145] (described in Section 5.3) to the Singlet Even particle-particle channel ($S = 0$, $L = 0$,$T = 1$). The strength used as input is G=17.5 MeV both in target and in the projectile. The occupation probabilities $|v_j|^2$ and energy shift E_{BCS} produced by the pairing on different orbitals are shown in Table 5.1 both for ^{18}O and ^{40}Ca and for protons and neutrons. The ^{18}O is well described both in terms of level order and occupation probability accordingly to what known for literature [152].

Table 5.1: Parameters obtained, in the case of ^{18}O, from a state-dependent pairing field with input strength G=17.5 MeV. $|v_j|^2$ represent the occupation probabilities and E_{BCS} (MeV) the energy shifts produced by the pairing on different proton and neutron states.

^{18}**O**					
Protons			**Neutrons**		
n l j	$\|v_j\|^2$	E_{BCS}	**n l j**	$\|v_j\|^2$	E_{BCS}
$1s_{1/2}$	1.0	19.269	$1s_{1/2}$	0.999	24.813
$1p_{3/2}$	0.999	9.187	$1p_{3/2}$	0.998	13.948
$1p_{1/2}$	0.999	3.611	$1p_{1/2}$	0.996	9.029
$1d_{5/2}$	0.008	4.602	$1d_{5/2}$	0.572	1.458
$2s_{1/2}$	0.003	7.528	$2s_{1/2}$	0.177	2.581
^{40}**Ca**					
Protons			**Neutrons**		
n l j	$\|v_j\|^2$	E_{BCS}	**n l j**	$\|v_j\|^2$	E_{BCS}
$1p_{1/2}$	1.0	17.334	$2p_{1/2}$	0.999	10.759
$1d_{5/2}$	0.999	8.319	$1d_{5/2}$	0.999	9.214
$2s_{1/2}$	0.999	3.733	$2s_{1/2}$	0.999	4.595
$1d_{3/2}$	0.999	2.020	$1d_{3/2}$	0.999	2.731
$2p_{3/2}$	0.012	2.445	$1f_{7/2}$	0.010	5.109
$2p_{1/2}$	0.008	3.825	$2p_{3/2}$	0.005	9.337
$1f_{7/2}$	0.006	3.886	$2p_{1/2}$	0.002	11.198

On the other hand, the ^{40}Ca is not well described. ^{40}Ca is a doubly closed-shell nucleus where the wave function of the ground state is composed for 88% by $d_{3/2}$, for 6% by $f_{7/2}$ and for 6% by $f_{5/2}$ [94, 95]. The results of the present calculation are not consistent with this picture of the ^{40}Ca$_{g.s.}$. In particular the $1f_{7/2}$ shell is found to be less bound than the p-shell and displays an occupation probability of only 1.2%. In the past, this problem was debated [153]. In order to simulate the softening of the $N = Z = 20$ shell closure, the pairing strength G was increased. This increasing adds a polarization contribution to the pairing interaction [151]. A value of $G_P = 35$ MeV for protons and $G_N = 29.2$ MeV for neutron were chosen. In Table 5.2 the parameters for the ^{40}Ca obtained in this conditions are listed:
The obtained ^{40}Ca structure is consistent to the result shown in Ref. [153] and is compatible to the ground wave function of ^{40}Ca, mentioned above.

Table 5.2: Parameters obtained, in the case of ^{40}Ca. $|v_j|^2$ represents the occupation probabilities and E_{BCS} (MeV) the energy shifts produced by the pairing on different proton and neutron states.

^{40}Ca					
Protons			**Neutrons**		
n l j	$\|v_j\|^2$	E_{BCS}	**n l j**	$\|v_j\|^2$	E_{BCS}
$1p_{1/2}$	1.0	14.502	$2p_{1/2}$	0.999	10.76
$1d_{5/2}$	0.999	9.490	$1d_{5/2}$	0.999	9.221
$2s_{1/2}$	0.999	4.916	$2s_{1/2}$	0.999	4.607
$1d_{3/2}$	0.999	3.208	$1d_{3/2}$	0.999	2.752
$1f_{7/2}$	0.051	3.883	$1f_{7/2}$	0.049	5.118
$2p_{3/2}$	0.034	4.314	$2p_{3/2}$	0.026	9.341

5.4.3 The 4-QP excitation

The 4QP excitations, not included in the 1p-1h (2QP) QRPA theory, are crucial for a correct description of the decay width of giant resonances. In fact, the theoretical values obtained by RPA underestimate systematically the measured widths, especially for heavy nuclei. To account for this collisional broadening of the RPA modes, the Hilbert space has to be extended to include both 1p-1h and 2p-2h excitations [154, 155]. Because of the large number of 2p-2h excitations, a complete treatment in the enlarged 4-QP space is extremely difficult, if not numerically impossible in most cases. Therefore a number of semiempirical approximations have been specifically developed for the description of the excitation energy continuum, obtaining an average 2p-2h contribution [144]. It is important to note that the equations formulated in the extended space are projected on the 1p-1h subspace, where the 2p-2h contributions are described by the matrix elements of a complex energy-dependent effective potential. In this way, the effect of the 2p-2h excitations appears as additional 1p-1h self-energy, producing an energy dependent shift and broadening of the RPA response functions and transition densities. The real and imaginary part of the matrix elements are related by a general dispersion relation [144], accounting for the larger broadening effect on the more shifted structures.

It is seen that this approach does not introduce further ground state correlations. In fact, no extra strength is associated to the enlarged space, so that the final results is

a state-dependent redistribution of the strength and the Energy Weighted Sum Rule (EWSR) remains valid.
In the present case, an empirical formula was derived for the imaginary part of the 2p-2h self-energy by imposing that the broadening is zero on the ^{18}F and ^{40}K ground state and 0.6 MeV at the energy typical for the Giant Dipole Resonance (GDR). The real part is then deduced from the dispersion relation of Ref.[144].

5.5 The results of the CEX-QRPA calculations

CEX-QRPA calculations have been performed, as illustrated in the previous sections, in order to describe the ^{18}F and ^{40}K 1p-1h (2QP) states. In both cases, the allowed energy range for the 2QP excitations is maintained up to 80 MeV to avoid the cut-off of important correlations determined by the off-the energy shell components.
The QRPA level density distributions (per MeV) for charge exchange transitions from $^{18}O_{g.s.}$ to excited states of ^{18}F and from $^{40}Ca_{g.s.}$ to excited states of ^{40}K are shown in Fig.5.1 and 5.2 respectively. They are calculated for $E_x \leq 15$ MeV and multipolarities from 0^+, 0^- to 5^+, 5^-, both for natural and unnatural parities. These quantities are obtained by normalizing the QRPA multipole response functions to the NEWSR of the same operator:

$$d^{QRPA}(\omega, P_\alpha) = \frac{R_\alpha^{QRPA}(\omega, P_\alpha)}{S_0(P_\alpha)}, \qquad \int d\omega d^{QRPA}(\omega, P_\alpha) = 1 \tag{5.33}$$

The presence of peaks at certain excitation energies and transferred angular momenta (j^π) indicates that finite probabilities are calculated for the $^{18}O_{g.s.} \rightarrow {}^{18}$F and $^{40}Ca_{g.s.}$ $\rightarrow {}^{40}$K transitions.

5.5.1 The results for the $^{18}O_{g.s.} \rightarrow ^{18}F$ transition

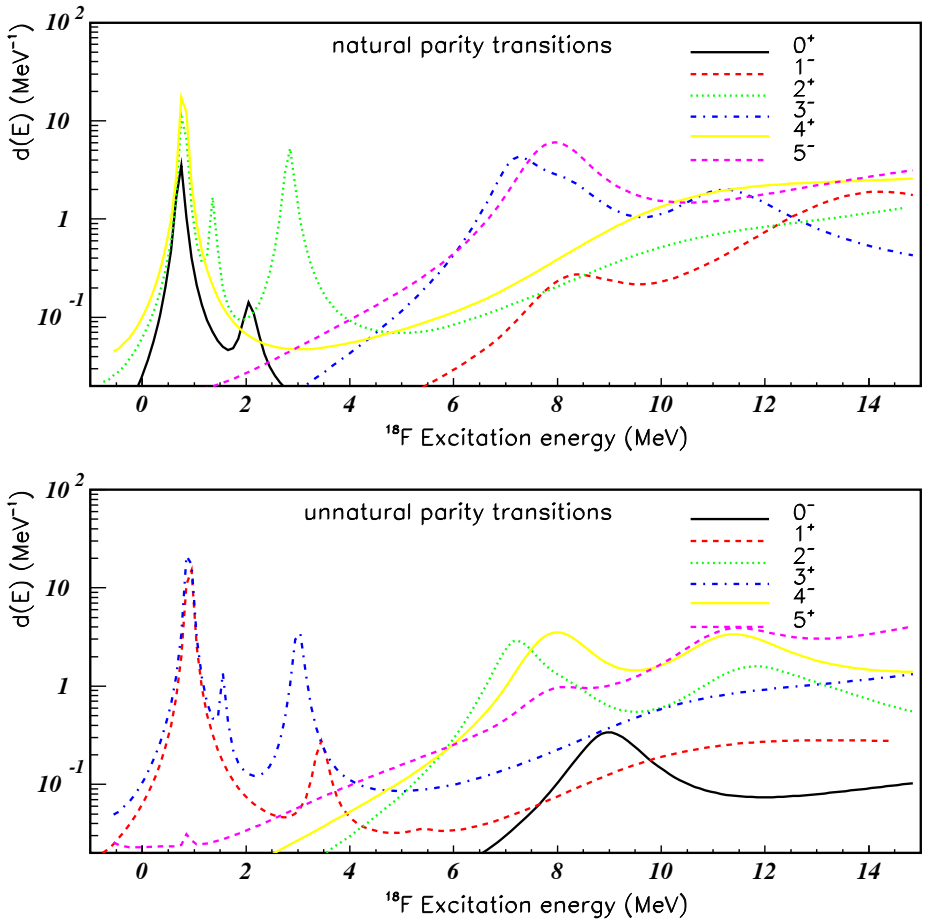

Figure 5.1: QRPA level densities for CEX transitions from $^{18}O_{g.s.}$ to excited states of ^{18}F. These quantities represent, for each multipolarity the ratio between each response function and the respective sum rule at each energy. The bin is 50 keV. In the upper panel, the natural parity transitions are shown, while in the lower panel, the unnatural parity ones.

Transitions to different discrete levels of ^{18}F are observed. The simultaneous presence of one peak at a fixed energy, in different J^π transitions, indicates which orbitals are involved in the transitions.

The $^{18}O(d_{5/2}) \rightarrow ^{18}F(d_{5/2})$ transition is expected to be the lowest energy level for multipolarities 0^+, 1^+, 2^+, 3^+, 4^+, 5^+. Indeed, a peak at 1 MeV for such transitions is

observed. It is compatible with the ^{18}F ground state, that it know to be a 1^+ state [156].

Two transitions are observed in the calculated level densities for the 2^+, 3^+ multipolarities at about 2 and 3 MeV. These can be only associated to the $^{18}\mathrm{O}(d_{5/2}) \rightarrow {}^{18}\mathrm{F}(s_{1/2})$ and $^{18}\mathrm{O}(s_{1/2}) \rightarrow {}^{18}\mathrm{F}(d_{5/2})$ transitions.

The presence of a peak in the 0^+, 1^+ transitions at about 4 MeV is associated to the $^{18}\mathrm{O}(s_{1/2}) \rightarrow {}^{18}\mathrm{F}(s_{1/2})$ transition.

Furthermore, the response functions to the Fermi and Gamow-Teller like operators were calculated according to the eq. 5.17. These allow a comparison with known experimental Gamow-Teller strength $B(GT)$ [89]. We obtain $B(GT) = 2.79$, it is compatible with the known experimental value of about 3.27 [89].

5.5.1.1 The results for the $^{40}\mathrm{Ca}_{g.s.} \rightarrow {}^{40}$K transitions

The obtained spectrum for the $^{40}\mathrm{Ca}_{g.s.} \rightarrow {}^{40}$K transitions is much more complicated than that for the $^{18}\mathrm{O}_{g.s.} \rightarrow {}^{18}$F. Indeed, several peaks are populated in agreement with the high level density characteristic of the ^{40}K structure [137, 138].

A peak at 0.4 MeV is observed for the 2^-,3^-,4^-,5^- multipolarities, it is related to the $^{40}\mathrm{Ca}(d_{3/2}) \rightarrow {}^{40}\mathrm{K}(f_{7/2})$ transition and is compatible with the states multiplet that corresponded to the ground state and first excited states of ^{40}K.

A peak at about 1.8 MeV is presented for the multipolarities ,0^-, 1^-, 2^-, 3^-, and can be associated to the transition $^{40}\mathrm{Ca}(d_{3/2}) \rightarrow {}^{40}\mathrm{K}(p_{3/2})$. A level at about 2.5 MeV is obtained in 3^- and 4^- and it is compatible to the transition $^{40}\mathrm{Ca}(2\mathrm{s}_{1/2}) \rightarrow {}^{40}\mathrm{K}(f_{7/2})$.

The Gamow-Teller strength is distributed in the peak at 0.0 , 0.8 and 2.5 MeV. In fact, the first peak is present at 0^+, 1^+, 2^+, 3^+ and involved a transition $^{40}\mathrm{Ca}(\mathrm{d}_{3/2}) \rightarrow {}^{40}\mathrm{K}(d_{3/2})$. The second peak is observed in the multipolarities 0^+, 1^+, 2^+, 3^+, 4^+, 5^+ and can be associated within a transition $^{40}\mathrm{Ca}(\mathrm{f}_{7/2}) \rightarrow {}^{40}\mathrm{K}(f_{7/2})$ or $^{40}\mathrm{Ca}(\mathrm{f}_{5/2}) \rightarrow {}^{40}\mathrm{K}(f_{5/2})$. The last peak is populated at 0^+, 1^+ and it can involve a $^{40}\mathrm{Ca}(\mathrm{s}_{1/2}) \rightarrow {}^{40}\mathrm{K}(s_{1/2})$ transition. the response functions to the Fermi and Gamow-Teller like operators were calculated (eq.5.17). The obtained value is $B(GT) = 0.046$, it is compatible with the known experimental value of about 0.069[90].

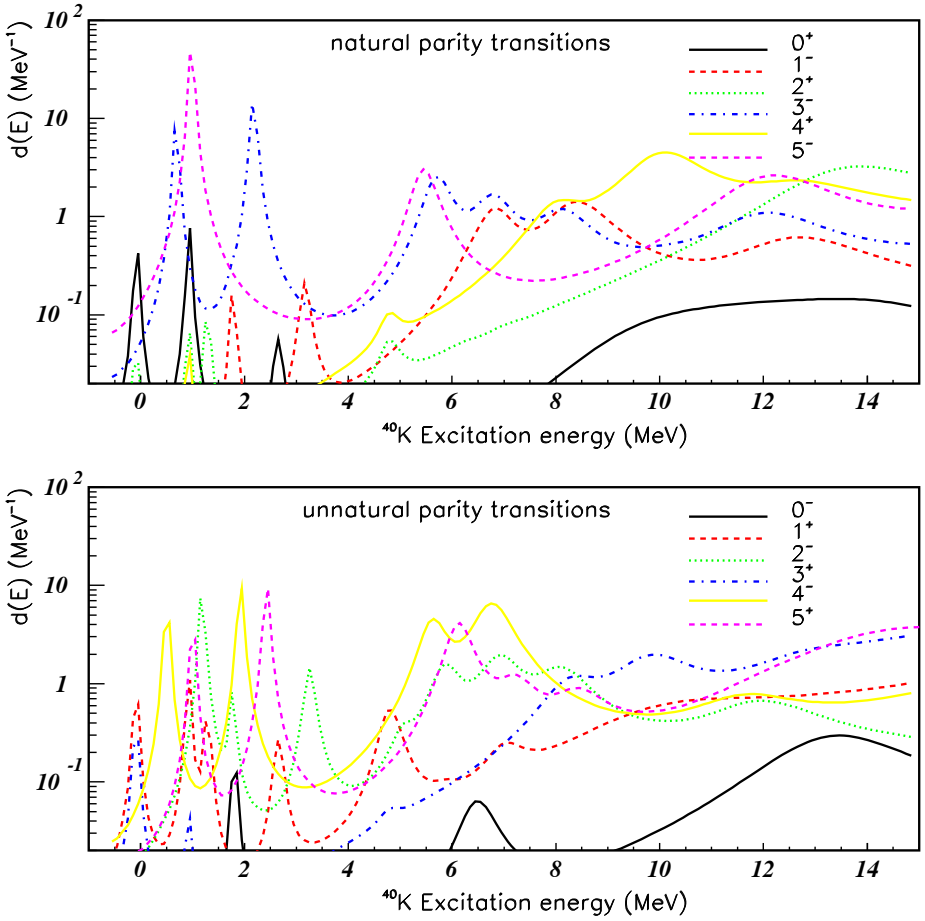

Figure 5.2: QRPA level densities for CEX transitions from $^{40}\mathrm{Ca}_{g.s.}$ to excited states of ^{40}K. The bin is 50 keV. In the upper panel, the natural parity transitions is shown, while in the lower panel, the unnatural parity ones.

5.6 The DWBA cross section calculations

Assuming that the considered charge-exchange reaction proceeds mainly through a direct one-step process, its transition amplitude can be described by the first order DWBA T-matrix element:

$$T^{(1)}_{\beta\alpha} = < \chi^{(-)}_{\beta} | F^{(\tau)}_{\beta\alpha} | \chi^{(+)}_{\alpha} > \tag{5.34}$$

The distorted waves in the incident $\alpha = (a, A)$ and final $\beta = (b, B)$ channel are denoted by $\chi_\alpha^{(+)}$ e $\chi_\beta^{(-)}$, respectively. The charge exchange form factor $F_{\beta\alpha}^{\tau} = \langle bB|V^{(\tau)}|aA\rangle$ is calculated in a double-folding model, as following:

$$F_{\beta\alpha}^{(\tau)} = \int d\xi_a d\xi_A \rho_{ab}(\xi_a)\rho_{AB}(\xi_A)V^{(\tau)}(\mathbf{R}, \xi_a\xi_A) \tag{5.35}$$

where ρ_{ab} and ρ_{AB} are the charge-exchange transition densities for projectile-ejectile ($a \to b$) and target-product ($A \to B$) transitions, respectively. $V^{(\tau)}$ is the isovector part of the nucleon-nucleon effective interaction, which is the component acting in a charge-exchange reaction and determining the exchange of one isospin unit between the target and the projectile.

DWBA calculations, based on the CEX-QRPA transition densities, give the cross sections for the transitions to the ^{40}K single particle states that are overall reproduced by the QRPA calculations. The results of these calculations for the ^{40}Ca(^{18}O,^{18}F)^{40}K reaction and the comparison with the experimental data will be described in the following section.

5.6.1 The T-matrix interaction

The effective NN-interaction used to calculate the charge exchange form factors is taken form the isovector part of the D3Y G-matrix interaction of Hofman and Lenske [145]. The full T-matrix in momentum space can be obtained at low incident energy by extrapolating the density dependent G-matrix interaction, as, e.g. in Ref.[157]. The T-matrix isovector interaction consists of central (scalar and vector), spin-orbit and tensor components, each of them including direct and exchange terms:

$$t_{NN}^{\tau} = \Big[\underbrace{t_\tau^C(r) + t_{\sigma\tau}^C(r)\sigma_{\mathbf{1}}\cdot\sigma_{\mathbf{2}}}_{\text{central}} + \underbrace{t_\tau^{LS}(r)(\mathbf{L}\cdot\mathbf{s_1} + \mathbf{L}\cdot\mathbf{s_2})}_{\text{spin-orbit}} + \underbrace{t_{\tau(r)S_{12}}^T}_{\text{rank-2tensor}}\Big]\tau_{\mathbf{1}}\cdot\tau_{\mathbf{2}} \tag{5.36}$$

It is remarked that the same interaction as in the HFB ground state and QRPA correlated excitations calculations is used. This assures the consistency of structure and reaction calculations. The density dependence of the D3Y G-matrix gives rise to a density dependent T-matrix. The numerical calculations are simplified by using a separable LDA [145, 157] to express this dependence. The global properties of the T-matrix interaction obtained in the various (S, T) channels are given in Table 5.3. The spin-orbit

NN-interactions are neglected. For the isovector channel ($S, T = 1$), the central (without and with spin dependence) and tensor components are shown in momentum space in Fig.5.3, separating the direct and exchange terms. Since peripheral collisions are involved, the reaction takes place principally for linear momentum transfer q from 0 to 1 fm^{-1} in the experimentally explored angles.

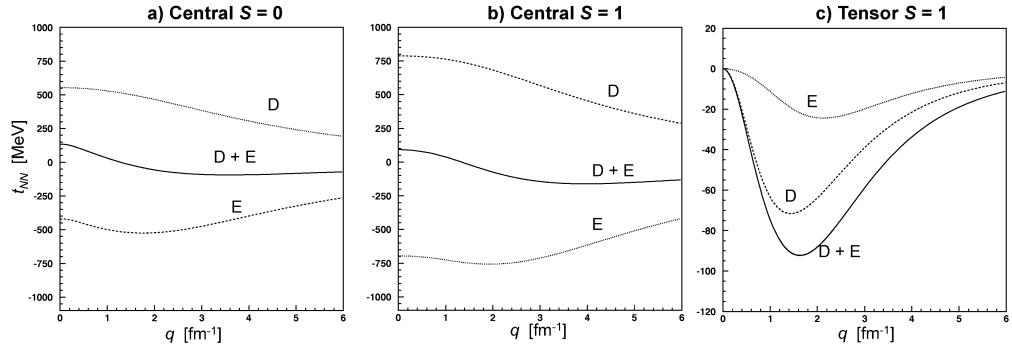

Figure 5.3: Different components of the real isovector part of the effective NN-interaction in the momentum space: a) central scalar ($S = 0$), b) central vector ($S = 1$), c) tensor vector ($S = 1$). For each plot the direct (D) and exchange (E) contributions are shown separately. The total (D + E) is also shown.

In Fig.5.3 one can see that, in the window of q-values considered, the tensor force cannot be neglected. The exchange terms are also important for a correct description of the interaction, expecially for the central $S = 1$ component. However, from Table 5.3 we can see that they are more influential for isoscalar than for isovector interactions.

5.6.2 The CEX form factors

The CEX form factors are calculated microscopically by double folding of the transition densities of the target and the projectile with the effective NN-interaction of Section 5.6.1.

$$F^{(\tau)}_{\beta\alpha}(\mathbf{r}, E) = \int d\mathbf{q} \rho_{^{18}O,^{18}F}(\mathbf{q}) t^{\tau}_{NN}(\mathbf{q}, E) \rho_{^{40}Ca,^{40}K}(\mathbf{q}) e^{i\mathbf{q}\cdot\mathbf{r}}/(2\pi)^3 \qquad (5.37)$$

The CEX-QRPA transition densities given by eq.5.18 are used for both the target (^{40}Ca$\rightarrow^{40}$K) and the projectile (^{18}O$\rightarrow^{18}$F) transitions.

Table 5.3: Volume integrals for the T-matrix interaction in the various (S,T) channels at vanishing density, calculated in the (A,B) rest frame. The interaction used in the CEX form factor calculations is given by the isovector components $(S,T=1)$.

Central (S,T) interaction [MeV·fm^3]				
(S,T)	(0,0)	(0,1)	(1,0)	(1,1)
Direct real	-1082.1	787.3	782.3	-419.2
Direct Imaginary	245.7	159.2	29.2	146.6
Exchange real	440.6	-568.5	-573.5	568.8
Exchange Imaginary	-652.4	69.2	-11.6	-60.8
Modulus	597.6	254.8	117.0	164.8
Tensor (S,T) interaction [MeV·fm^5]				
(S,T)	(0,0)	(0,1)	(1,0)	(1,1)
Direct			17.6	149.0
Exchange			44.4	-17.7
Modulus			26.8	166.7

5.6.3 The optical potential

For the calculation of the scattering amplitudes in the DWBA framework(eq. 5.34), the form factors (eq. 5.37) and the distorted waves $\chi^{(+)_\alpha(k_\alpha,r)}$ and $\chi^{(-)_\beta(k_\beta,r)}$ in the incident $\alpha=(a,A)$ and final $\beta=(b,B)$ channels are needed. The choice of the optical potentials to use in the initial and final channels is important. A double folding approach has been used in order to describe the elastic scattering both in ingoing and outgoing channels. Since the density dependence of the elastic scattering at forward angles is small, the free NN-interaction obtained by Franey and Love at $E_{inc} \geq 50$MeV/u [158, 159] is used to derive the optical potential (both real and imaginary part). The isoscalar and isovector projectile and target ground state densities are folded with a complex T-matrix, which is obtained at the appropriate incident energy by spline extrapolation of the phenomenological Franey and Love potential using the value of the D3Y G-matrix of Ref. [145] at 0 MeV as reference. The folding is made in momentum space using the Fourier transforms of the ground state densities (with (a,A) = (^{18}O, ^{40}Ca) and (b,B) = (^{18}F, ^{40}K) in ingoing and outgoing channel, respectively):

$$U_{opt}(\mathbf{r},E) = \sum_{\tau=0,1} \int d\mathbf{q} \rho_a^\tau(\mathbf{q}) t_{NN}^\tau(\mathbf{q},E) \rho_A^\tau(\mathbf{q}) e^{i\mathbf{q}\cdot\mathbf{r}}/(2\pi)^3 \tag{5.38}$$

5.6.4 The CEX cross sections

The CEX cross sections of the ^{40}Ca(^{18}O,^{18}F)^{40}K reaction are obtained by DWBA calculations, performed with the HIDEX code [151]. The form factors of eq. 5.37 are used as input to solve the scattering equations. The one-step scattering amplitudes of eq. 5.34 are calculated for the transitions to ^{40}K involved in the range energy region between 2-3 MeV. Finally, the double differential direct CEX cross sections are constructed:

$$\frac{d^2\sigma}{d\Omega dE} = \sum_{J_P J_T} \int dE_T S_P^{J_P}(E - E_T) S_T^{J_T}(E_T) \frac{d\sigma_{J_P J_T}}{d\Omega} \tag{5.39}$$

where the sum extends over all the transition multipolarities J_P, J_T of the target and projectile, respectively. Each reduced DWBA cross section $\frac{d\sigma_{J_P J_T}}{d\Omega}$ is weighted by the target $S_T^{J_T}(E_T)$ and projectile $S_P^{J_P}(E)$ response function per energy. In particular, for the projectile, an average response function for the transition 1^+ in the energy region of 1 MeV was taken into account. One should notice that the region around 1 MeV correspond to the QRPA ground state (see Section 5.5.1 and fig 5.1). The angular distributions have been obtained by adding the double differential cross section eq. 5.39 at each energy step.

5.7 Results of the DWBA calculations

The DWBA calculations were performed for the excited states of ^{40}K in the range between 2-3 MeV. As discussed in Section 4.5, this energy region is characterized by the group of 1^+ states at 2.27 and 2.73 MeV [136] but also other possible higher spin states (e.g. 2^-, 3^-, 4^-).

The calculations were performed for the allowed multipolarities: 1^+, 1^-, 2^+, 2^-, 3^+, 3^-, 4^- in the ^{40}Ca(0^+) target. As discussed before, the hypothesis that the reaction in the projectile channel proceeds via ^{18}O(0^+)$\rightarrow$^{18}F(1^+) was assumed.

In Fig.5.4, the experimental angular distribution is shown together with the results of the calculations for the different multipolarities.

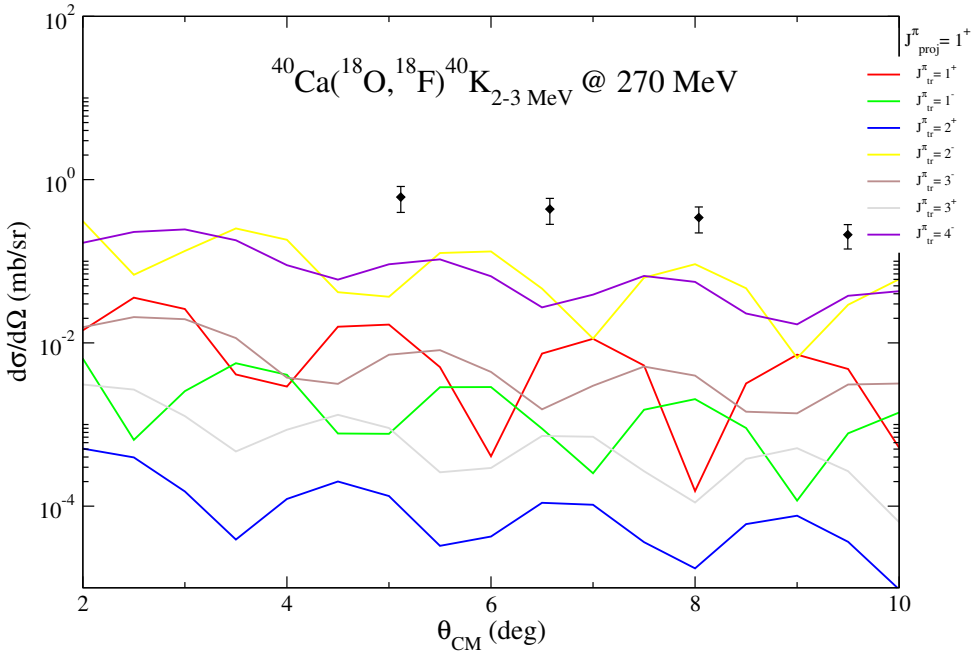

Figure 5.4: Experimental and theoretical angular distribution for the ^{40}Ca(^{18}O,^{18}F)^{40}K$_{2-3\text{MeV}}$ transition. In the calculation the J^{π}_{proj}=1^{+} is assumed for the projectile transition. The lines show the decomposition of the calculated cross section in terms of the angular momentum J_{tr} transferred in the target.

One can easily note that the unnatural parity components 2^{-} and 4^{-} are predominant. In Fig. 5.5, the incoherent sum of the cross section contributions is shown. It underestimate the experimental cross section by a factor about 2. This is possibly due to the fact that the ejectile excitation contribution was not considered in present calculations, while it is known that it is not negligible as evident from the ^{40}K spectrum shown in Fig. 4.19 (the peak referred to the ejectile excitation are labelled with the symbol *). However, the 1^{+} transition contributes to the incoherent sum by a factor ∼1/10. The next step of this analysis is to take into account also other transitions in the projectile.

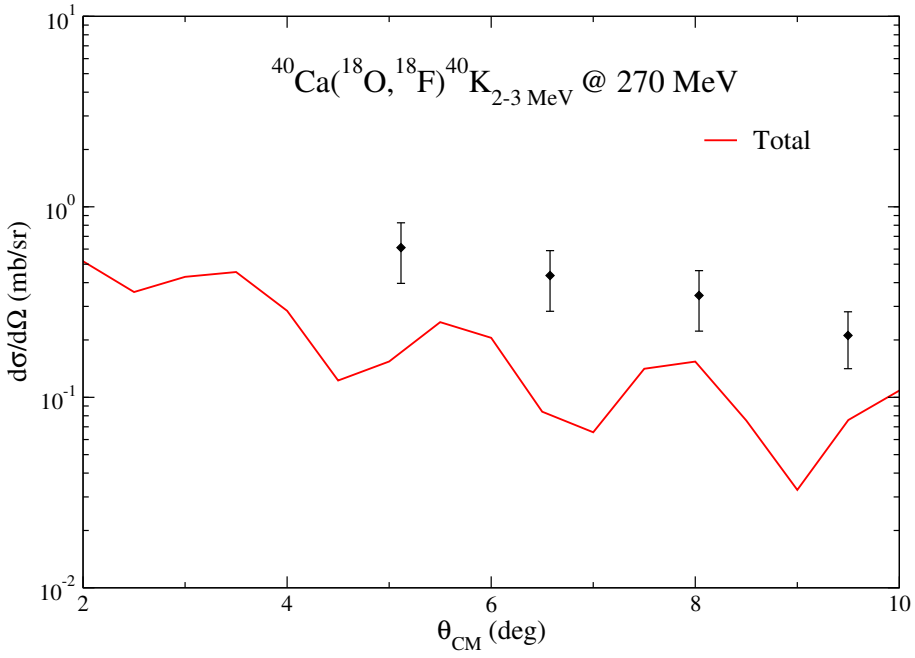

Figure 5.5: Calculated angular distribution for the ^{40}Ca(^{18}O,^{18}F)^{40}K$_{2-3\text{MeV}}$ transition. The calculated cross sections are not scaled. The experimental angular distributions is shown.

5.8 Future development

A future development of the present theory in order to describe the DCE cross-section is planned. The ^{40}Ca(^{18}O,^{18}Ne)^{40}Ar DCE reaction will be studied, following an approach based on the Multi-step Direct theory (MSD) originally proposed by Tamura, Udagawa and Lenske [160]. In the MSD theory, the evolution of the projectile-target system is described by a combination of direct reaction formalism and microscopic nuclear structure calculations within a statistical method. For this reason it is important not only to have a good description in terms of structure and dynamic of the first step channel but also of the second step (^{40}Ar(^{18}Ne,^{18}F)^{40}K reaction) involved in the ^{40}Ca(^{18}O,^{18}Ne)^{40}Ar DCE reaction. Thus, also the second step will be studied in the framework of the CEX-QRPA approach, as described above.

5. THEORETICAL ANALYSIS OF THE ^{40}CA(^{18}O,^{18}F)^{40}K REACTION IN THE CEX-QRPA APPROACH

Chapter 6

A new model to extract the $0\nu\beta\beta$-NMEs

As discussed in Chapter 1, the nuclear matrix elements play a key role in the knowledge of $0\nu\beta\beta$ decay. In this Chapter, an innovative method to infer the nuclear matrix elements by measuring the cross-section of a DCE reaction is proposed [87].
The basic idea is that the heavy-ion DCE mimics the full decay process. Indeed, as already explained in Chapter 2, the DCE reactions proceed from the same initial to the some final state as the $\beta\beta$ decay, and pass via the same intermediate nuclei. Another similarity is that they involve Fermi-like (ΔL = 0,1,2...; ΔS= 0; ΔT = 0) or Gamow-Teller-like (ΔL = 0,1,2...; ΔS= 1; ΔT = 1) short-range operators. The particular states of the intermediate channels through which the DCE and $0\nu\beta\beta$ proceed depend to a large extent on the momentum available.
The experimental results which demonstrate that the DCE reaction manly proceed via a direct process will be presented in the first part of this Chapter. After, the simple factorization of the DCE cross section will be discussed. In conclusion, the NME for ^{40}Ar will be exstracted.

6.1 Experimental results

In order to compare the cross sections of the different channels involved in the studied DCE reaction, the spectra counts of ^{40}Ar, ^{40}K, ^{38}Ar, ^{42}Ca are converted in differential cross section by integrating in the solid angle:

$$\frac{d\sigma}{dE} = \int f(\theta, \phi, E) d\Omega = \int_0^{2\pi} d\phi \int_{\theta_{min}}^{\theta_{max}} f(\theta, \phi, E) d\theta \tag{6.1}$$

where

$$f(\theta, \phi, E) = \frac{d^2\sigma(\theta)}{dE d\Omega}$$

The resulting spectra are shown in Fig.6.1 and 6.2.

In the ^{40}Ca(^{18}O,^{20}Ne)^{38}Ar 2p-transfer spectrum in Fig.6.1a, the cross section tends to increase with excitation energy as a consequence of the kinematical Q-matching conditions (Q_{opt}=32 MeV). Known low-lying states are identified [137, 138] indicating the suppression of low multipolarity transitions due to the L-matching conditions (L_{opt} = 6). In Fig.6.1, for each observed peak, the maximum angular momentum (J_{max}) is indicated according to [138]. The L- and Q-optimum for the second step 2n-transfer ^{38}Ar(^{20}Ne,^{18}Ne)^{40}Ar are similar. Thus, multistep transfer reactions are expected to be strongly suppressed in the population of the mismatched (L = 0, Q = -2.9 MeV) ^{40}Ar ground state.

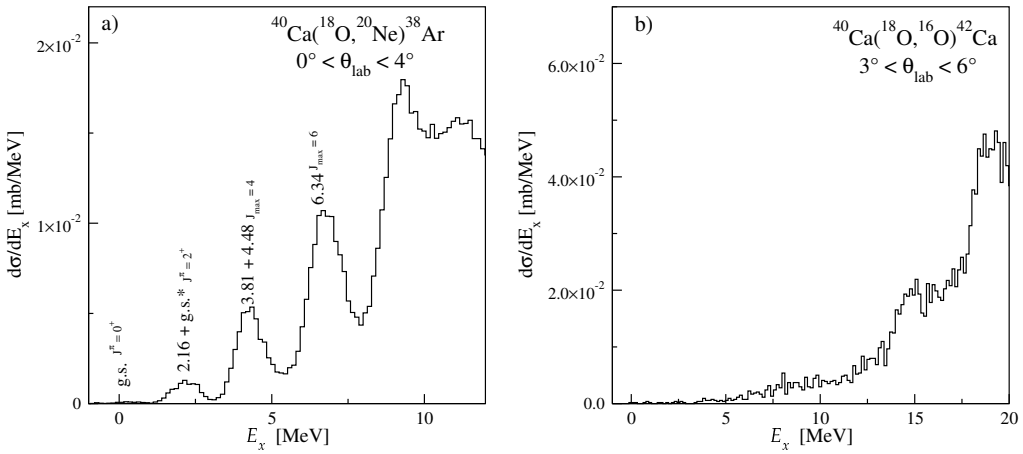

Figure 6.1: Panel a) ^{38}Ar energy spectrum populated in the ^{40}Ca(^{18}O,^{20}Ne)^{38}Ar 2p-transfer. The peak are labelled according to [138]. Panel b) ^{42}Ca enegy spectrum from the ^{40}Ca(^{18}O,^{16}O)^{42}Ca 2n-transfer.

The transition probability $B(I_i \rightarrow I_f)$ from an initial state I_i with spin J_i to a final state I_f with spin J_f through the operator V is:

$$B(I_i \rightarrow I_f) = \frac{C^2}{2J_i + 1} \langle I_f || V || I_i \rangle \tag{6.2}$$

where C is the Clebsh-Gordan coefficient. For the transition from high spin initial states to a final 0^+ state, the corresponding Clebsh-Gordan coefficient will be very small (e.g. for a transition $5^+ \rightarrow 0^+$ $C \sim 1/\sqrt{11}$). Therefore, the required condition of a final two-neutron transfer to the 0^+ $^{40}\mathrm{Ar}_{g.s.}$ gives a supplementary reduction due to the vanishing Clebsh-Gordan coefficients, especially for the high-spin intermediate states.

The cross section for the ^{40}Ca(^{18}O,^{20}Ne)$^{38}\mathrm{Ar}_{g.s.}$ is $\sim$ 3 μb/sr (see Sect.4.6.2) and fig.6.1a), not larger than the ^{40}Ca(^{18}O,^{18}Ne)$^{40}\mathrm{Ar}_{g.s.}$ ($\sim$ 11 μb/sr) (see Sect.4.6.1 and fig.6.2). This is very different from what found in ^{14}C + ^{40}Ca at 51 MeV [27]. As discussed in Sect.2.1.1, Drake at al. found for the ^{40}Ca(^{14}C,^{16}O)^{38}Ar 2p-transfer cross section of about 1 mb/sr, i.e. almost two orders of magnitude larger than the corresponding ^{40}Ca(^{14}C,^{14}O)^{40}Ar DCE [27]. Bes et al. [161] and Dasso and Vitturi [80] conclude that the ^{14}C + ^{40}Ca $\rightarrow$ ^{16}O + ^{38}Ar $\rightarrow$ $^{14}\mathrm{O}_{g.s.}$ + $^{40}\mathrm{Ar}_{g.s.}$ transfer route is the leading mechanism feeding the $^{40}\mathrm{Ar}_{g.s}$ in that experiment. The reason is the much better matching of the 2p-transfer in the ^{14}C + ^{40}Ca (Q_{opt} = 10 MeV, L_{opt} = 3) compared to the present case. Assuming a similar scaling between 2p-transfer and DCE for the present data, an upper limit of 30 nb/sr in the (^{18}O,^{18}Ne) reaction channel is estimated for the ^{18}O + ^{40}Ca $\rightarrow$ ^{20}Ne + ^{38}Ar $\rightarrow$ $^{18}\mathrm{Ne}_{gs}$ + $^{40}\mathrm{Ar}_{gs}$ multi-step route. This could give a contribution at most at large angles. Even possible interference of this channel with the direct DCE are thus small ($\sim$ 10%).

The 2n-pickup 2p-stripping channel ^{18}O + ^{40}Ca $\rightarrow$ ^{16}O + ^{42}Ca $\rightarrow$ $^{18}\mathrm{Ne}_{g.s.}$ + $^{40}\mathrm{Ar}_{g.s.}$ is unlikely to contribute significantly since the first step is already very suppressed in our experiments, with cross sections (see Fig.6.1b) which are about half the cross section of the 2p-transfer.

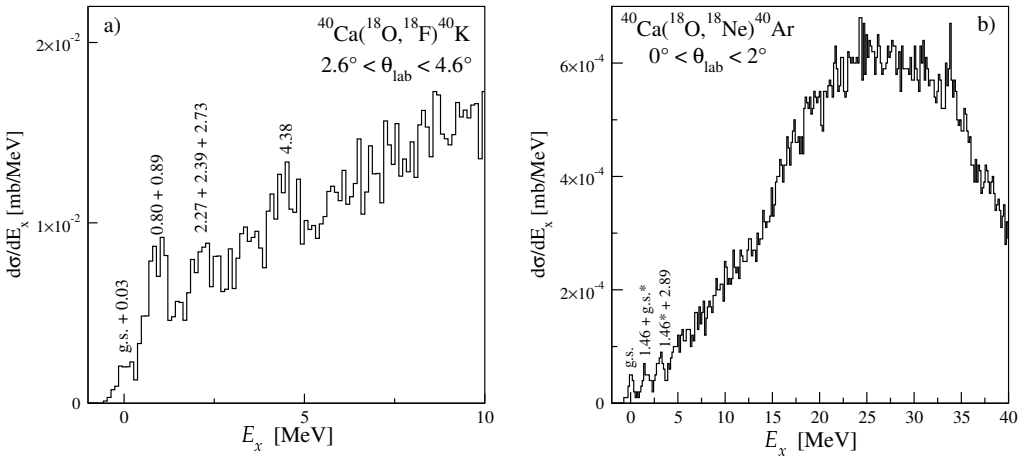

Figure 6.2: Panel a) ^{40}K energy spectrum populated in the ^{40}Ca(^{18}O,^{18}F)^{40}K single charge exchange. The peaks are labelled according to [136, 162]. The symbol g.s* indicates the ^{40}Ca(^{18}O,^{18}F$_{0.937}$)^{40}K transition. Panel b) the ^{40}Ar energy spectrum populated in the ^{40}Ca(^{18}O,^{18}Ne)^{40}Ar DCE. The g.s* and 1.46* symbol indicate the ^{40}Ca(^{18}O,^{18}Ne$_{1.87}$)^{40}Ar and ^{40}Ca(^{18}O,^{18}Ne$_{1.87}$)^{40}Ar$_{1.46}$ transitions, respectively

The ^{40}Ca(^{18}O,^{18}F)^{40}K single charge-exchange spectrum is shown in Fig. 6.2a. The group of 1^+ states at 2.27 and 2.73 MeV is also populated even if other high spin states could hide them. The cross section for these GT transitions is about 500 times larger than the DCE transition to the ^{40}Ar ground state (see Section 4.6.3).

These results indicate that the DCE reaction proceed mainly through the direct mechanism, whereas the concurrent channel (2n-pickup 2p-stripping channel and 2p-stripping 2n-pickup one) are very suppressed.

The angular distribution for the selected transition to the ^{40}Ar 0^+ ground state, shown in Fig. 6.3 is another evidence in support of the direct mechanism.

It shows a slope very similar to that predicted in Section 2.3.3. A clear oscillating pattern is observed. The location of the first minimum at about 2° and the period of the oscillations agree with a pure $L = 0$ angular momentum transition, which is expected due to the 0^+ to 0^+ transitions in both the projectile and target systems. Such an oscillating pattern is not expected in complex multistep transfer reactions, due to the many angular momenta involved in the intermediate channels, which determine a structure-less cross section slowly decreasing at larger angles [80].

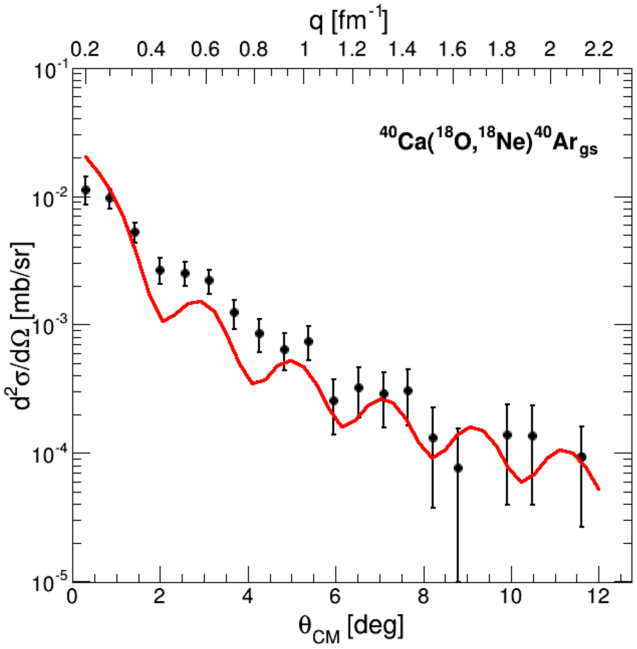

Figure 6.3: Differential cross section of the ^{40}Ca(^{18}O,^{18}Ne)^{40}Ar$_{g.s}$ transition as a function of the θ_{CM} and q. The red curve represent the L=0 Bessel function folded with the experimental angular distribution ($\sim 0.4°$) and scaled to reproduce the incoherent sum of the predicted double F and GT cross section (see Section6.3.3)[87].

The position of the minima is well described by a $|j_0(qR)|^2$ Bessel function, where $R = 1.4(A_1^{1/3} + A_2^{1/3})$ and $A_{1,2}$ is the mass number of projectile and target. The Bessel function presents a slightly different shape at forward angles compared to the experimental angular distribution. This is expected since a plane-wave description is not appropriate [163]. Despite that, a very simple model of $L = 0$ direct process reasonably well describes the main features of the experimental angular distribution.

6.2 Factorization of DCE cross section

In the present Section, a simple model to describe the DCE cross section will be described. It basically consists in a generalization of the well-established factorization of the single charge-exchange cross section [97].

6.2.1 Factorization of the single charge exchange cross section

A well defined and nuclear structure independent proportionality between single charge exchange reaction cross sections, such as (n,p) or (p,n) [97, 164, 165], and beta decay transition strengths is firmly established. The basic idea behind the proportionality is the similarity of the operators involved in each type of reaction. The central isovector terms in the effective nucleon-nucleon interaction, that mediate low momentum transfer spin-flip ($S = 1$):

$$\sum_i V_{\sigma\tau}(\mathbf{r}_{ip})\boldsymbol{\sigma}_i \cdot \boldsymbol{\sigma}_p \boldsymbol{\tau}_i \cdot \boldsymbol{\tau}_p$$

and non-spin flip ($S = 0$) transitions,

$$\sum_i V_{\sigma\tau}\boldsymbol{\tau}_i \cdot \boldsymbol{\tau}_p$$

are similar to the corresponding operators:

$$G_A \sum_i \boldsymbol{\sigma_i}\mathbf{t}_\mathbf{i}^{\pm} \quad \text{and} \quad G_V \sum_i \mathbf{t}_\mathbf{i}^{\pm}$$

for Gamow-Teller (GT) and Fermi (F) beta decay, respectively.
A typical formulation of this property is given as follows:

$$\frac{d\sigma}{d\Omega}(\mathbf{q},\omega) = \hat{\sigma}_\alpha(E_p, A)F_\alpha(\mathbf{q},\omega)B_T(\alpha)B_P(\alpha) \tag{6.3}$$

where $\mathbf{q}$ is the linear momentum transfer and $\omega = Q - Q_0$ is the excitation energy. B_T and B_P are the target and projectile β-decay transition strengths (also called reduced matrix elements) for α operators, where α = Fermi (F) or Gamow-Teller (GT). In particular the reduced GT transition strength $B(GT)$ for the transition from the initial state with spin j_i, isospin T_i and z-component of isospin T_{zi} to the final state with j_f, T_f and T_{zf} is given by [166]:

$$\begin{aligned} B(GT) &= \frac{1}{2J_i+1}\frac{1}{2}\frac{C_{GT}^2}{2T_f+1}\left|\langle J_f T_f|||\sum_{j=1}^{A}(\sigma_\mathbf{j}\tau_\mathbf{j})|||J_i T_i\rangle\right|^2 = \\ &\frac{1}{2J_i+1}\frac{1}{2}\frac{C_{GT}^2}{2T_f+1}[M_{GT}(\sigma\tau)]^2 \end{aligned} \tag{6.4}$$

where C_{GT} is the isospin ClebschGordan (CG) coefficient and the M_{GT} is the GT matrix element.

The quantity $\hat{\sigma}_\alpha$, called "unit cross section", is of primary interest since it almost behaves as an universal property of the nuclear response to F and GT probes. The dependence on the projectile energy E_p and on the target mass number A is in fact quite smooth and calculable all along the nuclear chart. In a rigorous Distorted Wave approach as that proposed by F. Osterfeld [164] or T.N. Taddeucci [97] the unit cross section for a single charge exchange process is found to be factorized as:

$$\hat{\sigma}(E_p, A) = K(E_{p'}, 0)|J_{ST}|^2 N_{ST}^D \tag{6.5}$$

where $K(E_p, \omega)$ is a kinematic factor:

$$K(E_p, \omega) = \frac{E_i E_f}{\hbar^2 c^2 \pi^2} \frac{k_f}{k_i}$$

$E_{i,f}$ and $k_{i,f}$ represent the reduced energy and the wave number in the entrance and exit channel, respectively. J_{ST} represents the volume integral of the relevant nucleon-nucleon interaction component $V_{\sigma\tau}(r)$ or $V_\tau(r)$. The N_{ST}^D, called "distortion factor", is defined by the ratio of distorted waves over plane waves cross sections:

$$N^D(\mathbf{q}, \omega) = \frac{\sigma(\mathrm{DW}; \mathbf{q}, \omega)}{\sigma(\mathrm{PW}; 0)}$$

This term expresses the distortion of the incoming and outcoming waves in the scattering. In basic heavy-ion scattering theory this distortion is determined by the action of a complex optical potential, where the real part accounts for the direct elastic scattering of the two colliding systems and the imaginary part is needed to describe the absorption of incoming flux into the many channels open in the reaction.
The factor $F(\mathbf{q}, \omega)$ describes the shape of the cross section distribution as a function of the linear momentum transfer q and the excitation energy ω. For $L = 0$ transitions, it depends on the square of the $J_0(qR)$ spherical Bessel function (as discussed in Section 2.3.3) [97]. In order to apply the factorization of the cross section (eq.6.3) for accurate determination of the reduced matrix elements B, it is required that the two-step multi-nucleon transfers are negligible, a minimum amount of linear momentum is transferred and the tensor components in the strong interaction are small compared to the central. The latter two conditions are set to better emulate the properties of β-decay operators. These constraints can be experimentally satisfied, especially for light-ion induced reactions such as (n,p), (p,n), (^{3}He,t), (t,^{3}He) at bombarding energies above 100 MeV/u [85, 166]. Thus single charge exchange reactions are routinely used as a

tool to determine $B(GT)$ and $B(F)$. For heavy-ion induced reactions, the data analyses are typically more complicated, due to the introduction of the projectile degrees of freedom and the sizeable amount of momentum transfer. However, a relevant simplification is determined by the strong absorption of the scattering waves in the interior of the colliding systems and the consequent surface localization of these reactions. As a consequence also in these cases the use of fully consistent microscopic approaches with double folded potential for the reaction form factors still allows the determination of $B(\alpha)$ within 10-20% [141].

6.2.2 Generalization to the Double Charge Exchange

As discussed above, the specificity of the single charge exchange process is expressed in the unit cross section (eq. 6.5) through the volume integrals of the $\sigma\tau$ and τ potentials, while the other factors are general features of the scattering processes. In particular for heavy-ion colliding systems the factorization of the cross section in a reaction and a nuclear structure part is a good approximation thanks to the surface localization of the direct reaction as a consequence of the strong absorption in the inner region. The quasi-elastic reactions tend to be in fact originated in a narrow portion of the target and projectile surfaces, where the complicated effects of polarization of the nuclei and Pauli repulsions of the overllaping densities are small [163, 164]. As a consequence, the effect of the many-body nucleus-nucleus potential can be expressed in terms of an optical potential (mapped at the surface) giving the direct elastic scattering of two frozen densities and a small perturbation describing the reaction operator. Small deviations from locality, due for example to the Pauli non locality induced by the exchange of nucleon coordinates, are accurately accounted for as effective velocity dependences in modern state of the art double folding optical potentials [99, 167].
Under the hypothesis of a surface localized process, a generalized version of eq.6.3 could be extracted also for double charge exchange reaction within a similar distorted wave approach. In this case a model for two-vertices interaction is needed to extract physical information from measured DCE cross sections. A complete and coherent theory of such an interaction is not existing at the present time.
In a simple model of DCE reaction one can assume that the process is just a second order charge exchange, where a two proton $j^\pi = 0^+$ pair in the target is converted in a $j^\pi = 0^+$ a two-neutron pair in the projectile by the exchange of two uncorrelated

mesons, which is consequently converted in a two-proton $j^\pi = 0^+$ pair. The lack of correlation between the two exchanged mesons is an approximation that is needed just as guideline for simple estimations. In this model the exchange of each single meson generates the same nuclear transitions as the single charge exchange operators. These are represented by the $B(\alpha)$ strengths of eq. 6.3 for angular momentum part of the matrix elements and by the volume integrals for the radial part. Since there are two mesons the action on the nuclear structure is repeated two-times.
The generalized version of eq. 6.3 is extracted also for DCE is:

$$\frac{d\sigma}{d\Omega}(\mathbf{q},\omega)^{DCE} = \hat{\sigma}_\alpha^{DCE}(E_p, A) F_\alpha^{DCE}(\mathbf{q},\omega) B_T^{DCE}(\alpha) B_P^{DCE}(\alpha) \tag{6.6}$$

where the superscripts indicate that the factors refer to the DCE process. The $B_{T,P}^{DCE}(\alpha)$ are directly connected to the nuclear matrix elements of the $\beta\beta$-decay [168]. Simple relations hold in the very relevant case of $0^+ \to 0^+$ transitions connecting the ground states of even-even nuclei. For example in a double Fermi transition, i.e. a transition where a Fermi operator acts twice, one obtains:

$$B(2F) = B^+(F) B^-(F)$$

In the case of double Gamow-Teller one gets:

$$B(2GT) = \frac{1}{3} B^+(GT) B^-(GT)$$

where the 1/3 factor accounts for the $1/(2j_n + 1)$ factor of one of the GT transitions (see eq. 6.4), which determines a $1^+ \to 0^+$ from the intermediate odd-odd to the final even-even nucleus. A DCE unit cross section can be defined:

$$\hat{\sigma}^{DCE}(E_p, A) = K(E_{p'}, 0) |J_\alpha^{DCE}|^2 N_\alpha^{DCE} \tag{6.7}$$

As discussed above, the specificity of the single or double charge exchange processes is expressed in the $\hat{\sigma}_\alpha$ through the volume integrals of the potential. One also needs to describe the off-shell propagation in the intermediate nuclear state $|n\rangle$ involved in the transition. This gives rise to a VGV-like term in the volume integral $|J_\alpha^{DCE}|^2$ which describes the action of the interaction V in two vertices. It has a non-vanishing contribution in a region that depends on the neutron-proton correlation length [169]. The explicit form of the propagator is:

$$G = \sum_n \frac{|n><n|}{E_n - (E_i + E_f)/2} \tag{6.8}$$

where $E_{i,n,f}$ indicates the energies of the initial, intermediate and final states. In particular, E_n is a complex number whose imaginary component represents the off-shell contributions due to the short living virtual intermediate states. When referring to a virtual state, we indicate a state which lives for a transit time and does not represent the asymptotic state of the reaction. It is not observable and can be accessed only during the reaction. In the limited time during which it lives the energy-time uncertainty principle allows that the energy balance can be violated of an amount given by $\Delta E \Delta t \sim \hbar$ in the sense described in Ref. [86]. The intermediate virtual state can have energies that are different from those (measurable) at stationary conditions. In practice, a supplementary contribution to the line width appears for the intermediate virtual states. This energy interval is called off-shell energy.
One can notice that $\hat{\sigma}_\alpha$ is related to the corresponding quantity for single charge exchange of the same nuclei at the same incident energy, expressed in eq. 6.7. In particular all the three factors can be directly connected and compared in the single and double charge exchange.

6.3 Cross section analysis

In order to demonstrate the validity of the factorization in eq. 6.6, the unit cross section and matrix element for the DCE process are deduced, assuming either a pure double GT or F transition.

6.3.1 Double Gamow-Teller transition

The first calculated ingredient is the J_{GT}^{DCE} volume integral for the ^{18}O + ^{40}Ca $\rightarrow$ ^{18}F$_{g.s.}(1^+)$ + ^{40}K$_{0-8\mathrm{MeV}}(1^+)$ $\rightarrow$ ^{18}Ne$_{g.s.}$ + ^{40}Ar$_{g.s.}$ at 270 MeV incident energy. It has been estimated starting from the single charge exchange volume integral, calculated within the CEX-QRPA approach described in the previous Chapter. We get $J_{GT} = 214$ Mev·fm^3 using the isovector parts of the D3Y G-interactions [145], which includes spin-dependent and spin-independent direct and exchange central interactions (see Table 5.3).
The G propagator of eq. 6.8 is calculated summing over the on-shell energy distribution of ^{40}K 1^+ states observed in high resolution (^{3}He,t) data on ^{40}Ca target [90] and on ^{18}F

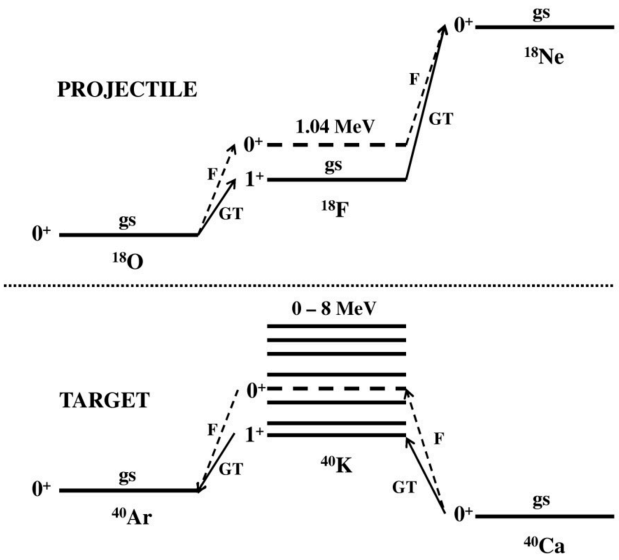

Figure 6.4: Diagram for GT and F projectile and target transitions used for the determination of the $B(2GT)$ and $B(2F)$

1^+ ground state, as sketched in Fig. 6.4. The off-shell contribution to G, accounting for ∼7 MeV (FWHM), is estimated from the crossing time ($\Delta t \sim 27$ fm/c) of the two pairs of nucleons participating in the DCE at 15 AMeV, assuming a correlation length of 4.8 fm from Ref. [169].

A distortion factor $N_\alpha^D \sim 0.042$ is calculated as the ratio of Distorted Wave over Plane Wave single charge exchange. The calculation of the Distorted Wave part was described in Section 5.7 of Chapter 5, by using the Double folding optical potential developed in Section 5.6.3. The same framework has been adopted to evaluate the Plane Wave cross section.

Taking into account the kinematic factor $K \sim 0.0089$ a $\hat{\sigma}_{GT}^{DCE} \sim 87$ μb/sr is estimated for the ^{40}Ca(^{18}O,^{18}Ne)^{40}Ar DCE reaction at $q = 0$ from eq. 6.7.

The correction factor F_{GT}^{DCE} for $q = 0.18$ fm^{-1}, corresponding to θ_{CM} ∼0° is:

$$F_{GT}^{DCE} \sim 0.72$$

From the measured cross section ($\frac{d\sigma}{d\Omega}(\theta_{CM})$=11 μb/sr), in the hypothesis of pure Gamow-Teller transition one obtains the measured strength from eq. 6.6:

$$B^{DCE}(GT) = B_T^{DCE}(GT)B_P^{DCE}(GT) = \frac{\frac{d\sigma}{d\Omega}^{DCE}(q, E_x)}{\sigma_{GT}^{DCE}(E_p, A)F_{GT}^{DCE}(q, E_x)} \sim 0.26 \qquad (6.9)$$

This is compared to the value obtained combining the strengths for the transitions in the projectile and target sketched in Fig. 6.4 and listed in Table 6.1, taken from literature:

$$B(2GT) = B_P(2GT) \cdot B_T(2GT) = 0.11 \tag{6.10}$$

It is important to stress that the reduced B transition strengths for spin and isospin are used according to eq. 6.4. For the projectile we consider:

$$B_P(2GT) = B[GT;^{18}\mathrm{O}_{g.s.}(0^+) \rightarrow^{18} \mathrm{F}_{g.s.}(1^+)][GT;^{18}\mathrm{F}_{g.s.}(1^+) \rightarrow^{18} \mathrm{Ne}_{g.s.}(0^+)] = 3.50 \tag{6.11}$$

where only the population of the $^{18}\mathrm{F}_{g.s.}$ is taken into account, as found in Ref.[89] and the $B(GT)$ for the second step from [170]. For the target:

$$B_T(2GT) = \sum B[GT;^{40}\mathrm{Ca}_{g.s.}(0^+) \rightarrow^{40} \mathrm{K}(1^+)][GT;^{40}\mathrm{K}(1^+) \rightarrow^{40} \mathrm{Ar}_{g.s.}(0^+)] = 0.031 \tag{6.12}$$

where the sum refers to the transitions to the ^{40}K 1^+ states up to 8 MeV observed in Ref. [156]. The strength of the second step ($B[GT;^{40}\mathrm{K}(1^+) \rightarrow^{40} \mathrm{Ar}_{g.s.}(0^+)]$) are taken from Ref.[156], after correction for the factor $1/(2J_i + 1) = 1/3$ which takes into account the multipolarity $J = 1^+$ of the target (see eq. 6.4).
Under the same hypothesis of pure GT transition, the magnitude of the NME can be derived from the Gamow-Teller strength $B^{DCE}(GT)$:

$$M_T^{DCE}(\alpha) = \sqrt{B}_T^{DCE}(\alpha) = 0.27 \tag{6.13}$$

Table 6.1: Extracted strengths for pure Gamow-Teller transitions and comparison with the literature.

B_P (^{18}O→^{18}F)	B_P (^{18}F→^{18}Ne)	$B_P(2\alpha)$	$E(^{40}\mathbf{K})$ MeV	B_T (^{40}Ca→^{40}K)	B_T (^{40}K→^{40}Ar)	$B_T(2\alpha)$
3.27^a	1.07^b	3.50	2.33	0.014^a	0.34^b	0.031
			2.73	0.069^a	0.31^b	
			4.40	0.018^a	0.18^b	
			4.50-8	$8{\cdot}0.007^a$	0.03^b	

a) From Ref.[90].
b) From Ref.[156].

6.3.2 Double Fermi transition

A similar procedure was applied assuming a pure double Fermi operator for the DCE to the $^{40}\mathrm{Ar}_{g.s.}$. The single charge exchange volume integral has been evaluated as in the Gamow-Teller case (see Section 5.6.1) obtaining $J_F = 208$ Mev·fm^3, very close to the GT case.
Only the ^{40}K 0^+ state at 4.38 MeV and the ^{18}F 0^+ state at 1.04 MeV are considered in the intermediate channel. We obtain $\hat{\sigma} \sim 39$ μb/sr from eq. 6.7 and:

$$B^{DCE}(F) = B_T^{DCE}(F) B_P^{DCE}(F) \sim 0.37$$

where $F_F^{DCE} \sim 0.77$ at $\theta_{CM} \sim 0°$.
Even in this case the value is not far from $B(2F) = 0.42$ expected under the hypothesis of:

$$B(2F) = B_P(F) \cdot B_T(F)$$

where $B_{P,T}(F)$ are the strengths for the projectile and target transitions through the 1.04 MeV and 4.38 MeV 0^+ state of ^{18}F and ^{40}K, respectively. The strengths take into account for the comparison are listed in Table 6.2:

Table 6.2: Extracted strengths for pure Fermi transitions and comparison with the literature.

B_P (^{18}O→^{18}F)	B_P (^{18}F→^{18}Ne)	$B_P(2\alpha)$	B_T (^{40}Ca→^{40}K)	B_T (^{40}K→^{40}Ar)	$B_T(2\alpha)$
2	2	4	0.053[a]	2	0.106

a) From Ref.[90].

Here $B_P(2F) = 4$ is taken from the Fermi sum rule, while the $B_T(2F) = 0.106$ is extracted by [156] and [90]
In the case of pure Fermi process, the magnitude of the NME is:

$$M_T^{DCE}(F) = 0.30$$

6.3.3 DCE nuclear matrix elements

The uncertainty in the determination of M_T^{DCE} is about ±50% estimated by checking the sensitivity of the results to the used parameters.

Both F and GT contribute to the total cross section at $\theta_{CM} = 0°$. Their size can be predicted by

$$B(2GT)\hat{\sigma}_{GT}^{DCE}F_{GT}^{DCE} \sim 5\mu b/sr$$

for Gamow-Teller and

$$B(2F)\hat{\sigma}_{F}^{DCE}F_{F}^{DCE} \sim 13\mu b/sr$$

for Fermi. The comparison is much more accurate than the single estimation due to the common assumptions done. In Fig. 6.3 the Bessel function has been scaled to experimental angular distribution of a quantity equal to the incoherent sum of the predicted F and GT cross sections. This result indicates that both pure F and GT-like extreme models give comparable contributions to the final cross section, and it is a direct consequence of the similar volume integrals for both operators. It is important to stress that the relation between these volume integrals looks like that for nucleon-nucleon interaction at 15 MeV. This indicates that the reaction mechanism is, to a large extent, determined by the effective nucleon-nucleon interaction. Experiments at different incident energies are envisaged in order to explore condition characterized by different weights of Fermi and Gamow-Teller contributions and disentangle the role of each operator.

6.4 Neutrinoless double beta decay matrix elements

As reported in Section 1.6, in $0\nu\beta\beta$ NMEs a combination of Fermi and Gamow - Teller appears (see eq. 1.14), ignoring for simplicity tensor components.
If the cross section in heavy-ion DCE reactions can be factorized, as demonstrated in this work, then the nuclear matrix element measured for DCE reaction will be a different combination of M_F and M_{GT} through the weigths f_F and f_{GT}, respectively:

$$M^{DCE} = f_F M_F^{DCE} + f_{GT} M_{GT}^{DCE} \tag{6.14}$$

where the coefficients f_F and f_{GT} depend on the projectile energy E_p and the momentum transfer q of the reaction.
In the case studied in this work, it turned out that $\Delta L = 0$ Fermi and Gamow-Teller operators give an passing description of the process, as demonstrated in Section 6.3.3. To extract each of them singularly it is necessary to measure two different cross section where F and GT operators contribute differently. Thus the single $B^{DCE}(2F)$ and

$B^{DCE}(2GT)$ and consequently M_F and M_{GT} can be extracted. Therefore, combining them with the g_A and g_V, it is possible obtaining the M($0\nu\beta\beta$). In this work, it is not possible performed that rigorously treatise since the experiment was performed at a single incident energy. However, in the extreme hypothesis of pure Gamow-Teller or Fermi transition the extracted matrix elements are:

$$M_T^{DCE}(GT) = 0.27, \quad M_T^{DCE}(F) = 0.3$$

They are very similar, so even the weighted average, representing a more realistic combination of both contributions, will be.
Assuming the F and GT strengths from literature (see Tables 6.1 and 6.2 respectively), as estimate of the weights in the expression of the DCE 0°-cross section one finds:

$$\begin{aligned}\frac{d\sigma}{d\Omega}(0^\circ, E_x = 0) =& \hat{\sigma}_F^{DCE} F_F^{DCE} B(2F) + \hat{\sigma}_{GT}^{DCE} F_{GT}^{DCE} B(2GT) = \\ & 13\mu\text{b/sr} + 5\mu\text{b/sr} = 18\mu\text{b/sr}\end{aligned} \tag{6.15}$$

It follows that the Fermi weight is $\sqrt{13/18}$, while the Gamow-Teller contribution is $\sqrt{5/18}$. The matrix elements weighted in this way are:

$$M_T'^{DCE}(GT) = 0.14, \quad M_T'^{DCE}(F) = 0.25$$

It is possible to deduce the matrix element for the $0\nu\beta\beta$ decay of ^{40}Ca, using the following relation (see eq. 1.14 ignoring for simplicity the tensor components)[54]:

$$M(0\nu\beta\beta) = \frac{g_V}{g_A}^2 M'^{DCE}(F) + M'^{DCE}(GT) \tag{6.16}$$

where g_V and g_A are the vector and axial coupling constants for the weak interaction, taken from the Ref. [15].
The obtained value, using eq.6.16 is:

$$M(0\nu\beta\beta;^{40}\text{Ca}) = 0.62 \cdot 0.25 + 0.14 = 0.29$$

In the lack of theoretical predictions for ^{40}Ca NME, it is worth to compare this value with the well studied ^{48}Ca. The estimated values of ^{48}Ca NME are in a ranges from 0.76 [78] to 1.98 [71] depending on different models.
The obtained small value of NME for ^{40}Ca reflects the Pauli blocking, which accounts for an overall a factor of about 7, coming from the 14% of the wave function which

can determine the GT and F in ^{40}Ca in comparison to about 40% in ^{48}Ca. In order to compare the obtained matrix element to the NME of $0\nu\beta\beta$ decay of ^{48}Ca, one can remove the Pauli blocking:

$$M(0\nu\beta\beta) \cdot 7 = 2.03$$

It is noteworthy that the obtained number (0.29) is compatible with literature for the calculation ^{48}Ca $0\nu\beta\beta$ NME.

Conclusions

This study is inserted in a research line that aims to access the Nuclear Matrix Element (NME) involved in the half-life of the $0\nu\beta\beta$ decay, by measuring the cross sections of heavy-ion induced Double Charge Exchange (DCE) reactions with high accuracy. The basic point is that the initial and final state of both $0\nu\beta\beta$ decay and DCE processes are the same. In addition, both processes pass through the same intermediate state and the transition operators have a similar mathematical structure.

Determining experimentally the NMEs for $0\nu\beta\beta$-decay is an important task and an old dream of many scientist involved in this research field. To reach this goal, past attempts to use DCE induced by pion or heavy-ions were done, but neither of them was successful.

Nowadays, the evaluation of the NMEs is limited only to state of the art theoretical calculations. But the ambiguities in the models are still too large and the constraints too loose to reach accurate values of the NMEs.

This work shows for the first time experimental data on heavy-ion DCE reaction in a wide range of transferred momenta, with an acceptable statistical significance and good angular and energy resolution. In particular ,(^{18}O,^{18}Ne) reaction at 270 MeV incident energy on ^{40}Ca target was investigated. In order to estimate the contribution of the concurrent channels the ^{40}Ca(^{18}O,^{18}F)^{40}K single charge exchange intermediate channel and the competing processes ^{40}Ca(^{18}O,^{20}Ne)^{38}Ar two-proton transfer and ^{40}Ca(^{18}O,^{16}O)^{42}Ca two-neutron transfer were also studied.

The experiment was performed at Laboratori Nazionali del Sud (LNS-INFN) in Catania using a 270 MeV energy ^{18}O Cyclotron beam impinging on a 279 μg/cm^2 thick ^{40}Ca target. The ejectiles were momentum analysed by the MAGNEX large acceptance magnetic spectrometer and detected by its focal plane detector. This is an ideal

instrument in order to perform such kinds of reaction characterized by very low cross-section and by the need to identify and measure heavy ion at high resolution and at zero degree. It conjugates good energy and angular resolution with a large acceptance both in solid angle and momentum. Since the measurement was performed at 0° a particular care was put on the beam transport and spectrometer setting. Applying the ray-reconstruction procedure the energy spectra and cross section were extracted. An overall energy and angular resolution of about $\sim$ 500 keV and 0.3° were obtained, respectively.

The data analysis of experimental results was aimed to establish whether the transition to $^{40}\mathrm{Ar}_{g.s.}$ is dominant by the direct process.

In the ^{40}Ca(^{18}O,^{18}Ne)^{40}Ar spectrum, the ground state is clearly separated from the group of excited states of ^{40}Ar at 1.460 MeV and ^{18}Ne at 1.887 MeV. Therefore, the angular distribution for the transition of interest to the ^{40}Ar 0^+ ground state was extracted. The transition has a cross section at 0° of 11 μb/sr and a clear oscillating pattern is observed. The location of the first minimum at about 2° and the period of the oscillations agree with a pure $L = 0$ angular momentum transition, as expected from the 0^+ to 0^+ transitions in both the projectile and target systems. Such an oscillating pattern is not expected in complex multistep transfer reactions, due to the many angular momenta involved in the intermediate channels, which determine a structureless cross section slowly decreasing at larger angles.

In the ^{40}Ca(^{18}O,^{20}Ne)^{38}Ar two-proton transfer, the cross section tends to increase with excitation energy as a consequence of the kinematical Q-matching conditions. Known low-lying states were identified indicating the suppression of low multipolarity transitions due to L-matching conditions. The cross section for the the transition to the ground state is $\sim$ 3 μb/sr smaller than the $^{40}\mathrm{Ca}(^{18}\mathrm{O},^{18}\mathrm{Ne})^{40}\mathrm{Ar}_{g.s.}$ one.

The ^{40}Ca(^{18}O,^{16}O)^{42}Ca reaction channel is very suppressed in the experiments, in fact the cross section involved for the transition to $^{42}\mathrm{Ca}_{g.s.}$ are about half the cross section of the 2p-transfer. These results indicate that the DCE reaction proceeds mainly through the direct mechanism, whereas the concurrent channels (2n-pickup 2p-stripping channel and 2p-stripping 2n-pickup one) are very suppressed.

In the ^{40}Ca(^{18}O,^{18}F)^{40}K single charge exchange, the group of 1^+ states (2.27 MeV and 2.73 MeV) is also populated even if other high spin states could hide them. However,

the cross section angular distribution in the energy region between 2 - 3 MeV was extracted. One can deduced that the Gamow-Teller (GT) transitions is about 500 times larger than the DCE transition to the ^{40}Ar ground state.

A microscopic many-body theory for heavy-ion charge exchange reactions was used in order to analyse the ^{40}Ca(^{18}O,^{18}F)^{40}K single charge exchange reaction. The CEX-QRPA approach was used to describe both the ^{40}K and ^{18}F nuclear structure. The CEX-QRPA transition densities were used in the one-step DWBA calculations performed for the excited states of ^{40}K in the range between 2 - 3 MeV. The calculations were based on the hypothesis that the reaction in the projectile channel proceeded via ^{18}O(0^+) $\rightarrow$^{18}F(1^+). The allowed multipolarities 1^+, 1^-, 2^+, 2^-, 3^+, 3^-, 4^- were considered. Comparing the experimental angular distribution and theoretical calculations, the unnatural parity component 2^- and 4^- results to be predominant, while the 1^+ transition contributes to the total cross section by a factor $\sim 1/10$. Furthermore, the incoherent sum of the multipolarities cross section understimates the experimental cross section by a factor 2. It is due to the lack of the ejectile excitation contribution in the present calculation. The results of the CEX-QRPA calculations were also used for the simple model adopted to extract the DCE nuclear matrix element. A future development of the present theory in order to describe the DCE cross section is planned.

Finally, an innovative technique to infer on the nuclear matrix elements by measuring the cross section of a double charge exchange nuclear reaction was proposed. The main assumption are that the DCE reaction is a two-step charge exchange and a surface localized process. The model adopted to describe the cross section of DCE consists in a generalization of the well-established factorization of the single charge-exchange cross section, valid under certain hypothesis, discussed in the thesis. Therefore, the cross section could be factorized in a nuclear structure term, containing the matrix elements, and a nuclear reaction one (the unit cross section).

In order to demonstrate the validity of the factorization, the unit cross section and strengths were deduced, assuming either a pure double GT or F transition. In the pure GT assumption, the ^{18}O to ^{18}Ne double GT transition through the intermediate 1^+ ^{18}F ground state was considered. For the target, the ^{40}Ca to ^{40}Ar double GT transition through the intermediate 1^+ ^{40}K states was taken into account.

When considering a pure F transition, the only 0^+ ^{40}K state at 4.38 MeV and the ^{18}F 0^+ state at 1.04 MeV were considered in the intermediate channel.

The comparison among the calculated strength for Gamow-Teller and Fermi and the values known in literature were encouraging. These demonstrate that the assumptions done on the target and projectile transitions ware reasonable. Indeed in the projectile, the 1^+ ground state of ^{18}F exhausts practically all the GT sum rule and the 0^+ state at 1.05 MeV exhausts the Fermi one. Similarly for the target, where the transition through the 2.73 MeV state largely dominates over the other 1^+ and the transition through 4.4 MeV is the unique 0^+ present. Transitions through other states with higher multipolarities in the intermediate channel are also observed. However, although the cross section could be not negligible, the matrix elements for these transitions require a $1/(2J_i+1)$ factor that severly reduces the matrix elements in the transition from the intermediate state with J_i angular momentum to the final 0^+ state of the daughter.
Furthermore, the comparison between the experimental angular distribution for the transition to the $^{40}\mathrm{Ar}_{g.s.}$ and the predicted cross section was also very encouraging. This result indicated that both pure F and GT-like extreme models give a comparable contributions to the final cross section, and it was a direct consequence of the similar volume integrals for both operators. The relation between these volume integrals resembles that for nucleon - nucleon interaction at 15 MeV. This indicates that the reaction mechanism is largely determined by the effective nucleon -nucleon interaction.
Finally, the nuclear matrix element for the ^{40}Ca was calculated. After removing the Pauli blocking effect, it was compared to the NMEs values found in literature in the case of ^{48}Ca. The obtained value is consistent with the calculation of the ^{48}Ca $0\nu\beta\beta$ NME.
Despite the approximations used in the comparison, the extracted strength and nuclear matrix elements are reasonable within $\pm$ 50%, signalling that the main physics content has been kept. A deeper investigation of DCE reactions will be performed in the future, studying other systems of interest as candidate nuclei for the $0\nu\beta\beta$-decay and using different bombarding energies. Experiments at different incident energies are envisaged in order to explore conditions characterized by different weights of Fermi and Gamow-Teller contributions and disentangle the role of each operator.

References

[1] J. Davis, D. Raymond, D. S. Harmer, and K. C. Hoffman, Phys. Rev. Lett. **20**, 1205 (1968). 1, 6

[2] Y. Fukuda and et al., Phys. Rev. Lett. **81**, 1562 (1998). 6

[3] Q.R. Ahmad and et al (SNO Collaboration), Phys. Rev. Lett. **89**, 011302 (2002). 1, 6

[4] S.T. Petcov, Adv. High Energy Phys. **2013**, 852987 (2013). 1, 5

[5] A. Gouvea and P. Vogel, Prog. Part. Nucl. Phys. **71**, 75 (2013).

[6] J.D. Vergados, H.E. Ejiri, and F. Simokovic, Rep. Prog. Phys. **75**, 106301 (2012).

[7] S.F. King, Rep. Prog. Phys. **67**, 107 (2004). 1, 5

[8] Report to the Nuclear Science Advisory Committee, Neutrinoless Double Beta Decay, 2014. 1, 2, 7, 13, 15, 20, 23

[9] S.R. Elliott and P. Vogel, Annu. Rev. Nucl. Part. Sci. **52**, 115 (2002). 14

[10] S.R. Elliott, Int. J. Mod. Phys. A **18**, 4097 (2003).

[11] Yu. G. Zdesenko, Rev. Mod. Phys. **74**, 663 (2002). 1, 14

[12] E. Caurier and et al., Rev. Mod. Phys. **77**, 427 (2005). 2, 18

[13] J. Engel, P. Vogel, and M. R. Zirnbauer, Phys. Rev. C **37**, 371 (1988). 18

[14] J. Toivanen and J. Suhonen, Phys. Rev. Lett. **75**, 410 (1995). 18

[15] J. Barea and F. Iachello, Phys. Rev. D **79**, 044301 (2009). 18, 127

[16] P. K. Rath and et al., Phys. Rev. C **82**, 064310 (2010). 18

[17] T. R. Rodrigez and G. Martinez-Pinedo, Phys. Rev. Lett. **105**, 252503 (2010). 2, 19

[18] H. Akimune and et al., Phys. Lett. B **394**, 23 (1997). 2, 20

[19] J.P. Schiffer and et al., Phys. Rev. Lett. **100**, 112501 (2008).

[20] D. Frekers, Prog. Part. Nucl. Phys. **64**, 281 (2010).

[21] C.J. Guess and et al., Phys. Rev. C **83**, 064318 (2011).

[22] S.J. Freeman and J.P Schiffer, J. Phys. G: Nucl. Part. Phys. **39**, 124004 (2012). 2, 20

[23] J.D. Vergados, Phys. Rev. D **25**, 914 (1982). 2, 23

[24] S. Mordechai and et al., Phys. Rev. Lett. **61**, 531 (1988).

[25] A. Fazely and L. C. Liu, Phys. Rev. Lett. **57**, 968 (1986).

[26] N. Auerbach and et al., Ann. Phys. **192**, 77 (1989). 2, 23

[27] D. M. Drake and et al., Phys. Rev. Lett. **45**, 1765 (1980). 2, 25, 26, 29, 115

[28] F. Naulin and et al., Phys. Rev. C **25**, 1074 (1982). 2, 27, 29

[29] J. Blomgren and et al., Phys. Lett. B **362**, 34 (1995). 2, 27, 28, 29

[30] P. Ring and P. Shuck, *The Nuclear Many-Body Problem* (Spinger, ADDRESS, 1980). 3, 89, 90, 93

[31] Brender and et al., Nucl. Phys. A **477**, 162 (1988).

[32] H. Lenske and et al., Nucl. Phys. A **482**, 343 (1988). 3, 89

[33] M. Goeppert-Mayer, Phys. Rev **48**, 512 (1935). 6

[34] E. Majorana, Nuovo Cimento **14**, 171 (1937). 6

[35] G. Racah, Nuovo Cimento **14**, 322 (1937). 6

[36] W. H. Furry, Phys. Rev. **56**, 1184 (1939).

[37] H. Primakoff, Phys. Rev. **85**, 888 (1952). 6

[38] F. Reines and C. Cowan, Phys. Rev **92**, 830 (1953). 6

[39] F. Reines and C. Cowan, Phys. Rev. **113**, 273 (1959). 6

[40] B. Pontecorvo, J. Exptl. Theoret. Phys. **33**, 549 (1957). 6

[41] B. Pontecorvo, J. Exptl. Theoret. Phys. **34**, 247 (1958). 6

[42] Z. Maki, M. Nakagawa, and S. Sakata, Prog. Theor. Phys. **28**, 870 (1962). 6

[43] L. Chau and W. Keung, Phys. Rev. Lett. **53**, 1802 (1984). 7

[44] J.N. Bahcall, *Neutrino Astrophysics* (Cambridge University Press, ADDRESS, 1989). 7

[45] C. Kraus and et al., Eur. Phys. J. **40**, 447 . 8

[46] V.M. Lobashev and et al., Nucl. Phys. Proc. Suppl. **91**, 280 (2001). 8

[47] I. Avignone, T. Frank, S.R. Elliott, and J. Engel, Rev. Mod. Phys. **80**, 481 (2008). 8, 14

[48] Y. Yanagida, in *Proceedings of the Workshop on the Unified Theory and the Baryon Number in the Universe*, edited by O. Sawada and A. Sugamoto (Tsukuba, Japan, 1979), No. 79-18, p. 95. 9

[49] M. Gell-Mann, P. Ramond, and R. Slansky, in *Supergravity*, edited by P. Van Nieuwenhuizen and D.Z. Freedman (North-Holland, Amsterdam, 1979), p. 315.

[50] R. N. Mohapatra and G. Senjanovic, Phys. Rev. Lett. **174**, 45 (1980). 9

[51] S.R. Elliott, A.A. Hahn, and M.K. Moe, Phys. Rev. Lett. **59**, 2020 (1987). 9

[52] J. Schechter and J.W.F. Valle, Phys. Rev. D **25**, 2951 (1982). 10, 12

[53] H. M. Georgi, S. L. Glashow, and S. Nussinov, Nucl. Phys. B **193**, 297 (1981). 10

[54] J. Kotila and F. Iachello, Phys. Rev. C **85**, 034316 (2012). 11, 127

[55] A. Smolnikov and P. Grabmayr, Phys. Rev. C **81**, 028502 (2010). 11

[56] F. Simkovic, G. Pantis, J.D. Vergados, and A. Faessler, Phys. Rev. C **60**, 055502 (1999). 12, 16, 17

[57] A. Faessler and F. Simkovic, J. Phys. G **24**, 2139 (1998). 12

[58] M. Agostini and et al., arXiv:1307.4720v1 [nucl-ex] (2013). 15, 16

[59] C. P. Aguirre and et al., arXiv: 1402.0922 . 15

[60] N. Abgrall and et al., Adv. High Energy Phys. **2014**, 365432 (2014). 15

[61] R. Arnold and et al., Eur. Phys. J. C **70**, 927 (2010). 15

[62] J. B. Albert and et al. (EXO-200 Collaboration), arXiv: 1402.6956v1 . 15

[63] A. et al. Gando, Phys. Rev. C **85**, 045504 (2012). 15, 16

[64] J. Hartnell, J. Phys. (Conf. Ser.) **375**, 356 (2012). 15

[65] S. Umehara and et. al., J. Phys. (Conf. Ser.) **39**, 236 (2006). 15

[66] K. Zuber, Nucl. Phys. Proc. Suppl. **138**, 236 (2005). 15

[67] J. Barea, J. Kotila, and F. Iachello, Phys. Rev. Lett. **109**, 042501 (2012). 15, 16, 21, 31

[68] C. Arnaboldi and et al., Phys. Rev. C **78**, 035502 (2008). 16

[69] C. E. Aalseth and et al., Phys. Rev. D **65**, 092007 (2002). 16

[70] R. Arnold and et al, Nucl. Phys. A **765**, 483 (2006). 16

[71] J. Barea, J. Kotila, and F. Iachello, Phys. Rev. C **87**, 014315 (2013). 17, 21, 22, 127

[72] J. F. Berger, M. Girod, and D. Gogny, Nucl. Phys. A **428**, 23 (1984). 19

[73] F. Simkovic, A. Faessler, and P. Vogel, Phys. Rev. C **79**, 015502 (2009). 19, 21

[74] H.E. Ejiri, Phys. Rep. **338**, 265 (2000). 20

[75] V. Rodin, A. Faessler, F. Simkovic, and P. Vogel, Nucl. Phys. A **766**, 107 (2006). 21

[76] F. Simkovic, A. Faessler, V. Rodin, P. Vogel, and J. Engel, Phys. Rev. C **77**, 045503 (2008). 21, 22

[77] K. Muto, Nucl. Phys. A **577**, 415 (1994). 21

[78] E. Caurier, F. Menendez, F. Nowachi, and A. Poves, Phys. Rev. Lett. **100**, 052503 (2008). 21, 22, 127

[79] J. Cerny, in *Proceedings of the Third International Conference on Nuclei Far From Stability* (CERN Report, Cargese, YEAR), No. 76-13, p. 225. 25

[80] C. H. Dasso and A. Vitturi, Phys. Rev. C **34**, 743 (1986). 26, 115, 116

[81] D. Bowman and et al., Phys. Rev. Lett. **31**, 614 (1973). 27

[82] H. Matsubara and et al., Few-Body System **54**, 1433 (2013). 29

[83] H. Matsubara and et al., CNS Annual Report (2011). 30

[84] M. Takaki and et al., CNS Annual Report (2011). 29

[85] P. Puppe, Phys. Rev. C **84**, 051305 (2011). 31, 119

[86] L. Mandelstam and Ig. Tamm, J. Phys. USSR **9**, 249 (1945). 32, 122

[87] F Cappuzzello and et al., phys. Lett. B (submitted) (unpublished). 32, 113, 117

[88] K. Ikeda, Prog. Theor. Phys. **31**, 434 (1964). 33, 94

[89] D. J. Mercer and et al., Phys. Rev. C **49**, 3104 (1994). 33, 104, 124

[90] Y. Fujta, private communication (unpublished). 34, 77, 104, 122, 124, 125

[91] T. Chittrakarn and et al., Phys. Rev. C **34**, 80 (1986). 34

[92] T.N. Taddeucci and et al., Phys. Rev. C **28**, 2511 (1983). 34

[93] B. K. Park and et al., Phys. Rev. C **45**, 1791 (1992). 34

[94] W. Tomow and et al., Phys. Rev. C **42**, 693 (1990). 35, 100

[95] S. Adachi and et al., Nucl. Phys. A **438**, 1 (1985). 35, 100

[96] D. M. Brink, Phys. Lett. B **40**, 37 (1972). 36

[97] T.N. Taddeucci and et al., Nucl. Phys. A **469**, 125 (1987). 37, 117, 118, 119

[98] M. Cavallaro and et al., Nucl. Instr. Methods A **648**, 46 (2011). 38

[99] D. Pereira and et al., Phys. Lett. B **710**, 426 (2010). 120

[100] F. Cappuzzello and et al., Nucl. Instr. Methods A **763**, 314 (2014). 38, 39

[101] A.Cunsolo et al., Nucl. Instr. Methods A **481**, 48 (2002). 40, 43, 47, 69

[102] F. Cappuzzello, D. Carbone, M. Cavallaro, and A. Cunsolo, in *Magnets: Types, Uses and Safety* (Nova Publisher Inc., New York, 2011), Chap. MAGNEX: an innovative large acceptance spectrometer for nuclear reaction studies, pp. 1–63. 43

[103] A. Cunsolo and et al., Nucl. Instr. Methods A **484**, 56 (2002). 40, 45, 47, 70

[104] M. Cavallaro, Ph.D. Thesis, 2008. 40, 89, 95

[105] D. Carbone, Ph.D. Thesis, 2012. 40, 53, 69

[106] D. Rifuggiato and et al., Proc. of the XVII Int. Conf. on Cyclotron and their Applications, Tokyo, Japan, 2004, p.118. 40

[107] *MOD. 439, Digital Current Integrator*, Ortec, USA. 41

[108] *MOD. V820, 32 Channel Latching Scaler*, CAEN S.p.A, Viareggio, Italy. 41

[109] H.A. Enge, Nucl. Instr. Methods **162**, 161 (1979). 43

[110] D.C. Carey, *The Optics of Charged Particle Beams* (Harwood Academic Publishers, Chur. London. Paris. New York, 1987). 44

[111] M. Cavallaro and et al., Eur. Phys. J. A **48**, 59 (2012). 45, 47

[112] F. Cappuzzello, D. Carbone, and M. Cavallaro, Nucl. Instr. Methods A **638**, 74 (2011). 46, 72, 76, 87

[113] A. Lazzaro and et al., Nucl. Instr. Methods A **570**, 192 (2007). 46

[114] A. Lazzaro and et al., Nucl. Instr. Methods A **585**, 136 (2008). 53

[115] A. Lazzaro and et al., Nucl. Instr. Methods A **591**, 394 (2008).

[116] A. Lazzaro and et al., Nucl. Instr. Methods A **602**, 494 (2009). 46

[117] K. Makino and M. Berz, Nucl. Instr. Methods A **427**, 338 (1999). 46

[118] M. Berz and K. Makino, *COSY INFINTIY Version 8.1*, Department of Physics and Astronomy and NSCL, Michigan State University, East Lansing, USA, 2001. 46

[119] M. Berz, AIP Conf. Proc. **249**, 456 (1991). 46

[120] H.A. Enge, Rev. Sci. Instr. **35**, 278 (1964). 46

[121] B. Schmidt, Nucl. Instr. Methods A **252**, 579 (1986). 50

[122] C. Boiano, R. Bassini, A. Pullia, and A. Pagano, IEEE trans. Nucl. Sci. **51**, 1931 (2004). 50, 51

[123] M. Bordessoule, F. Bartol, M. Lemonnier, and J.C. Santiard, Nucl. Instr. Methods A **390**, 79 (1997). 51

[124] C. Boiano, IEEE trans. Nucl. Sci. **55**, 3563 (2008). 51

[125] *MOD. V550, CAEN Readout for Analogue Multiplexed Signal - Technical Information Manual*, Viareggio, Italy, 2002. 51

[126] D. Carbone, F. Cappuzzello, and M. Cavallaro, Eur. Phys. J. A **48**, 60 (2012). 51, 61

[127] C. Boiano and et al., IEEE trans. Nucl. Sci. (2012). 51

[128] A. Lazzaro, Ph.D. Thesis, 2003. 53, 55, 71

[129] K. Lau and j. Pyrlik, Nucl. Instr. Methods A **354**, 376 (1995). 61

[130] G. Charpak, G. Melchart, G. Petersen, and F. Sauli, Nucl. Instr. Methods **167**, 455 (1979). 61

[131] G.F. Knoll, *Radiation Detection and Measurement* (John Wiley & sons, Inc., 2000). 65

[132] F. Cappuzzello and et al., Nucl. Instr. Methods A **621**, 419 (2010). 66, 67

[133] Lise++: Exotic beam production. 71

[134] W. N. Catford, *Catkin*, 2005. 72

[135] M. Cavallaro and et al., Nucl. Instr. Methods A **637**, 77 (2011). 74, 76, 82

[136] F. Ajzenberg-Selove and et al., Phys. Rev. C **32**, 756 (1985). 77, 86, 109, 116

[137] R.H. Siemssem, C.L. Fink, L.R. Greenwood, and H.J. Koerner, Phys. Rev. Lett. **28**, 626 (1972). 78, 104, 114

[138] J.A. Cameron and B. Singh, Nuclear Data Sheets **109**, 1 (2008). 78, 104, 114

[139] J. Winger, B. M. Sherril, and D. J. Morrissey, Nucl. Instr. Methods B **70**, 380 (1992). 81

[140] *MINUIT, Function Minimization and Error Analysis,*, version 92.1 ed., CERN Program Library Lonf Writeup D506, 1992. 86

[141] F. Cappuzzello and et al., Nucl. Phys. A **739**, 30 (2004). 89, 95, 120

[142] F Cappuzzello and et al., Phys. Lett. B **516**, 21 (2001). 95

[143] S. E. A. Orrigo, Ph.D. thesis, University of Catania, 2004. 89, 95

[144] F.T. Baker and et al., Phys. Rep. **289**, 235 (1997). 89, 90, 93, 101, 102

[145] F. Hofmann and H. Lenske, Phys. Rev. C **57**, 2281 (1998). 89, 90, 95, 96, 97, 99, 106, 108, 122

[146] *Quantum Theory of Many-Particle System* (Mc Graw-Hill, New York, 1971). 93

[147] H. Lenske, J. Phys. G: Nucl. Part. Phys. **24**, 1429 (1998). 95, 96

[148] H. Lenske, F. Hofmann, and C. M. Keil, Jour. Progr. Part. Nucl. Phys. **46**, 187 (2001). 95

[149] K. A. Brueckner, J. R. Buchler, S. Jorna, and R. J. Lombard, Phys. Rev. 1188 (1968). 96

[150] J. W. Negele and D. Wauterin, Phys. Rev. C **5**, 1472 (1972). 97

[151] H. Lenske, private communication (unpublished). 99, 100, 109

[152] M. Cavallaro and et al., Phys. Rev. C **88**, 054601 (2013). 99

[153] F. J. Eckle and et al., Nucl. Phys. A **506**, 159 (1990). 100

[154] C. Yannouleas, M. Dworzecka, and J. J. Griffin, Nucl. Phys. A **397**, 239 (1983). 101

[155] G.F. Bertsch, P. Bortignon, and R. Broglia, Rev. Mod. Phys. **55**, 287 (1983). 101

[156] M. Bhattacharya, C. D. Goodman, and A. Garcia, Phys. Rev. C **80**, 055501 (2009). 104, 124, 125

[157] D. T. Khoa and von Oertzen, Phys. Lett. B **304**, 8 (1993). 106

[158] W. G. Love and M. A. Franey, Phys. Rev. C **24**, 1073 (1981). 108

[159] M. A. Franey and W. G. Love, Phys. Rev. C **31**, 488 (1985). 108

[160] T. Tamura, T. Udagawa, and H Lenske, Phys. Rev. C **26**, 379 (1982). 111

[161] D. R. Bes, O. Dragun, and E. E. Maqueda, Nucl. Phys. A **405**, 313 (1983). 115

[162] W. von Oertzen, Nucl. Phys. A **482**, 357 (1988). 116

[163] G.R. Satchler, *Direct Nuclear reactions* (Oxford Science Publications, ADDRESS, 1983). 117, 120

[164] F. Osterfel, Rev. Mod. Phys. **64**, 491 (1992). 118, 119, 120

[165] W.P. Alford and B.M. Spicer, Advances in Nucl. Phys. **24**, 1 (1998). 118

[166] Y. Fujta, B. Rubio, and W. Gelletly, Progress in Particle and Nuclear Physics **66**, 549 (2011). 118, 119

[167] J.R.B. Oliveira, J. Phys. G: Nucl. Part. Phys. **40**, 105101 (2013). 120

[168] D. Frekers and et al., Nucl. Phys. A **916**, 213 (2013). 121

[169] M. Matsuo, Phys. Rev. C **73**, 044309 (2006). 121, 123

[170] D. E. Albuerger and D. H. Wilkinson, Phys. Lett. B **32**, 190 (1970). 124